RAY W. HERRICK LABORATORIES

A Graduate Research Facility
of The School of Mechanical Engineering

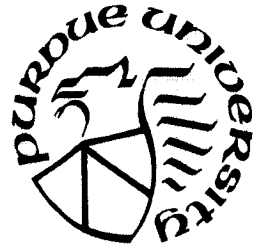

Purdue University

West Lafayette, Indiana 47907

STRUCTURE-BORNE NOISE

Research Contract No. 520 1288-0353

An Investigation of Energy Transmission Due to Flexural Wave Propagation in Lightweight, Built-Up Structures

Sponsored by

NASA

0353-4 HL 86-40

Submitted by:

John Douglas Mickol, Graduate Research Assistant
R.J. Bernhard, Principal Investigator

Approved by:

Raymond Cohen, Director
Ray W. Herrick Laboratories

December 1986

Dedicated to Garbone,

who passed on the difference

between wisdom and knowledge.

ACKNOWLEDGEMENTS

I would like to thank the people of the Structural Acoustics Branch at Langley Research Center for sponsoring this work and providing the opportunity to work at NASA Langley.

I also thank Dr. R.J. Bernhard for initiating this research and serving as my major professor.

I appreciate the assistance provided by Dr. J. Stuart Bolton. Gratitude is given to Dr. James F. Hamilton for serving on my examining committee.

Thanks to my family for their unswerving, unconditional support. High regard to Pete, Mike, Bill, and Michael for their "acoustical stimulation". Appreciation is deserved by Warburg and Bill from whom I learned more than they will EVER know. Tina, what can I say? Thanks to the Eds, Andys, Reiner, Mike, D'Val, Bill, Urs, Bryce, Nancy, Ginny, Connie, Torsten, Judi, Clarence, Art, Lin and Mau Pin for more than diversion but for a "sounding board". Tom, I can no longer follow your path, maybe mine and yours will cross in the future.

TABLE OF CONTENTS

Page

LIST OF TABLES

LIST OF FIGURES

Figure Page

Figure Page

Appendix
Figure Page

LIST OF SYMBOLS

Symbol	Description
$\underline{A}$	boundary value problem unknown vector (see equation 3.5)
B	flexural rigidity
c	speed of sound
C_n	finite element displacement function constants
$\underline{C}$	vector of C_n's
d	length of integration contour
f	frequency in Hz
f_l	lower cut-off frequency for the excitation signal
f_u	upper cut-off frequency for the excitation signal
F	magnitude of input force
$\underline{F}$	forcing function vector
G_{12}	cross spectral function
h	plate thickness
I_m	probe rotational inertia
[I]	identity matrix
Im[ ]	imaginary part
I_{xb}	bending moment intensity in the x-direction
I_{xt}	twisting moment intensity in the x-direction

I_{xm}	total moment intensity in the x-direction
I_{xq}	shear force intensity in the x-direction
k	bending wave number
m	mass per unit length (beam); per unit area (plate), probe mass for sensitivity analysis
M_x	bending moment on the x face
M_{xy}	twisting moment on an xy element
p	parameter in the sensitivity analysis
[P]	local coordinate displacement function evaluation matrix
Q_x	shear force on the x face
r	probe location
Re[ ]	real part
S_{12}	cross spectral function between accelerometer 1 and 2
t	time
[T]	boundary value problem transfer matrix
u_z	displacement transverse to the plate surface
x(t)	excitation time history
$\underline{X}$	trigonometric function matrix (see equation 3.5)
∇^2	2-D Laplacian operator
Δf	frequency interval
Δr	accelerometer spacing
$\delta(\omega)$	actual physical phase difference between accelerometer of the structure-borne wave measurement
ε_B	bias error
ε_P	error in intensity due to instrumentation phase difference

ε_{SOA}	second-order approximation error
μ	Poisson's ratio
Φ_n	Schroeder phase of the nth harmonic of the excitation signal
π_{in}	injected power
ρ	plate or beam density
$\dot{\theta}_x$	rotational velocity in the x direction (about the y axis)
ω	angular frequency

ABSTRACT

Mickol, John Douglas. Purdue University. December 1986. An Investigation of Energy Transmission Due to Flexural Wave Propagation in Lightweight, Built-up Structures. Major Professor: Dr. R.J. Bernhard, School of Mechanical Engineering.

A technique to measure flexural structure-borne noise intensity is investigated. Two accelerometers serve as transducers in this cross-spectral technique. The technique is similar to the two microphone cross-spectral acoustical intensity measurement technique.

The structure-borne sound power is obtained by two different techniques and compared. In the first method, a contour integral of intensity is performed from the values provided by the two-accelerometer intensity technique. In the second method, input power is calculated directly from the output of force and acceleration transducers.

A plate and two beams were the subjects of the sound power comparisons. Excitation for the structures was either band-limited white noise or a deterministic signal similar to a swept sine. The two-accelerometer method was found to be sharply limited by near field and transducer

spacing limitations. In addition, for the lightweight structures investigated, it was found that the probe inertia can have a significant influence on the power input to the structure.

In addition to the experimental investigation of structure-borne sound energy, an extensive study of the point harmonically forced, point-damped beam boundary value problem was performed to gain insight into measurements of this nature. The intensity formulations were also incorporated into the finite element method. Intensity mappings were obtained analytically via finite element modeling of simple structures.

CHAPTER 1 - INTRODUCTION

Sound pressure levels of 95 dB re 20 μPa are not uncommon in propeller driven light aircraft. Levels are expected to become worse as new technology is exploited to produce a fuel efficient but noisy turbo-propeller engine. This level of noise is annoying, fatiguing and may be high enough to cause hearing damage. There is little question that it would be profitable to reduce these sound levels.

McGary [16] has shown that for certain aircraft, there can be equal contribution (at certain frequencies) from air-borne and structure-borne noise in the total noise reaching the aircraft cabin. Air-borne noise, in the context of light aircraft, refers to noise which travels through air for a time and then is transmitted through cabin walls and into the interior section. Structure-borne noise, on the other hand, consists of vibrational energy propagation in solids which is ultimately radiated as noise to the cabin. Sources include such items as engine imbalances, wing flutter, and vortices shed from propellers to the wings.

Fundamental noise control indicates that noise reduction is possible by treating a combination of the source, path, or receiver of the noise. Whereas the receiver, certain sources, and their locations may be easily identified, the paths of structure-borne noise are usually not readily apparent. The intent of this work is to develop a technique to identify structure-borne noise paths. A technique for measuring the structure-borne wave intensity vector, both magnitude and direction, would be of great use since dominant noise paths could then be identified. The noise paths could then be selectively treated, making for efficient distribution of noise control resources; especially important to aircraft because many treatments mean added weight. After the major paths contributing to the noise level in the aircraft cabin are identified, many solutions exist for reducing the flow of energy such as elastomeric isolation, geometric modifications, etc.

As discussed by Williams et. al. [35], the noise path can be defined in terms of direction and magnitude of either structural intensity (mechanical power flow per area) or structural power flow; if the direction of power is conserved throughout the spatial integration of intensity. Intensity seems the preferred choice since power can be derived from intensity but not vice-versa. Since a large part of the structure-borne noise in aircrafts travels through panels or plate-like structures, which

discourage longitudinal and surface wave propagation, it is primarily important to develop a techniques for measuring flexural wave propagation. Simply measuring the dynamic transverse displacement for flexural waves does not suffice since displacement alone does not necessarily correspond to energy flow, just as a plate vibrating in its fundamental mode may undergo large displacements but have no net energy flow.

It is no surprise with the introduction of schemes to determine airborne intensity and acoustical paths that investigations should surface for identifying structure-borne noise paths. The technique utilized here is similar to the well known two microphone technique for measuring acoustic intensity in a fluid. The two accelerometer technique also involves certain quantities of frequency analysis, namely the cross spectrum. Unfortunately, it is also subject to many of the same limitations as the two microphone method. Like the two microphone technique, the two accelerometer technique is sensitive to phase differences in the transducers, reactive field levels, and finite difference approximations, among other limitations. The technique also relies on the knowledge of material properties, such as the flexural rigidity and density of the structure of interest.

In the following chapters appear experiments and theoretical models concerned with validating and developing the intensity measuring technique. The mechanical power derived from two accelerometers is compared to an independent measurement scheme. The power comparisons were performed for three different point-driven structures subject to various excitation signals. Also presented are finite element analysis techniques where power flow in complex, built-up structures can be predicted. The same variables obtained experimentally were obtained from ANSYS finite element code and reduced to structural intensity.

CHAPTER 2 - THEORETICAL DEVELOPMENT

2.1 Introduction

The basis of structural intensity was the work of Noiseux [19] which was later refined by Pavic [21]. Noiseux performed his work nearly two decades ago and was supported through naval institutions. Noiseux not only made important observations in comparing contributions to intensity from internal shear forces and moments acting in a structure, but also considered the transducers required to make a time-domain measurement. Noiseux realized that much useful information could be obtained and a much simpler transducer arrangement would suffice when the farfield assumption is valid. After Noiseux, not much else appears in the literature until Pavic resurrected the investigation of power flow through structures a decade ago. Pavic's development was very similar to Noiseux's though the spatial derivative was accounted for through the use of a finite difference formulation which is implemented by four linear accelerometers.

A long time before the developments of either Pavic or Noiseux and continuing up through the mid seventies, mostly all of the noise control resources related to aircraft has been concerned with the quantification and the development of models to predict air-borne noise. In the late seventies and early eighties however, much discussion in the literature sought to determine the contribution of structure-borne noise to the total interior noise level, especially since the reemergence of propfan engines. Unruh [32], Eversman [4], and McGary [16] are some examples.

Unruh, who concentrated on the contribution to interior noise from the engine, found significant structure-borne components up through the 1600 Hz band [32]. McGary found nearly equal contributions to interior noise from structure-borne and air-borne noise [16]. Recently, Eversman developed models to predict the contribution of structure-borne noise generated by the interaction of the propeller tip vortex system with the wing [4]. Eversman found that depending on the stiffness and mass characteristics of the wing carry-through structure, the contributions of structure-borne and air-borne noise could be comparable.

At this time, the previously underestimated significance of structure-borne noise is drawing attention and resources. Verheij, in 1980, proposed a simplification of

the experimental apparatus for the measurement of structural intensity with the introduction of cross spectral frequency domain measurements in structural intensity [33]. A year later, Redman-White began evaluating some of the frequency domain and finite difference errors much like the investigations of researchers in the area of air-borne sound intensity [24]. Rasmussen demonstrated the use of structural intensity mappings with plates utilizing time domain measurements and the farfield assumption (requiring only two linear accelerometers) [23].

Quinlan [22] sought to define new quantities with regard to the cross spectral method of structural intensity. His measurements not only include "active" intensity but "reactive" intensity (the standing wave energy per unit width) and potential energy density (analogous to the potential energy expression for a torsional spring). The two additional quantities helped to "completely describe both the propagating and stationary energy field" in a structure. All these quantities were formulated in the frequency domain using a four accelerometer intensity "probe" (arranged in the shape of a square).

Using a variation of the initial formulation derived by Noiseux, Williams [35] made structure-borne noise measurements in water through the use of a series of hydrophone measurements and the theory of near field holography.

The near field holography technique extrapolates the pressure field from the hydrophone positioned in the acoustical near field back to the plate. The acoustical near field refers to the space close to the plate directly in line with the location where the intensity is desired and is quite distinct from the near field of the vibrational field within the plate. The structural near field is that area which is excluded by what was referred to above as the "farfield assumption".

As more assumptions are invoked in the development by the above researchers, the more limited became the application and accuracy. The result is that the expression for structural intensity is quite "cultivated" in that many assumptions and manipulations were employed. The development here will be fairly extensive for completeness and to more clearly show the assumptions involved.

2.2 Theory of Structural Intensity

2.2.1 Intensity Formulation from Plate Theory

Figure 2.1 shows an infinitesimal element of a thin structure (i.e. beam or plate). The plate is assumed to conform to Timoshenko plate theory for flexural vibration. Thus, for a homogeneous, uniform plate it is assumed that:

(a) rotational inertia is small.

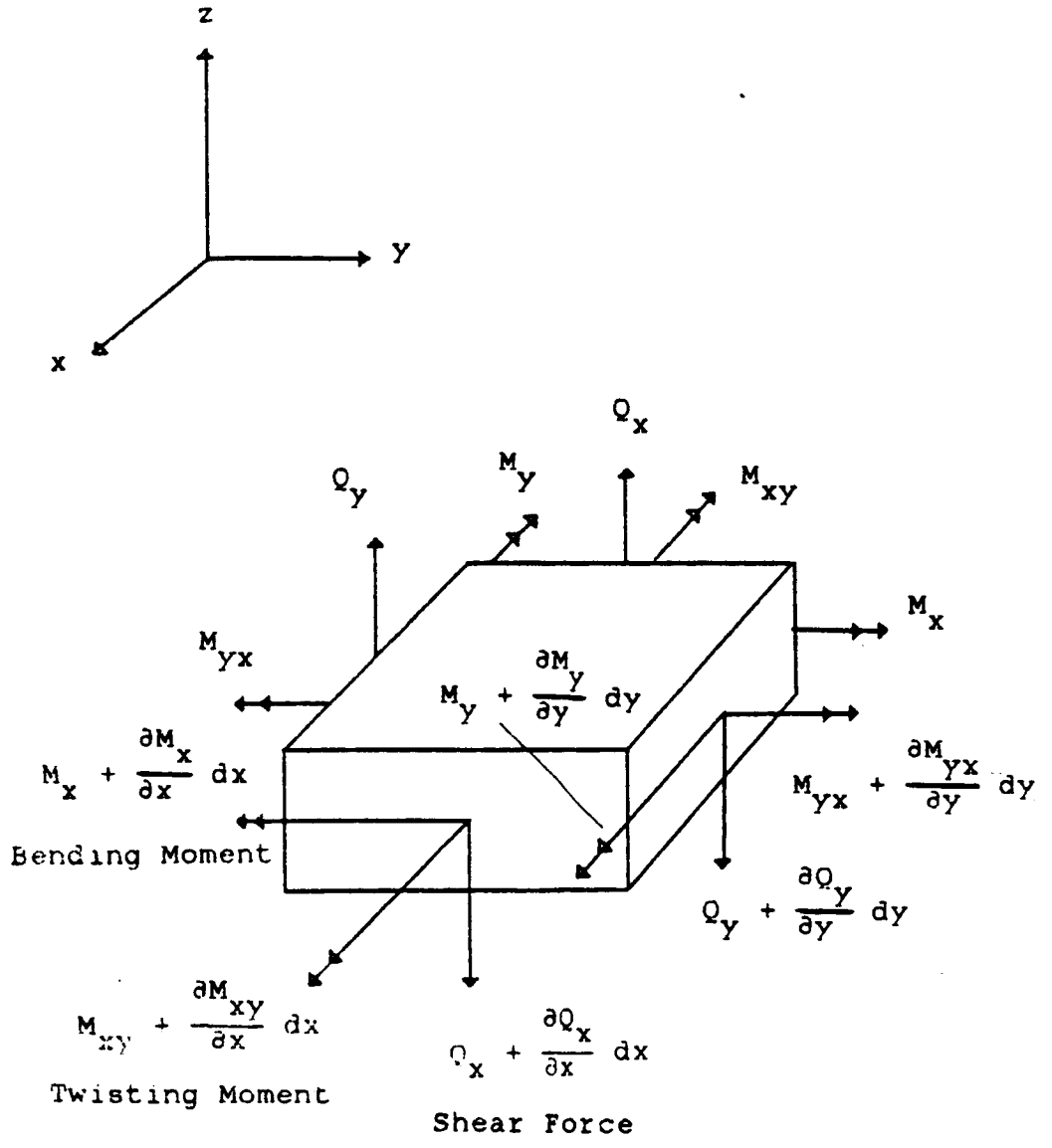

Figure 2.1 Infinitesimal Plate Element in a Vibrational Field

(b) shear deformation can be neglected.

(c) loads are acting normal to the surface.

(d) deflections are small compared to length.

(e) the neutral axis remains unstrained under load.

Structural intensity, which is defined as power flow per unit area, is found by using dot products of force or moment vectors with their corresponding velocity vectors. This dot product actually consists of time averaging the instantaneous values of the vector quantities involved. Later in this development the time averaging will be treated as complex conjugate multiplication for frequency domain measurements of complex variables. Accordingly, the intensity in the x direction can be written as the summation of three components; the shear force contribution:

$$I_{xq} = Q_x \cdot \frac{\partial u_z}{\partial t} \tag{2.1}$$

the bending moment contribution :

$$I_{xb} = M_x \cdot \frac{\partial^2 u_z}{\partial x \partial t} \tag{2.2}$$

and the twisting moment contribution :

$$I_{xt} = M_{xy} \cdot \frac{\partial^2 u_z}{\partial y \partial t} \tag{2.3}$$

where :

Q_x = shear force on the x-face per unit area

M_x = bending moment on the x-face per unit area

M_{xy} = twisting moment on the x-face per unit area

u_z = displacement in the z-direction

Since $\frac{\partial^2 u_z}{\partial y \partial t}$ and $\frac{\partial^2 u_z}{\partial x \partial t}$ actually represent the angular velocity, the total intensity in one direction can then be written:

$$I_x = Q_x \cdot \dot{u}_z + M_x \cdot \dot{\theta}_x + M_{xy} \cdot \dot{\theta}_y \qquad (2.4)$$

where :

$\dot{\theta}_n$ = angular velocity in the n-direction

Also required are the equations resulting from the elemental force balance :

$$M_x = - B \left(\frac{\partial^2 u_z}{\partial x^2} + \mu \frac{\partial^2 u_z}{\partial y^2}\right) \qquad (2.5)$$

$$M_y = - B \left(\frac{\partial^2 u_z}{\partial y^2} + \mu \frac{\partial^2 u_z}{\partial x^2}\right) \qquad (2.6)$$

$$M_{xy} = - M_{yx} = B (1-\mu) \frac{\partial^2 u_z}{\partial x \partial y} \qquad (2.7)$$

$$Q_x = - B \frac{\partial (\nabla^2 u_z)}{\partial x} \qquad (2.8)$$

where :

B = Flexural Rigidity

μ = Poisson's Ratio

2.2.2 Harmonic Excitation and Acoustic Considerations

In considering only one dimensional wave propagation, assuming harmonic variation of source velocity and limiting the measurements to the farfield, flexural behavior is governed by Euler's equation which reduces to:

$$\nabla^2 u_z = \frac{1}{c^2} \frac{\partial^2 u_z}{\partial t^2} = - \frac{\omega^2}{c^2} u_z = - k^2 u_z \qquad (2.9)$$

where :

ω = circular frequency

c = speed of sound in a thin plate

k = wave number

Pavic disregarded the assumptions of equation (2.9) for the more accurate expression whereby flexural displacement is governed by the fourth-order Laplacian not the second-order shown above.

Also for a dispersive medium, the differential equation of motion provides a relationship between wave number and the material properties :

$$k^4 = \frac{\omega^2 m}{B} \qquad (2.10)$$

where :

m = mass per unit area of the plate

2.2.3 Equal Shear Force and Moments Contribution to Intensity

Considering the total contributions from only the moments; summing equations (2.2) and (2.3) :

$$I_{xm} = I_{xt} + I_{xb} = M_x \cdot \dot{\theta}_x + M_{xy} \cdot \dot{\theta}_y \qquad (2.11)$$

Substituting (2.5) and (2.6) into (2.11) results in

$$I_{xm} = -B\left(\frac{\partial^2 u_z}{\partial x^2} + \mu\frac{\partial^2 u_z}{\partial y^2}\right)\cdot\frac{\partial^2 u_z}{\partial x \partial t} + B(1-\mu)\frac{\partial^2 u_z}{\partial x \partial y}\cdot\frac{\partial^2 u_z}{\partial y \partial t} \qquad (2.12)$$

The contribution to intensity from the shear force is:

$$I_{xq} = -B\left(\frac{\partial^2 u_z}{\partial x^2} + \frac{\partial^2 u_z}{\partial y^2}\right)\frac{\partial^2 u_z}{\partial x \partial t} \qquad (2.13)$$

The solution to equation (2.9) may be expressed in travelling wave form as:

$$u_z = Ae^{j(\omega t - k_x - k_y)} + Be^{j(\omega t - k_x + k_y)} + Ce^{j(\omega t + k_x - k_y)} + De^{j(\omega t + k_x + k_y)} \qquad (2.14)$$

If equation (2.14) is substituted into equations (2.12) and (2.13) it can be show that $I_{xm} = I_{xq}$. Thus, the total intensity can be written as twice the intensity contribution due to shear force:

$$I_x = 2\, I_{xq} = 2\left(-B\left(\frac{\partial^2 u_z}{\partial x^2} + \frac{\partial^2 u_z}{\partial y^2}\right)\cdot\frac{\partial^2 u_z}{\partial x \partial t}\right) \qquad (2.15)$$

or

$$I_x = - 2 B \left(\frac{\partial^2 u_z}{\partial x^2} + \frac{\partial^2 u_z}{\partial y^2}\right) \cdot \dot{\theta}_x \qquad (2.16)$$

or

$$I_x = - 2 B (\nabla^2 u_z) \cdot \dot{\theta}_x \qquad (2.17)$$

Substituting equations (2.9) and (2.10) into equation (2.17) and differentiating the transverse displacement and rotational velocity with respect to time

$$I_x = - 2 \frac{\sqrt{B m}}{\omega} (\ddot{u}_z \cdot \dot{\theta}_x) \qquad (2.18)$$

Thus, the structural intensity is expressed in terms of the transverse acceleration, which is measureable with an accelerometer, and the angular acceleration, which can be estimated using two accelerometers.

2.2.4 Finite Difference Approximation

No appropriate angular motion transducers exist. Thus, a finite difference approximation is used to measure the rotational velocity,

$$\dot{\theta}_x = \frac{\dot{u}_{z2} - \dot{u}_{z1}}{\Delta r} \qquad (2.19)$$

and

$$\ddot{u}_z = \frac{\ddot{u}_{z2} + \ddot{u}_{z1}}{2} \qquad (2.20)$$

where :

Δr = spacing between locations of accelerometers on a line in the x-direction

$\ddot{u}_{zn}$ = acceleration at location n

The structural intensity may be written in terms of well-known material properties and relatively easily measured quantities as

$$I_x = -2 \frac{\sqrt{B\,m}}{\omega} \left(\frac{\dot{u}_{z2} - \dot{u}_{z1}}{\Delta r} \right) \cdot \left(\frac{\ddot{u}_{z2} + \ddot{u}_{z1}}{2} \right) \qquad (2.21)$$

2.2.5 Cross Spectral Density Formulation

Equation (2.21) was developed with the implementation of a two accelerometer "probe" in mind and is shown by Verheij [33]. The conversion from time-averaged measurements to frequency domain measurements will now be made. Time-averaged quantities of the form $a_1(t) \cdot a_2(t)$ are found in the frequency domain by $1/2\ \mathrm{Re}[a_1(f)\ a_2(f)]$. When the bracketed quantities are expanded, what remains is a more compact and easily implemented equation, especially when considering frequency domain measurements of complex variables. Equation (2.21) reduces to :

$$I_x = \frac{\sqrt{B\,m}}{\Delta r\ \omega^2} \mathrm{Re}\left[j \left(\ddot{u}_{z2} - \ddot{u}_{z1} \right) \left(\ddot{u}_{z2} + \ddot{u}_{z1} \right)^* \right] \qquad (2.22)$$

or

$$I_x = \frac{\sqrt{B\ m}}{\Delta r\ \omega^2}\ \mathrm{Im}[\ 2(\ddot{u}_{z1}\ \ddot{u}^{*}_{z2})] \qquad (2.23)$$

or

$$I_x = 2\ \frac{\sqrt{B\ m}}{\Delta r\ \omega^2}\ G_{12} \qquad (2.24)$$

where :

G_{12} = the imaginary part of the cross spectrum between accelerometers one and two.

Therefore the flexural wave intensity in one direction depends on the inverse square of the circular frequency, on the well-known properties of the structure, on the signal from two closely spaced accelerometers on the surface and the distance separating these transducers. This derivation assumes the probe is oriented parallel with the coordinate x direction. I_y would be found with the same equation but orienting the probe with the coordinate y direction.

2.3 Summary

Equation (2.24) satisfies important goals for the experimentalist. It addresses the need for parameters which can be easily obtained in the frequency domain. The equation requires only knowledge of common material properties found in most handbooks. In addition, it is readily programmable by common laboratory equipment. However, the limitations of the method are significant. Equal moments

and shear force contributions to the total intensity has been assumed. The structure is also assumed to conform to Timoshenko plate theory. It is assumed that the motion variables, transverse velocity and rotational velocity, can be approximated by finite difference relationships.

CHAPTER 3 - ANALYTICAL MODELS

3.1 Introduction

The structural intensity formulation of chapter 2 resulted in equation (2.22) which expresses intensity in one direction in terms of two closely spaced (with respect to the wavelength) measurements of acceleration in the structure. This expression is uncomplicated at the price of inaccuracies under certain conditions.

The purpose of chapter 3 is to determine the extent the intensity formulation of equation (2.22) suffers from the approximations used. Little work has been done in this area because closed-form solutions for finding the displacement of harmonically forced structures (including damping) is difficult. Only for structures of the simplest geometries are solutions readily derived. Accordingly, the boundary valüe problem of figure 3.1 was chosen as a model to investigate energy propagation in structures.

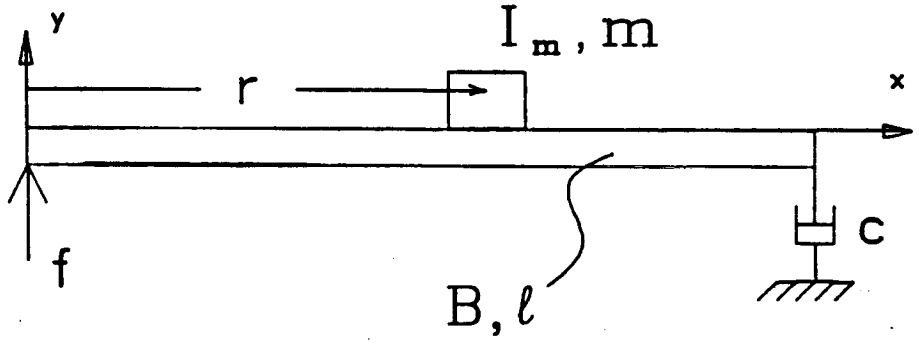

Figure 3.1 Transducer Loaded, Damped Beam Model

3.2 Boundary Value Formulation for a Point-Driven, Point-Damped, Probe-Loaded Beam

The solution to the 4^{th} order governing differential equation of motion for a beam is of the form:

$$y(x) = A \cosh(kx) + B \sinh(kx) + C \cos(kx) + D \sin(kx) \quad (3.1)$$

where y is the transverse displacement. The solution for the case of a probe loaded beam is described by two equations in the form of equation (3.1). The beam is divided into two regions with continuity of transverse displacement and slope enforced at the location of the probe mass. The equations are solved for the complex coefficients, A, B, C, and D, which depend upon the boundary conditions and are a function of f (frequency), E (Young's modulus of elasticity), I (moment of inertia of the beam), r (probe location), m (probe mass), I_m (probe rotational inertia), l (beam length), c (damping coefficient) and F (magnitude of the forcing function).

Because the frequency spectrum of injected power is desired, the coefficients had to be calculated at each frequency increment in the frequency range. The boundary value problem consisted of an 8 x 8 matrix solution (2 regions with 4 boundary conditions each). Two boundary conditions are known at x=0, four compatibility conditions at x=r (the probe location), and two boundary conditions at

x=L. Because of the large number of calculations, the problem was programmed on a VAX 11/780.

3.2.1 Evaluating the Farfield Approximation

As shown in chapter 2, one of the major assumptions made in the derivation of equation (2.22) is that the displacement function satisfies the second order wave equation. This is true provided that the location of the intensity probe is further than about a tenth of the wavelength from a point discontinuity. The region inside a tenth of a wavelength is referred to as the near field.

The "real" or active power flow and "imaginary" or reactive power for the 1" beam (see table 4.2) is given in figures 3.2 and 3.3. The location of the 7.35 g probe is 0.25 m from the forced end of a 2.0 m beam. The damping was quite high for the beam at 50 Ns/m and the force is 1.0 N.

Figure 3.2 and 3.3 represent the exact or moments formulation results. The moments formulation refers to intensity calculated from the complex multiplication of the shear force and moments with their corresponding linear or rotational velocity. The value of real and imaginary power which the transducer or intensity probe would measure (indirectly, power = intensity x area) under the same conditions is shown in figures 3.4 and 3.5. Figures 3.4 and

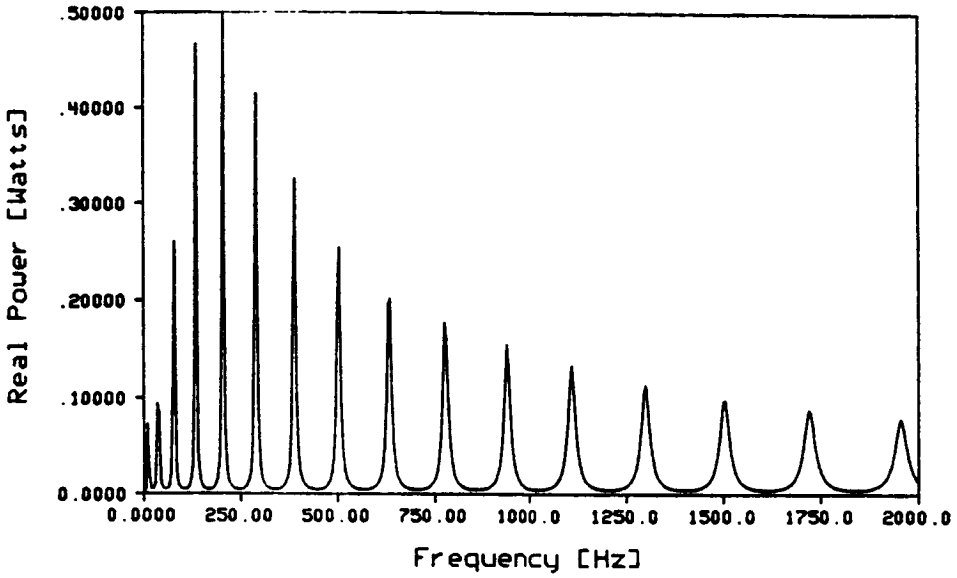

Figure 3.2 Active Exact Power Flow

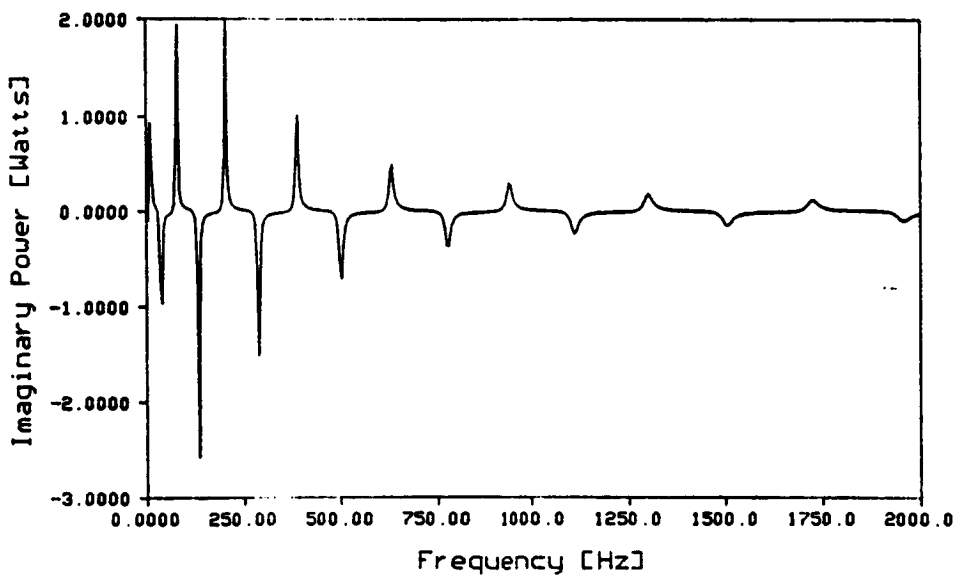

Figure 3.3 Reactive Exact Power Flow

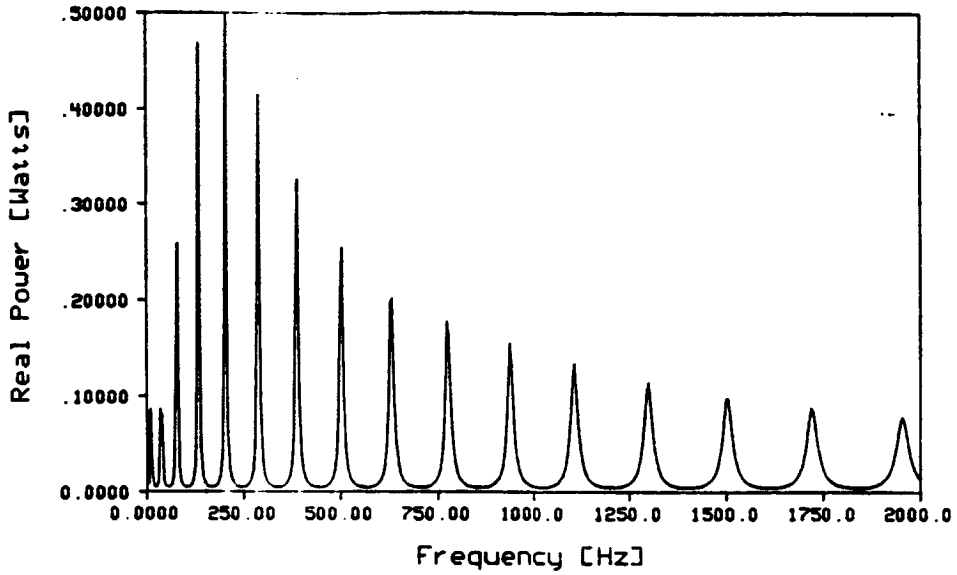

Figure 3.4 Active Power Flow from Transducer Formulation

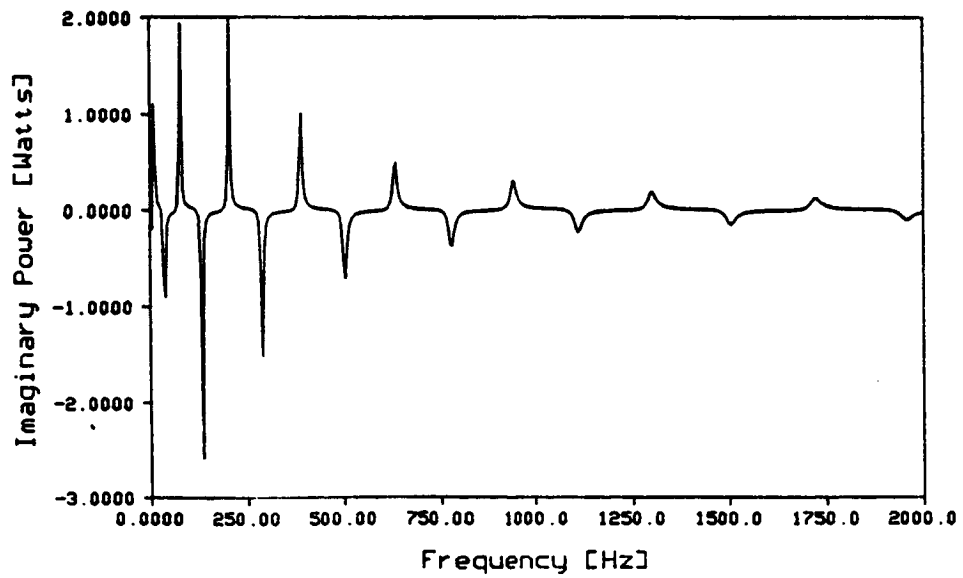

Figure 3.5 Reactive Power Flow from Transducer Formulation

3.5 show the results of the transducer or displacement formulation. The percent difference between the power calculated by the two methods is given by figures 3.6 and 3.7. The difference results from the fact that the transducer formulation tends to overestimate the power delivered by the source at the very near field and then underestimates the power for the remaining near field until it approaches the exact answer in the far field. This plot corresponds to the plot shown by Redman-White [24] which shows the percent error versus kx as opposed to frequency. Redman-White found that experimental results suffered 20% error at a probe position of $\lambda/10$. In this investigation, at $r = \lambda/10$, which occurs at a frequency of 20 Hz, about 20% error results as well. Note that the finite difference approximation is not included because only the near field effects are considered.

An additional parameter was plotted to support figure 3.6 and 3.7. This new parameter, second order approximation error, ε_{SOA}, is the ratio of the displacement function satisfying the second order Euler equation to the displacement function satisfying the fourth order beam equation. The second order approximation error is defined as:

$$\varepsilon_{SOA} = \frac{A\cosh kx + B\sinh kx}{A\cosh kx + B\sinh kx + C\cos kx + D\sin kx} \qquad (3.2)$$

where C and D in the numerator are same as C and D in the denominator. Figures 3.8 and 3.9 essentially show the same

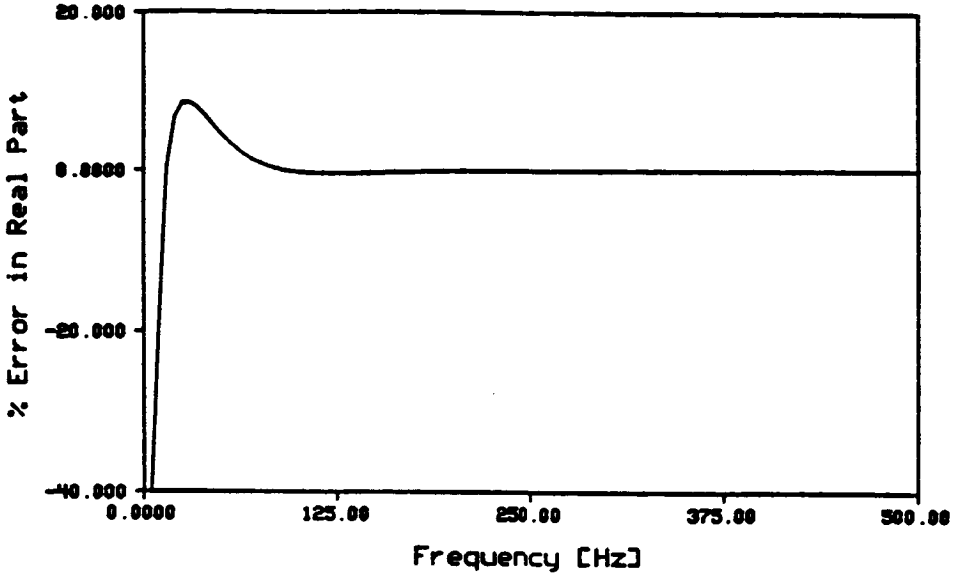

Figure 3.6 Error in the Active Power from the Transducer Formulation

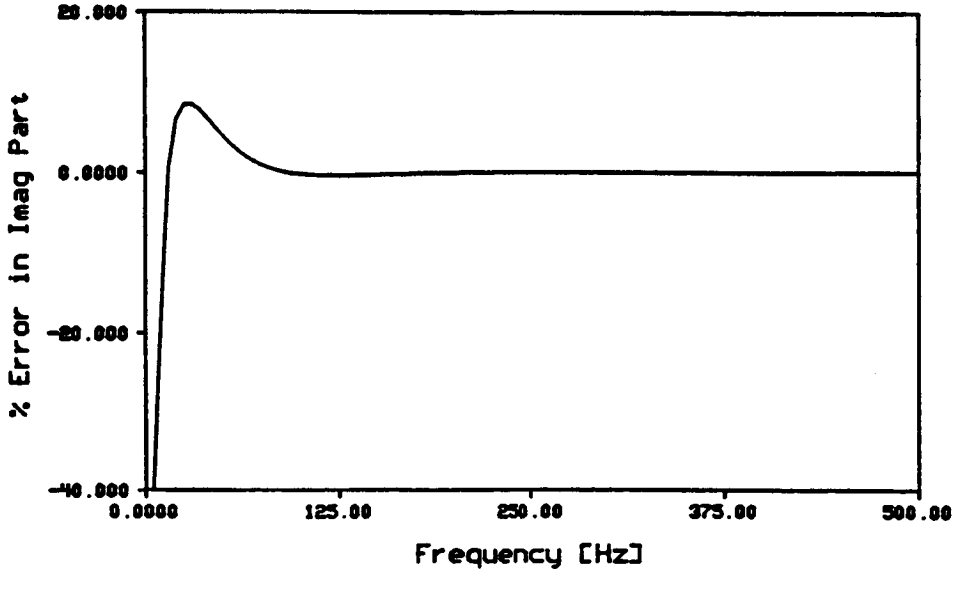

Figure 3.7 Error in the Reactive Power from the Transducer Formulation

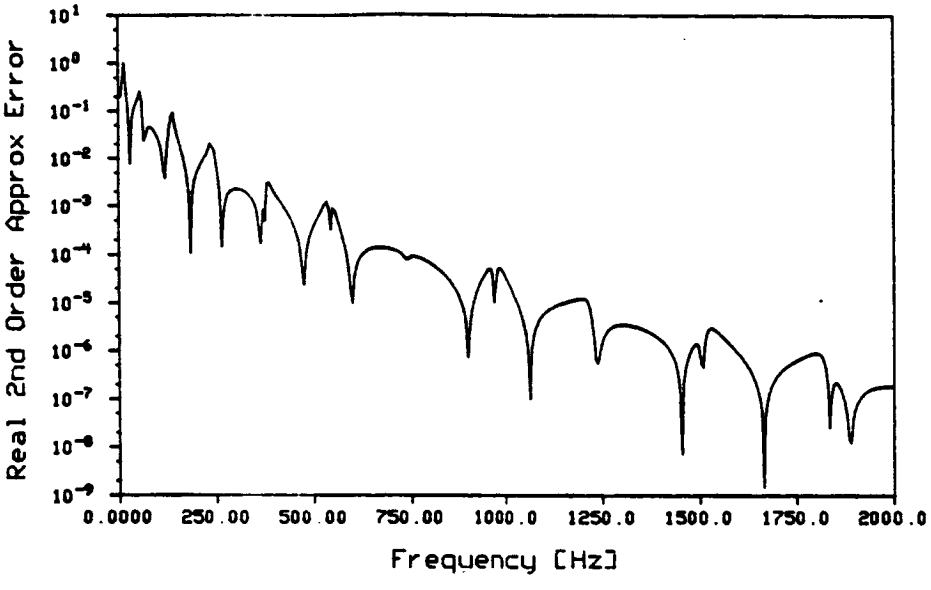

Figure 3.8 Second Order Approximation Error in the Active Power at x=L/2

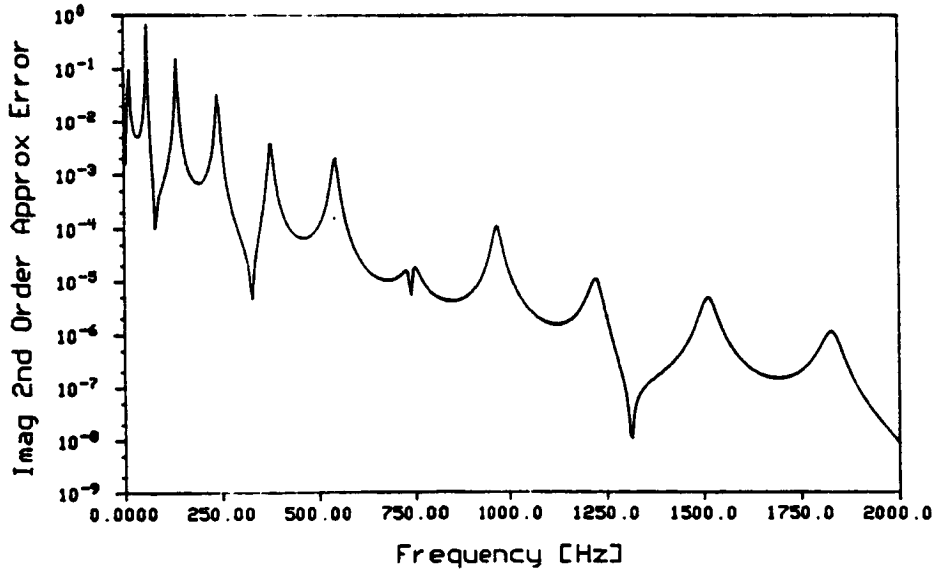

Figure 3.9 Second Order Approximation Error in the Reactive Power at x=L/2

information as shown in figures 3.6 and 3.7 in different form. Figures 3.8 and 3.9 are for the case x = L/2. Figures 3.10 and 3.11 are given for the case x=L/10. The error is generally higher over the frequency range for the x=L/10 case compared to the x=L/2 case. The difference in error is due to the higher influence of the point discontinuity (and the hyperbolic terms of equation (3.2)) closer to the excitation. The error is higher closer (with respect to the wavelength) to the point discontinuity. In addition, figures 3.8 through 3.11 display a "resonant" behavior due to the hyperbolic functions in the displacement expression.

3.2.2 The Sensitivity of Injected Power to Probe Parameters

To determine the effect of probe characteristics on the injected power, the boundary value problem was modified to not only calculate power by the two intensity formulations but also the derivative of power with respect to location, mass and rotational inertia of an intensity probe. The damping factor of the point damper was also used as a variable for the sensitivity studies.

Initially the boundary value problem is posed as:

$$[T] \begin{bmatrix} \underline{A}_1 \\ \underline{A}_2 \end{bmatrix} = \underline{F} \qquad (3.3)$$

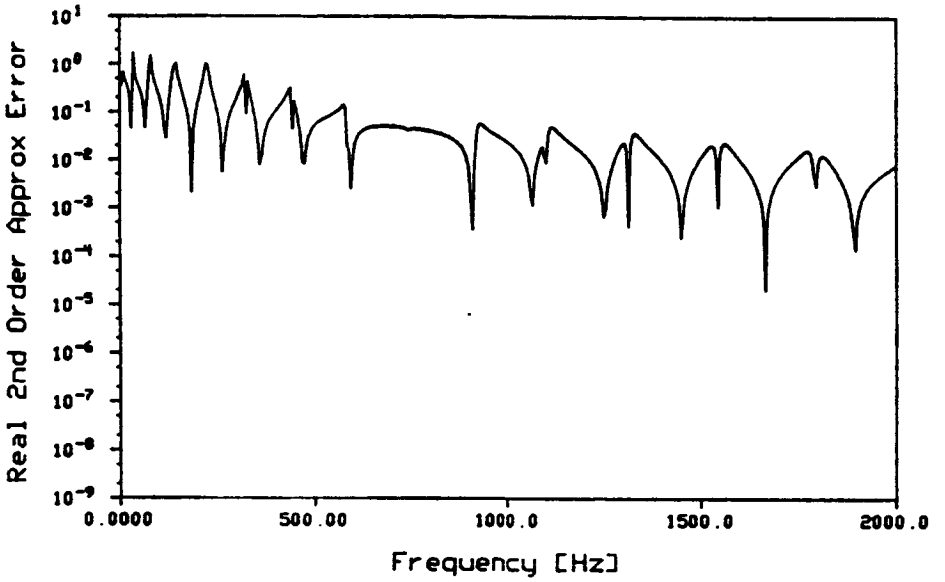

Figure 3.10 Second Order Approximation Error in the Active Power at x=L/10

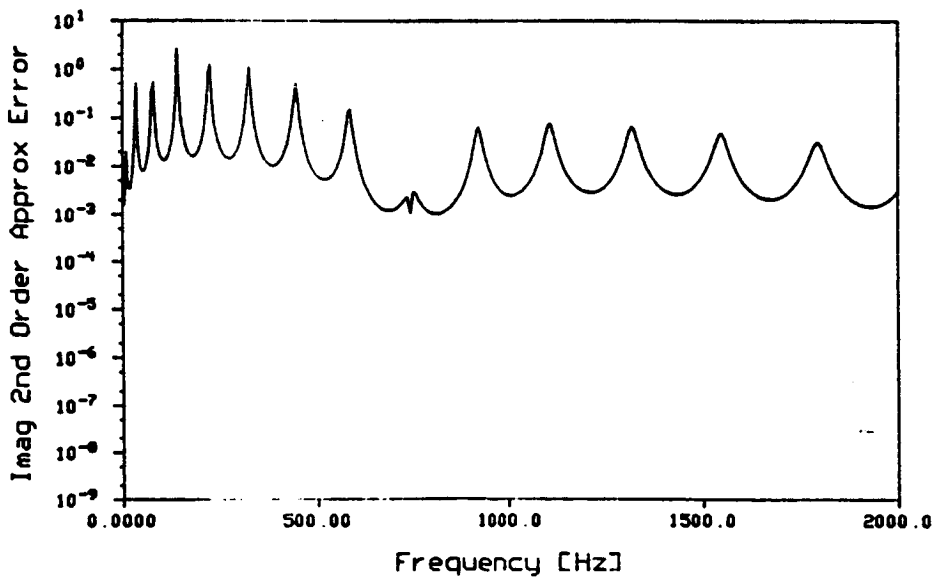

Figure 3.11 Second Order Approximation Error in the Reactive Power at x=L/10

where $\underline{A}_1$ represents a vector composed of A, B, C, D for the length of beam to the left of the mass of figure 3.1 or from x = 0 to r, $\underline{A}_2$ represents the coefficient vector for the remaining length of beam, $\underline{F}$ is the forcing function vector and [T] is a constant coefficient matrix resulting from applying boundary conditions. The transverse displacement of the beam can then be written as

$$y(x) = (\underline{X}^T \mid \underline{X}^T) \begin{bmatrix} \underline{A}_1 \\ \underline{A}_2 \end{bmatrix} \tag{3.4}$$

where $\underline{X} = \begin{bmatrix} \text{coshkx} \\ \text{sinhkx} \\ \text{coskx} \\ \text{sinkx} \end{bmatrix}$

and represents the vector of the trignometric functions (without coefficients) of equation (3.1).

Differentiating equation (3.3) with respect to one of the parameters p results in the equation

$$\begin{bmatrix} \frac{\partial T}{\partial p} \end{bmatrix} \begin{bmatrix} \underline{A}_1 \\ \underline{A}_2 \end{bmatrix} + [T] \begin{bmatrix} \frac{\partial \underline{A}_1}{\partial p} \\ \frac{\partial \underline{A}_2}{\partial p} \end{bmatrix} = \begin{bmatrix} \frac{\partial \underline{F}}{\partial p} \end{bmatrix} \tag{3.5}$$

where p represent any parameter for sensitivity analysis. The vector $\frac{\partial \underline{A}}{\partial p}$ is a vector of the sensitivity of the coefficients of equation (3.1) to the parameter p. In the problem under consideration, $\underline{F}$ is constant and thus $\frac{\partial \underline{F}}{\partial p} = 0$.

The active power is calculated by the expression

$$\pi = \frac{1}{2} \text{Re} \left(F \, V^{*} \right)$$

where V is the transverse velocity at some location on the beam. Thus, the power can be found from

$$\pi = \frac{1}{2} \text{Re} \left(F \, j\omega \, (\underline{X}^{T} \, \underline{A}_1)^{*} \right) \tag{3.6}$$

where * signifies the complex conjugate. The derivative of the $\underline{A}$ vector solved from equation (3.5) is incorporated into the sensitivity expression for power as:

$$\frac{\partial \pi}{\partial p} = \frac{1}{2} \text{Re} \left(F \cdot j\omega \, (\underline{X}^{T} \frac{\partial \underline{A}_1}{\partial p})^{*} \right) \tag{3.7}$$

Equation 3.7 is only true if the forcing function vector, $\underline{F}$, does not depend on the parameter p. Notice $\partial \underline{A}_2 / \partial p$ is not necessary since power is only supplied at x=0.

A series of cases were run for beams of the same dimensions as those tested (see table 4.2). However the damping mechanisms were very dissimilar. The model assumes point-viscous damping. The experimental damping of the beam uses sand distributed over a length of the beam as discussed in chapter 4. The forcing functions are quite different. Experimentally the input force depends on the characteristics of the structure which is much different than the theoretically assumed constant amplitude force. On a normalized basis the analysis can still render useful information for understanding structure-borne noise.

For the 3" beam, the dependency of power to probe mass, rotational inertia, position and damping for three different damping factors was considered initially. The cases were run using the characteristics of the actual probe located at L/4. These sensitivity analyses are shown in figures 3.12 to 3.14. The input power is more sensitive to the parameters at higher damping. The damped natural frequency shifts more with higher damping and thus near the resonances there are significant changes, both positive and negative, in input power.

The sensitivity of the input power to the mass and rotational inertia of the probe is similar. Increasing both parameters lowers the frequency at which the resonances occur. The input power at the original resonances will decrease and the input power at the new resonance will increase. Note that power is increased or decreased with a change in mass or rotational inertia of the probe. Thus introducing a probe onto the beam will have an effect particularly at the resonances. Furthermore, it is not apparent when taking a measurement whether the experimental data is an overestimation or underestimation of the actual power flow because of the effect of the probe.

The sensitivity of power to r/wavelength is negligible. The parameter r/wavelength establishes the distance of the probe from the source relative to a wavelength.

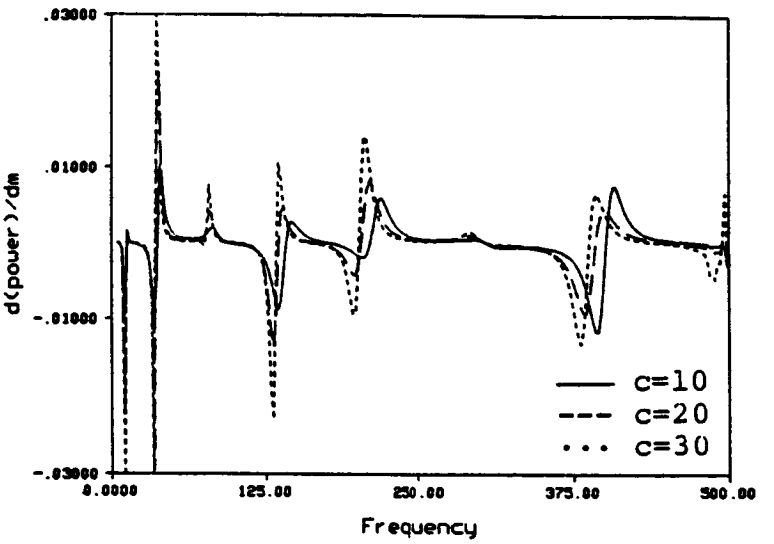

Figure 3.12 The Sensitivity of Injected Power to Probe Mass for Various Damping Factors

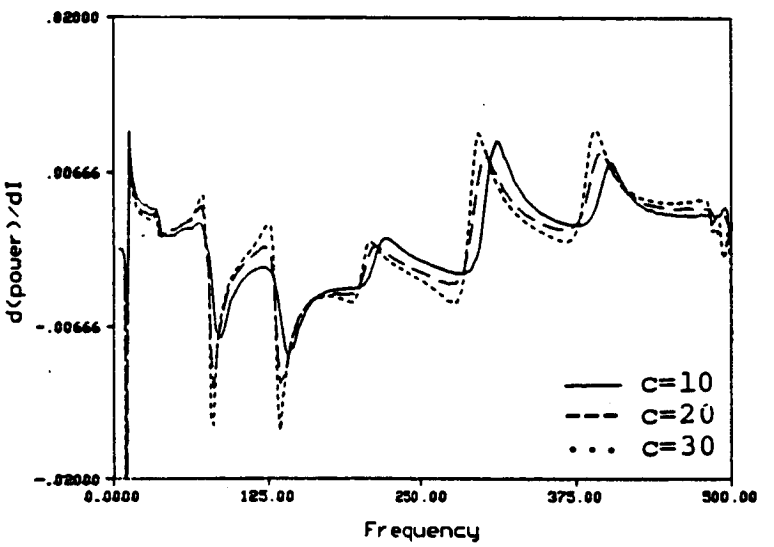

Figure 3.13 The Sensitivity of Injected Power to Probe Rotational Inertia for Various Damping Factors

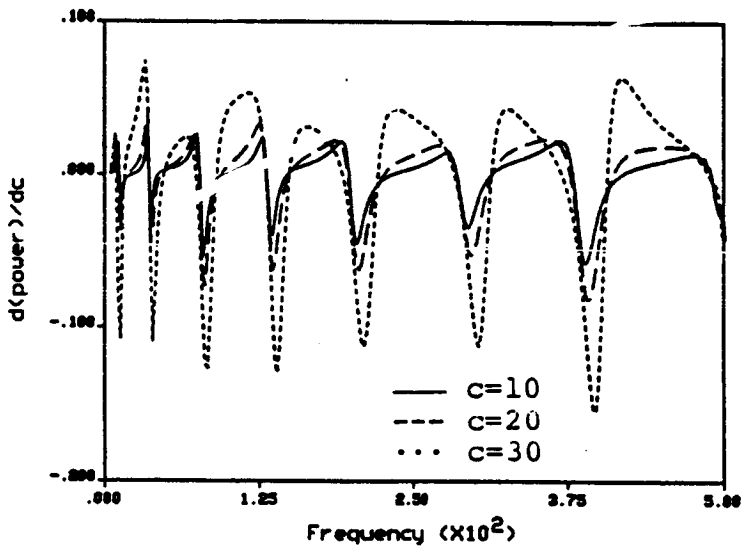

Figure 3.14 The Sensitivity of Injected Power to Point Damping for Various Damping Factors

Thus the probe is always the same relative distance from a node or antinode even though it moves down the length of the beam. The fact that this parameter r/wavelength has no effect is reasonable. However figures 3.6 and 4.36 show that when the probe is moved to different positions relative to nodes, position has a large effect. In practice, for broadband excitation and a dispersive medium, the probe will be positioned at nodes, antinodes, and positions in between simultaneously for each excitation frequency. Thus probe location is an important parameter to consider when making an intensity measurement.

The damping factor itself has a large effect on power as shown in figure 3.14. The injected power is either increased or decreased significantly at all frequencies although the beam is less sensitive to damping when damping is low.

Additional cases of the sensitivity of the input power to the same three parameters (m,I,c) studied above were considered. The cases compare $\frac{\partial \pi}{\partial p}$ (where p is the parameter) with no probe (zero mass and rotational inertia) to $\frac{\partial \pi}{\partial p}$ with values of mass and rotational inertia the same as the actual probe. The probe for the analysis was placed at a location of r=L/4. This analysis was performed for both the 3" beam with a low moment of inertia, figures 3.15 to 3.17, and the 1" beam with a higher moment of inertia,

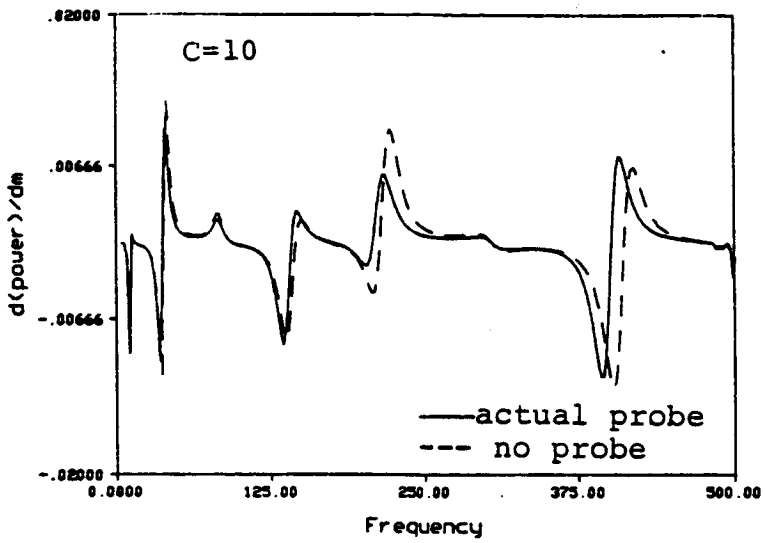

Figure 3.15 The Sensitivity of Injected Power to Probe Mass for a Probe Versus No Probe for a Light Beam

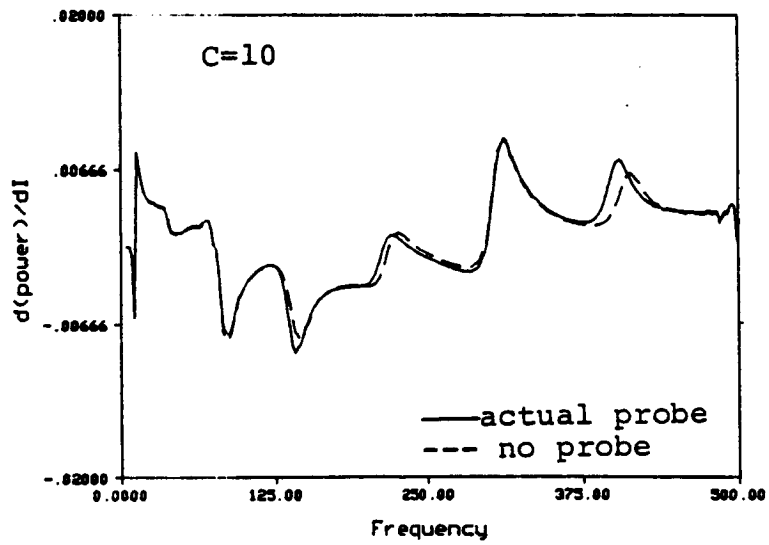

Figure 3.16 The Sensitivity of Injected Power to Probe Rotational Inertia for a Probe Versus No Probe for a Light Beam

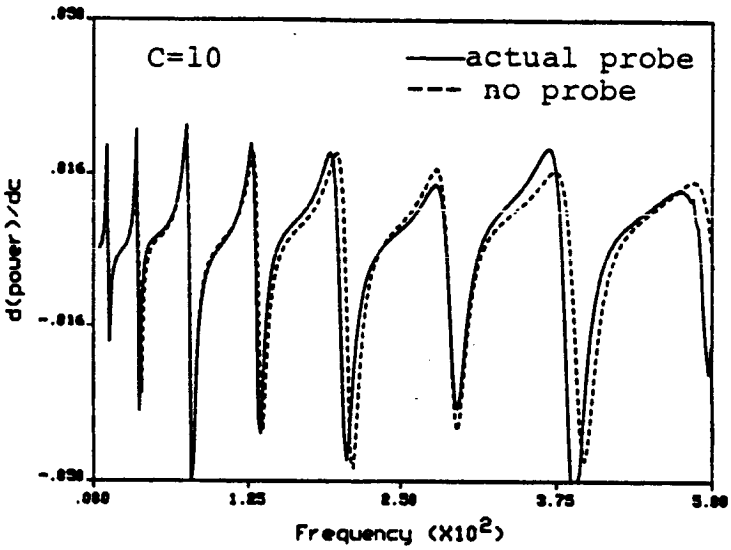

Figure 3.17 The Sensitivity of Injected Power to Point Damping for a Probe Versus No Probe for a Light Beam

figures 3.18 to 3.20. For a linear system the comparisons in each figure would be identical. The results are similar to a great degree. Thus, while it was shown in figures 3.12 and 3.13 that the input power is sensitive to probe inertia, figures 3.15, 3.16, 3.18, 3.19 show that power is essentially a linear function of inertia. Therefore the sensitivity of power input to any given probe mass is significant and relatively the same. The probe also has less overall effect on a beam with a higher beam moment of inertia, but will have a more significant effect at the natural frequencies.

3.3 Finite Element Analysis

In addition to an exact but limited boundary value analysis of the beam, an approximate analysis technique, the finite element method was used. Finite element analysis is used for two purposes:

1. while the boundary value analysis is capable of verifying the cross-spectral structural intensity method, a two-dimensional finite element problem can check the path mapping characteristics of the method as well.

2. the finite element method can be used in the future to model more elaborate, built-up structures.

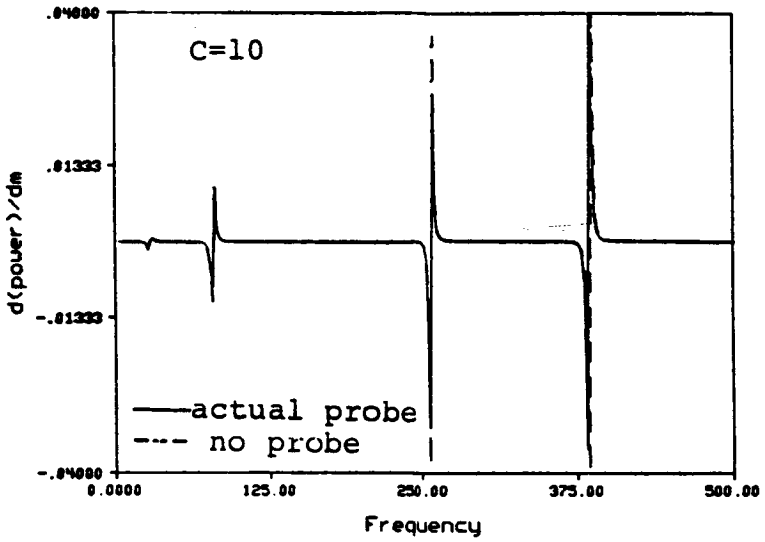

Figure 3.18 The Sensitivity of Injected Power to Probe Mass for a Probe Versus No Probe for a Heavy Beam

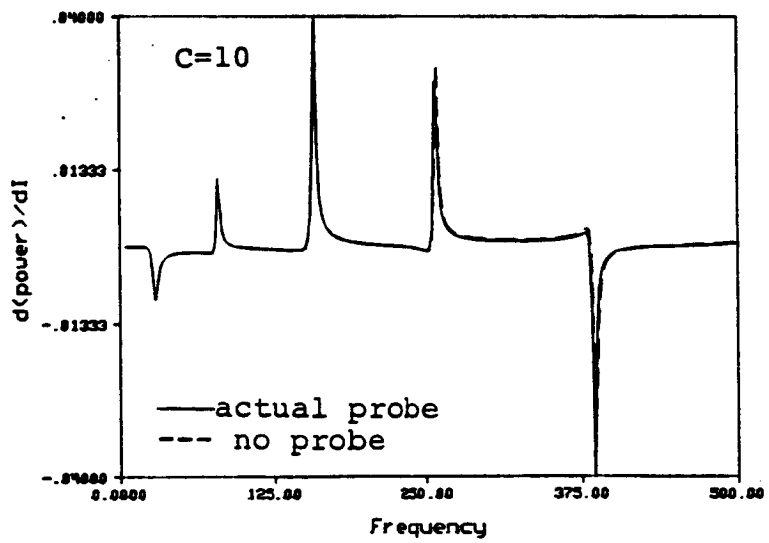

Figure 3.19 The Sensitivity of Injected Power to Probe Rotational Inertia for a Probe Versus No Probe for a Heavy Beam

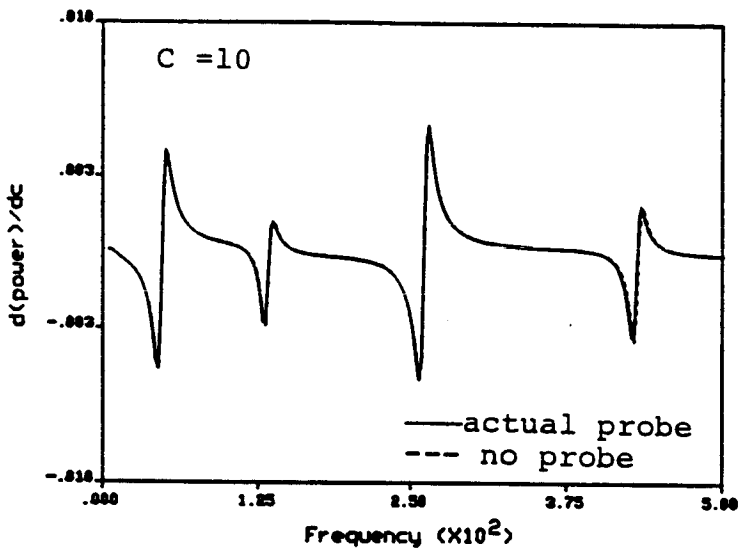

Figure 3.20 The Sensitivity of Injected Power to Point Damping for a Probe Versus No Probe for a Heavy Beam

An investigation of structural intensity demands certain capabilities of a finite element package. First, the finite element software must allow harmonic point-forced models. Secondly, the code must provide a viscous (preferably point) damping element to model energy absorption. The last requirement is that the package should possess a 2-dimensional shell element having bending capabilities and at least 3 degrees of freedom (DOF) per node: displacement perpendicular to the plate surface and rotation (or slope) about both axes lying in the plane of the element.

An available code which possesses all three characteristics is ANSYS. The harmonic response, defined as KAN = 6 in ANSYS was used. The elements utilized were the rectangular shell element number 43, the two dimensional elastic beam element number 3, and the spring-damper element number 14.

Because the available code was for educational uses, the program had a problem size limitation. The largest problem which could be solved was a 10 x 15 element rectangular plate.

One goal of the finite element analysis is to compare the 2-dimensional intensity mappings resulting from the transducer or displacement formulation and the mappings furnished by the "less cultivated" moments formulation which utilizes equation (2.4). The displacement formulation

utilizes the direct output of the finite element program. The moments formulation requires that the values of shear force, bending moment, and twisting moment as well as the translational and rotational motion be known for each node.

3.3.1 Displacement Interpolation

The bending moment, twisting moment and shear force at the centroid of the element can be obtained from the ANSYS output of the rectangular shell element. Unfortunately, the transverse displacement and slopes are given at the nodes of the elements. Therefore, to compute intensity the 3 motion DOF's were interpolated to determine their value at the elemental centroid.

The displacement function for the rectangular shell which appears in the ANSYS user's manual is:

$$\phi_z(x,y) = C_1 + C_2x + C_3y + C_4x^2 + C_5xy + C_6y^2 + C_7x^3 + C_8x^2y + C_9xy^2 + C_{10}y^3 + C_{11}x^3y + C_{12}xy^3 \quad (3.8)$$

The rotational motions are spatial x and y derivatives of the displacement function of equation 3.8. For this rectangular shell there are 12 shape functions of the form of equation 3.8; one transverse displacement, $\phi(x,y)$, and two slope or rotation functions, $\phi^x(x,y)$ and $\phi^y(x,y)$, at each node. Interpolation requires knowledge of the values of the C_j. The C_j are found from a 12 x 12 (3 displacement

functions x 4 nodes) matrix problem of the form:

$$[P]\ \underline{C} = [I] \tag{3.9}$$

where [P] is a constant coefficient matrix and [I] is the identity matrix. Once the C's are known the interpolated displacement function is

$$u_z(x,y) = \sum_{j=1}^{4} u_{zj}\phi_j + \sum_{j=1}^{4} \left(\frac{\partial u_z}{\partial x}\right)_j \phi_j{}^x + \sum_{j=1}^{4} \left(\frac{\partial u_z}{\partial y}\right)_j \phi_j{}^y \tag{3.10}$$

where:

u_{zj} = the transverse displacement at the j^{th} node

$\left(\frac{\partial u_z}{\partial x}\right)_j$ = the rotation about the x axis at the j^{th} node

$\left(\frac{\partial u_z}{\partial y}\right)_j$ = the rotation about the y axis at the j^{th} node

At the centroid x = 0 and y = 0, only the first constant in each shape function is required, thus equation 3.10 becomes

$$u_z(0,0) = \sum_{j=1}^{4} u_{zj} C_{j1} + \sum_{j=1}^{4} \left(\frac{\partial u_z}{\partial x}\right)_j C_{j1}{}^x + \sum_{j=1}^{4} \left(\frac{\partial u_z}{\partial y}\right)_j C_{j1}{}^y \tag{3.11}$$

The expressions for the remaining degrees of freedom are found in a similar fashion. The j index corresponds to one of four nodes of the element, so that not only is the displacement at the centroid influenced by the displacement at the four nodes but also by the slopes (in both directions) at the nodes. To verify the solution, various allowable (by the shape function of order less than a complete cubic in x and y) configurations were evaluated

successfully. Appendix A illustrates, in a three-dimensional representation, the interpolation of the displacement and slopes in the model plate for a problem solution. The source listing which contains the interpolation algorithm is included in appendix B.

3.3.2 Point-Driven, Point-Damped, Probe-Loaded Beam

The finite element analysis was compared to the boundary value analysis for a beam. The model beam was composed of forty elastic beam elements and one general mass element. The model was forced at one end and damped at the other by a one dimensional spring-damper element. The end of the spring-damper was fixed to ground by restricting displacement in three coordinate directions.

ANSYS only provides the real motion degrees of freedom, real moments, and real shear force values even though ANSYS is capable of complex analysis. The active injected power calculation, however, requires both imaginary and real values. Therefore the program must be run twice for each case: first with purely real excitation (supplying real results) and a second time with a purely imaginary forcing function (supplying imaginary results). The program which reduces the ANSYS output is included in appendix B.

Good results were obtained for the displacements, slopes, and injected power for the finite element analysis versus the boundary value analysis. The values were always within 1% of each other and frequently as close as numerical errors allowed.

The agreement established the credibility of the finite element techniques. The favorable comparison between the boundary value problem and FEA also showed ANSYS capable of forced harmonic response analysis and the precise analysis required for structural power flow calculations.

3.3.3 Point-Driven, Point-Damped Plate

The finite element model of figure 3.21 was used to compare the two intensity formulations and determine if the structural intensity method is able to indicate location of sources and receivers and the paths between them for structure-borne noise. The 11 x 16 nodal grid comprising 150 elements is forced at "F" and damped at "D". The 1.575 mm thick plate is 1.0 m x 1.5 m.

Each rectangular shell element has 24 degrees of freedom, the displacements and slopes in the three coordinate directions at the four corner nodes. Since the plate lies in the x-y plane and is forced and damped transversely (z direction) only the displacement in the z and slopes (rotations) about the x and y need to be considered. The

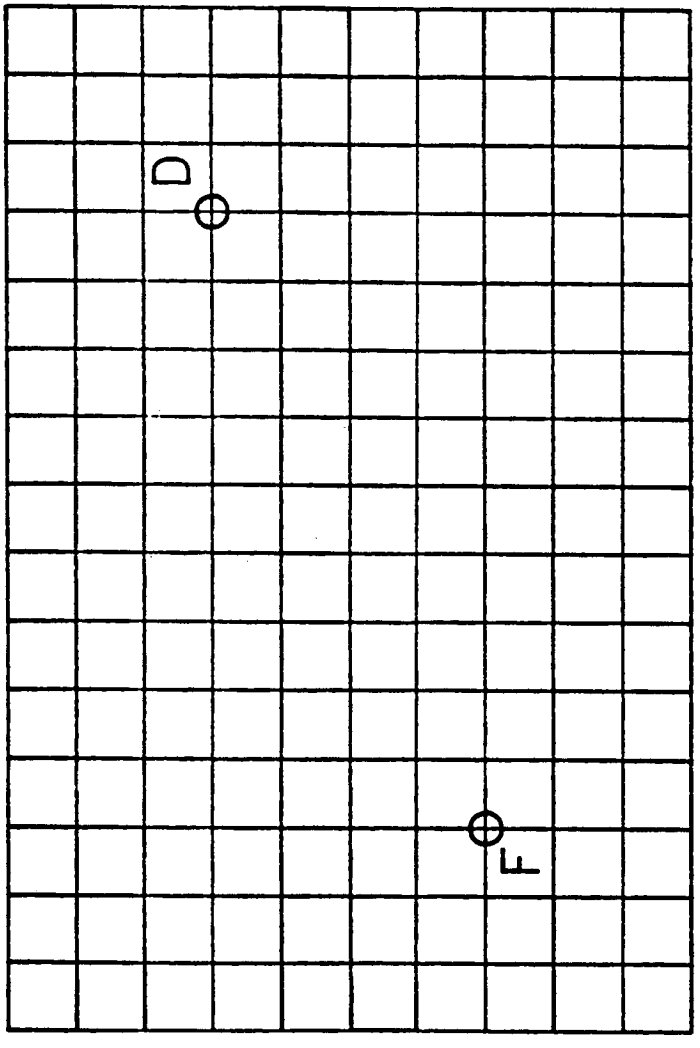

Figure 3.21 Finite Element Model

end of the point damper element is constrained against displacement in the three coordinate directions. The damper end node is the only node constrained in the analysis.

In each case, the magnitude of the forcing function was 1 N and the point damping coefficient was 100 Ns/m. The frequency of analysis was 100 Hz.

Appendix A shows the transverse displacement, rotations in both directions, bending moments, twisting moments and shear force solutions. The displacement results are the only results which are physically represented by the plots. The magnitude of the other results are illustrated in three-dimensional plots to indicate points of extreme conditions and to serve as a check on discretization.

The structural intensity mapping using the displacement formulation is shown in figure 3.22. The figure illustrates the usefulness of the structural intensity method. The tail of each vector is located at a node in the finite element model. It appears clear where the source is located. Because of the meandering path of the vectors of large magnitude, the location of the damper could only be estimated to within 1 element size. A finer discretization may alleviate this uncertainty.

Figure 3.23 shows the intensity mapping using the displacement formulation and the interpolated values of the

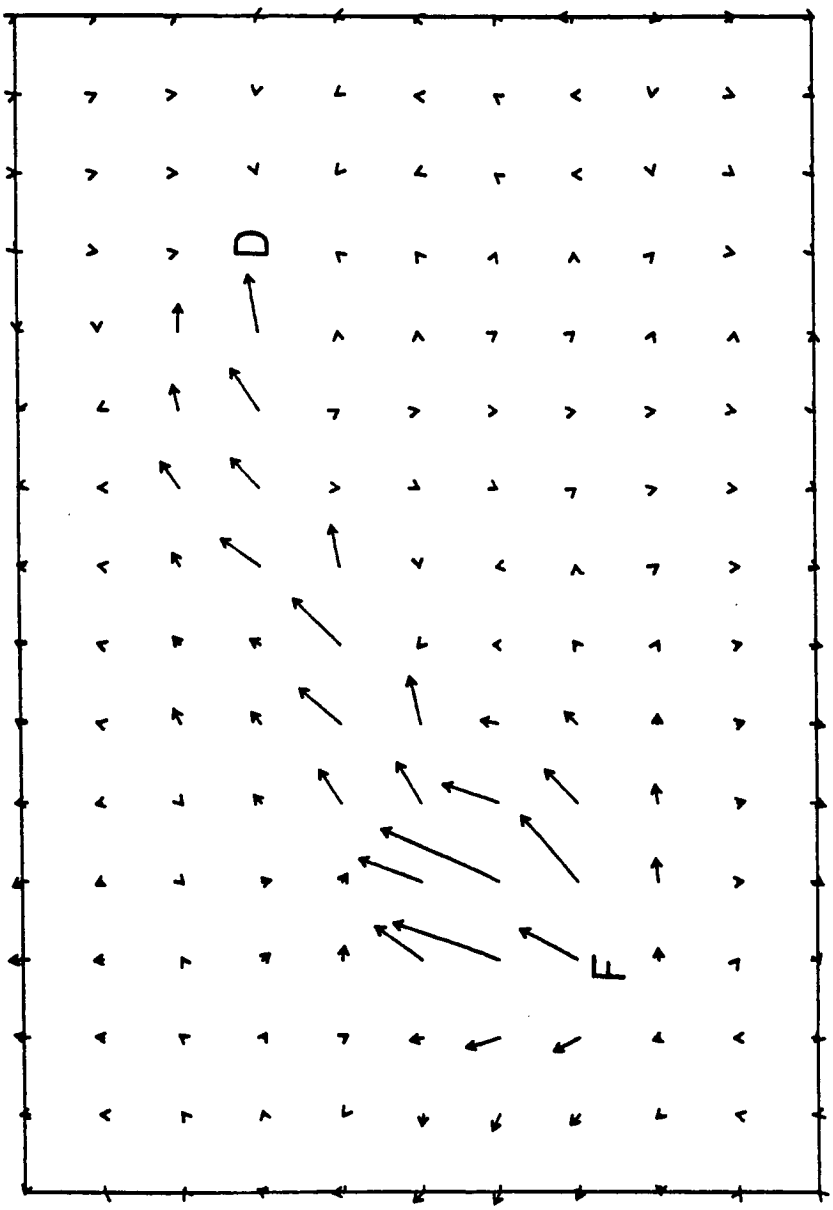

Figure 3.22 Finite Element Intensity Mapping Using the Transducer Formulation

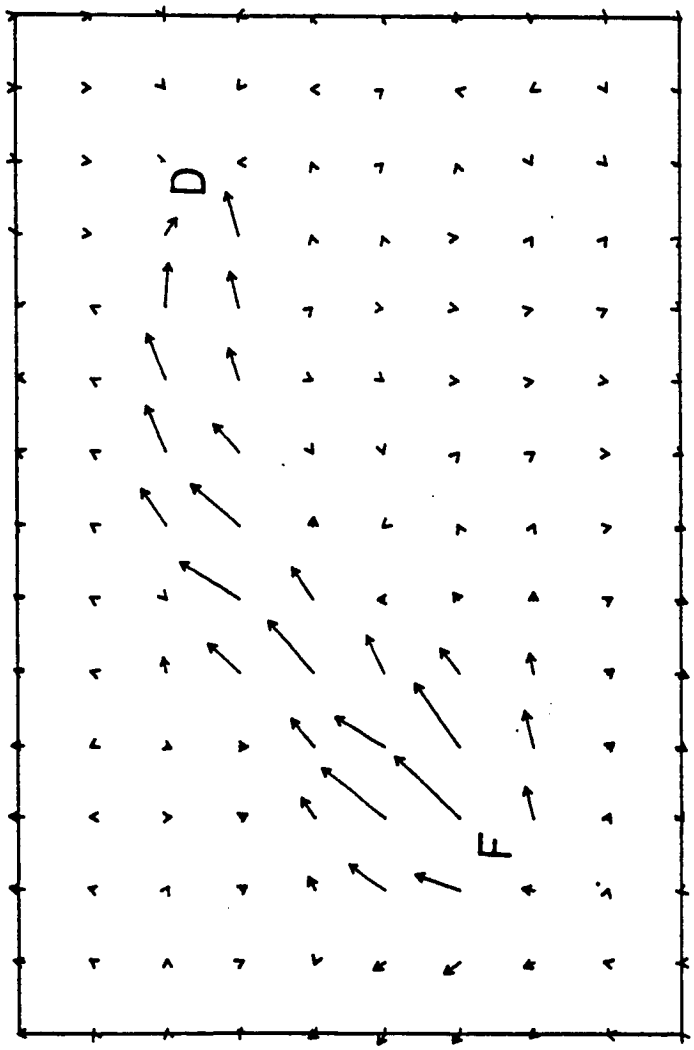

Figure 3.23 Interpolated Finite Element Intensity Mapping Using the Transducer Formulation

displacement and slopes. The vector tails are positioned at the centroids of the original finite elements. The mapping displays all the characteristics of the original uninterpolated mapping such as a torturous path and an easily identified source location. A significant difference exists between figures 3.22 and 3.23 because the interpolated values are further from discontinuities, thus the approximations should be better.

Figure 3.24 shows the intensity mapping using the moments formulation. The vectors in the figure originate at the centroidal location for each finite element. While the location of the source is easy to locate, the location of the damper would probably be misjudged by about one half of a length of an element side. Because the formulation represents a more exact form (except for the finite element approximation), the moments formulation provides a more accurate picture of power flow through the plate. A comparison of figure 3.23 and 3.24 show the inaccuracies of the displacement formulation.

The moments formulation mapping for intensity resulted in larger intensity values near the source. However, further than an element size from the source, the three intensity calculations result in similar intensity vectors. The moments formulation is expected to be more accurate in the nearfield which in the case of the plate is the region

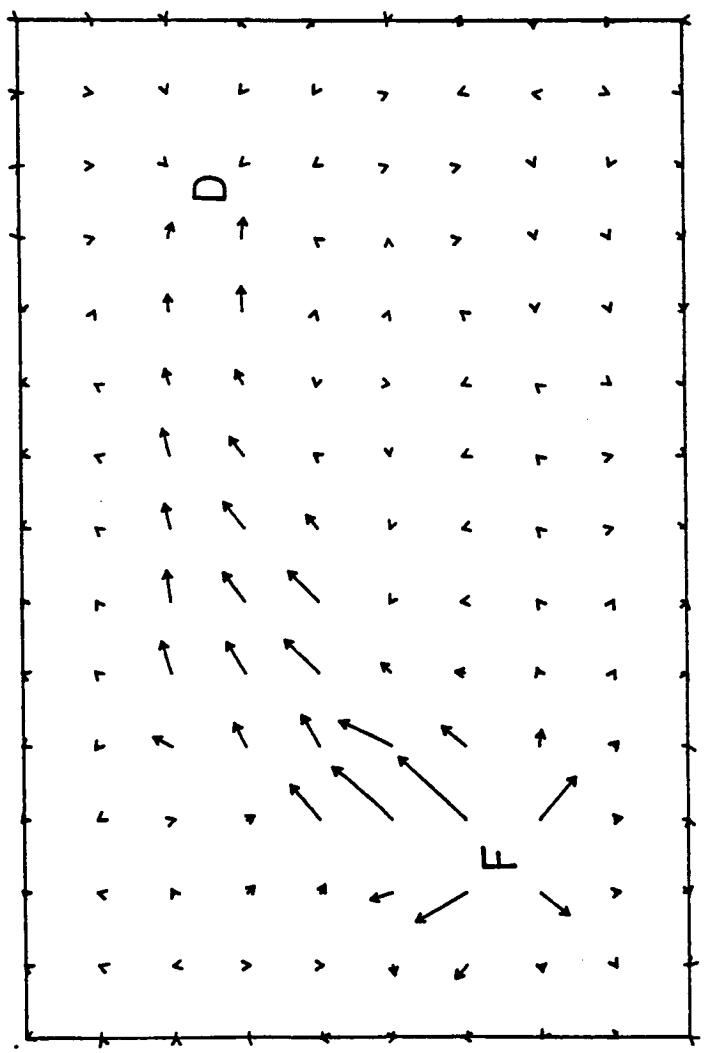

Figure 3.24 Finite Element Intensity Mapping Using the Moments Formulation

around the point force, the point damper and the plate edges.

The intensity mappings of figures 3.22, 3.23, and 3.24 provide clear evidence of what is theoretically possible with structural intensity methods and finite element method. Because of severe size limitations on the version of the finite element code, more elaborate models were not possible. However, the moment formulation is shown to be valid and provided the finite element models are valid, the method can be usefully applied to monitor energy transmission through built-up structures.

CHAPTER 4 - STRUCTURAL INTENSITY MEASUREMENTS

4.1 Introduction

With much of the theoretical development and modeling of the previous chapters complete, attention is now given to some considerations for the application of structural intensity. The study investigates structures similar to the model beams and plate of the preceding chapters. Two types of experiments were performed. The first type compares power injected into a test structure using the structural intensity technique and an impedance-type measurement. Secondly, intensity measurements were taken over an array of points for a plate to form a mapping. Additional experiments helped demonstrate the experimental errors of the discussion.

4.2 Experimental Apparatus

In this section is presented the description of the instrumentation used. The description includes the considerations necessary for experiments of this nature and also a discussion of the limitations.

4.2.1 Instrumentation

Figure 4.1 is a diagram of the experimental set-up. The components which comprise the system are further described in Table 4.1. The microcomputer serves two functions. Initially it provides a Schroeder-phased digital input signal to the Wavetek waveform generator. Secondly, the microcomputer serves as a data collection device. Once the waveform generator is loaded, it both supplies the shaker with a signal via a GenRad amplifier and also serves as the clock for the Nicolet Fast Fourier Analyzer to facilitate synchronous data sampling.

The exciter is a Bruel & Kjaer 10N max force electromechanical shaker. The first natural frequency of the shaker, 18 kHz, is well outside the frequency range of interest. To determine the transfer characteristics of the shaker, the signal described in section 4.3 was input to the shaker and a B&K charge-mode accelerometer was attached to the shaker table with cyanoacrylate glue to ensure a stiff or rigid bond. The resulting transfer function, output acceleration voltage over input signal voltage, of figure 4.2, shows flat response. The input signal for this test was between 70 Hz and 1850 Hz.

The shaker is connected to the structure using a piece of tempered wire soldered to two studs. A simple calculation shows the natural frequency for longitudinal vibration

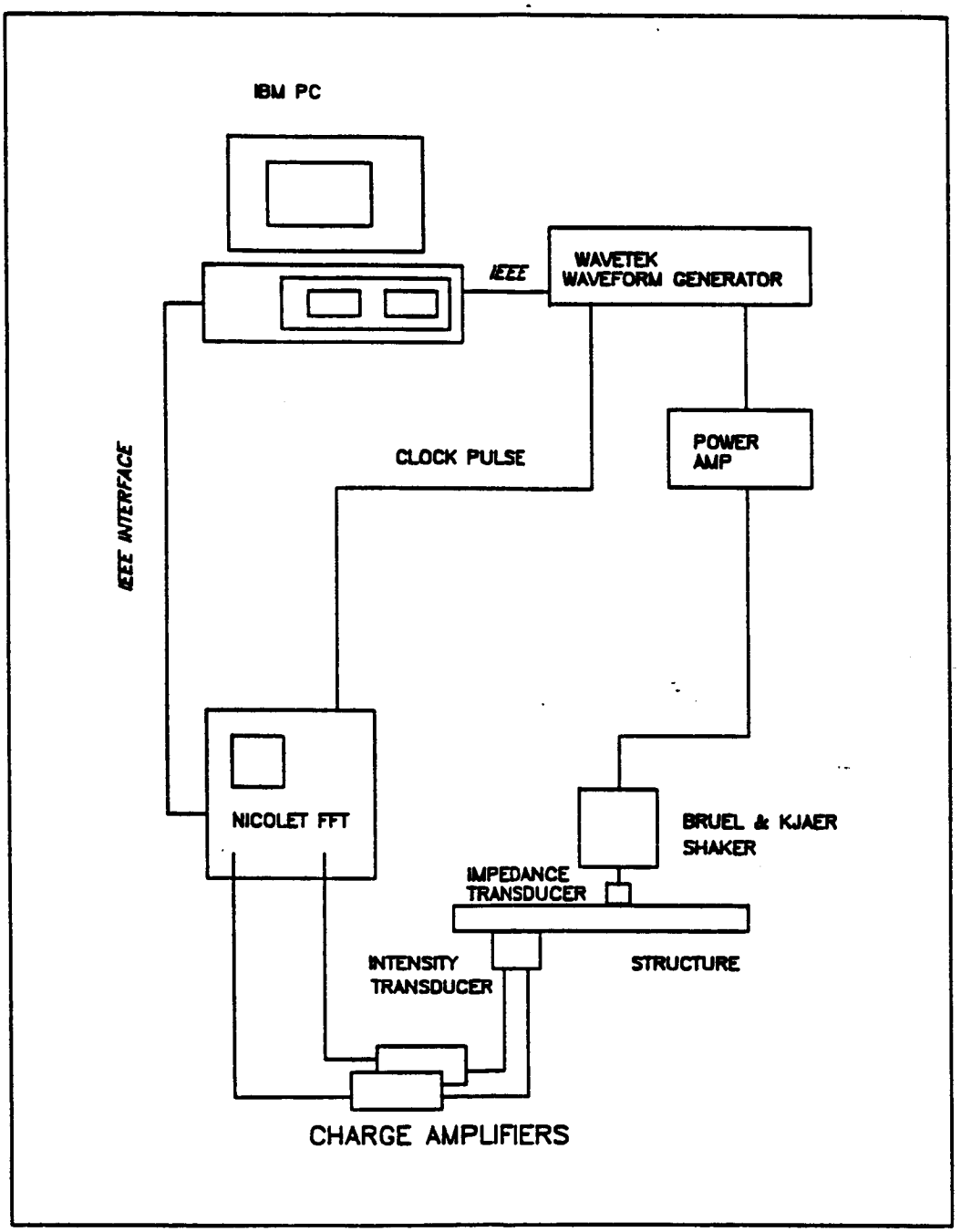

Figure 4.1 Experimental Apparatus Schematic

Table 4.1 Equipment and Transducers

	Description	Manufacturer	Model No.	Comment
1.	2 Accelerometers	PCB	303A	ICP, 2.2 g
2.	4 Charge Amps	PCB	464A	Adjustable, Dual Mode
3.	Force Gauge	PCB	208A	
4.	Accelerometer	Bruel & Kjaer	4344	Voltage Mode, 2.5 g
5.	Impedance Head	Bruel & Kjaer	8001	
6.	Mini-Shaker	Bruel & Kjaer	4810	10 N
7.	Fast Fourier Analyzer	Nicolet	660A	Dual Channel
8.	Amplifier	Genrad	1308-A	Audio Oscillator
9.	Arbitrary Waveform Generator	Wavetek	75	

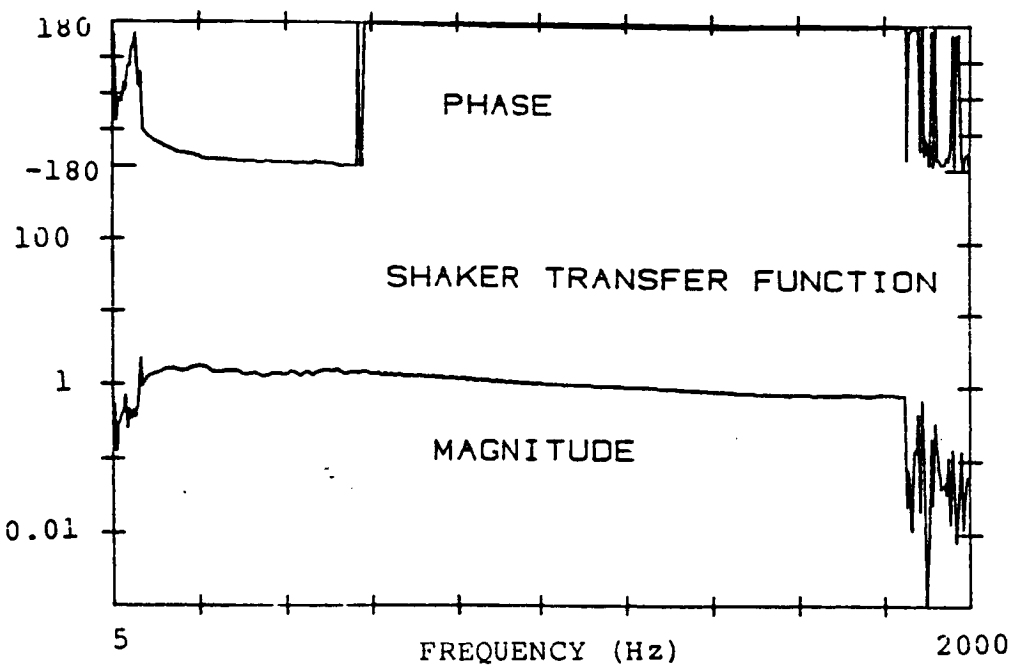

Figure 4.2 Shaker Transfer Function

of the connection to be above the maximum frequency of interest. The natural frequency of transverse vibration was found to be below the frequency range of interest.

The "structure" of figure 4.1 is either a beam or a plate. Further description can be found in section 4.6. The "intensity transducer" in figure 4.1 signifies the structural intensity probe composed of two accelerometers. A force gauge and accelerometer comprise the "impedance transducer".

The configuration of the structural intensity probe is illustrated in figure 4.3. It consists of two light-weight PCB accelerometers with built-in FET preamplifiers, an acrylic spacer, plus a nylon band and cyanoacrylate glue to secure the complete assembly. The total weight of the probe is 7.35 g. The accelerometers are spaced at .0127 m (0.5") center to center. The choice of spacing is particularly important and is discussed in section 4.6. If the spacing is too small, the phase difference between the accelerometers may be indistinguishable to the accelerometers. If the spacing is too large, the measurement will be limited to frequencies where the bending wavelength is at least 4 times the probe spacing.

The natural frequency of the accelerometers, 70 kHz, is of no concern since it is well above the frequency range of interest. The transfer function between the two

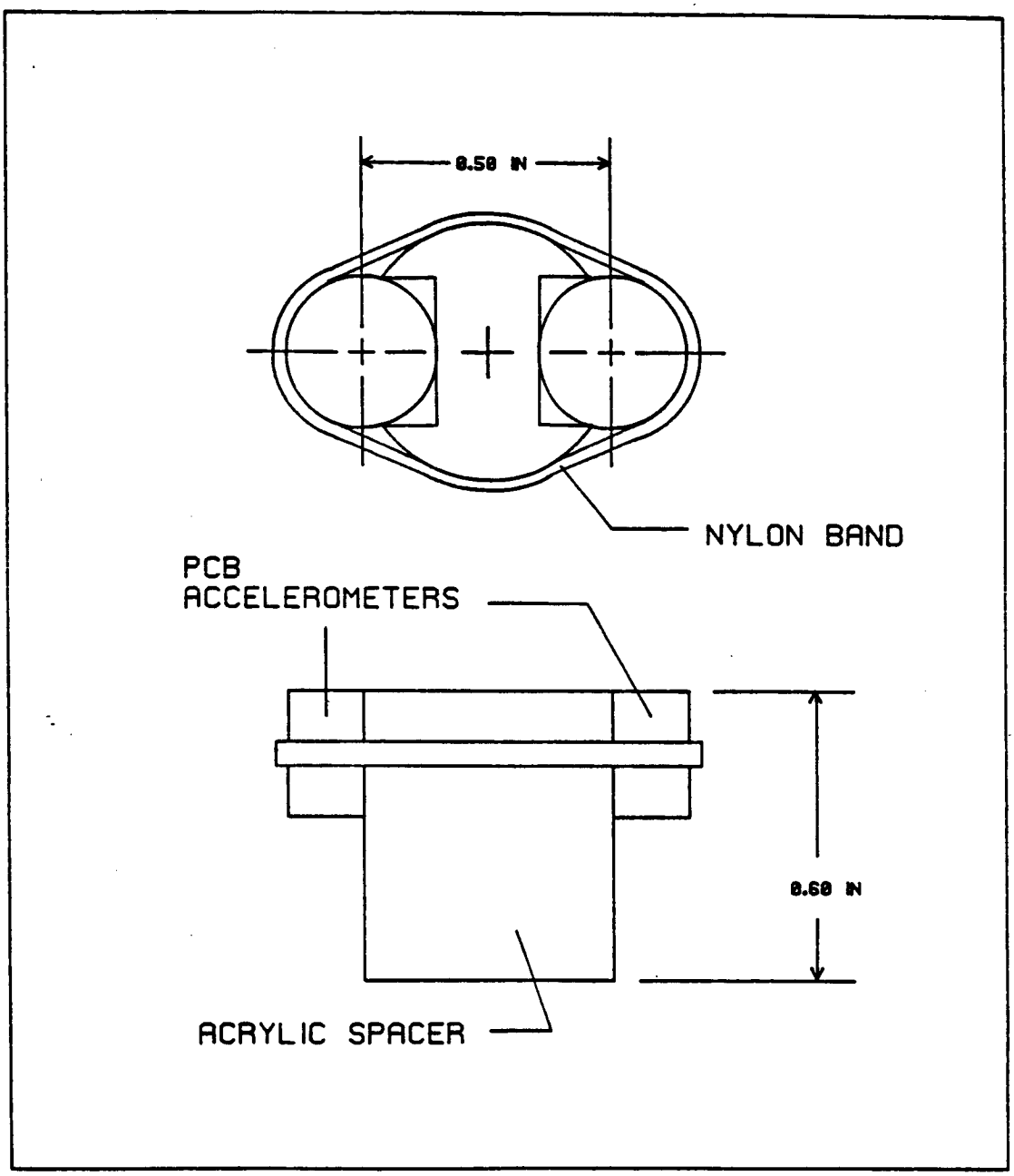

Figure 4.3 Probe Design Sketch

accelerometers channels in the probe configuration is shown in figure 4.4. The transfer function was obtained by fixing the probe with beeswax to the shaker table excited by the Schroeder-phased flat (constant amplitude) frequency spectrum signal, from 70 to 1850 Hz, described in section 4.3. The accelerometers appear to be well matched. In addition, no resonances of the intensity transducer due to its assembly appear to have been created. The height of the probe was kept minimal but functional to allow easy attachment to the test structures.

The arrangement of the force gauge and accelerometer is presented in detail in section 4.5.

The output of the "intensity or impedance transducer" was passed through variable gain, dual mode PCB amplifiers. The output signals were amplified and calibrated. The signal from the amplifier was then input to the Nicolet 660A FFT which performs the cross spectrum function central to the two accelerometer structural intensity method. The data held in the storage buffers of the Nicolet were passed to the microcomputer via an IEEE interface board where the intensity calculation is then performed.

4.3 Excitation

The choice of an excitation for the structures to be studied was based on statistical error considerations,

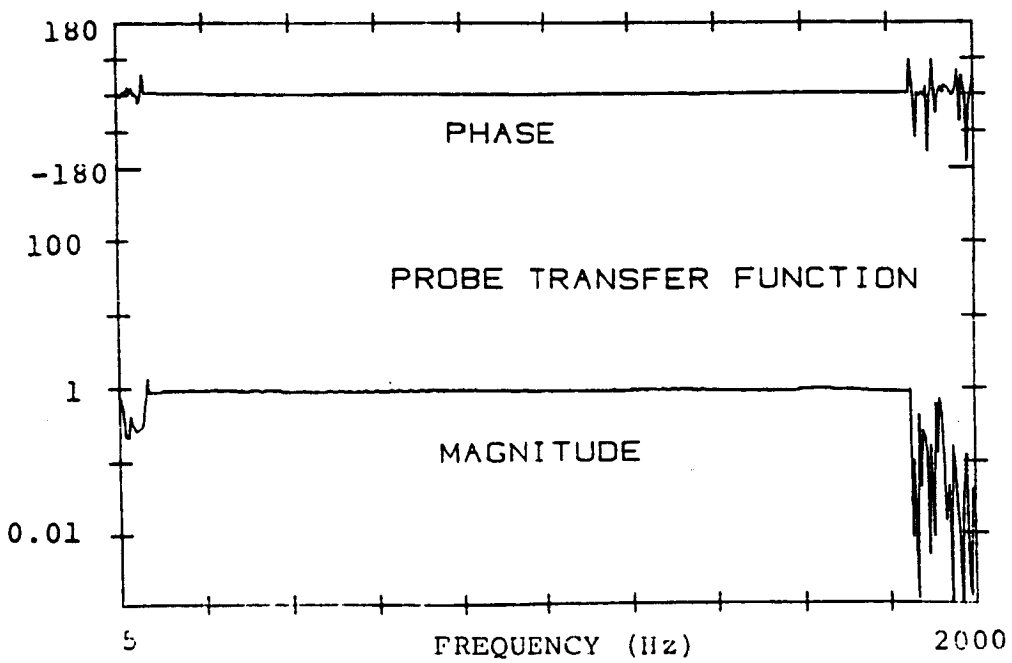

Figure 4.4 Transfer Function Between Probe Accelerometers

availability, dynamical properties of the tested structures and the simulated conditions of interest (frequency range).

Because the experimental technique is developed with aircraft type structures (especially panels) in mind, the excitation should reflect that encountered in noise fields surrounding light aircraft. Most aircraft panels without treatment are lightly damped and exhibit highly resonant behavior below 70 Hz. For propeller-driven aircraft, the blade-passage frequency falls in the range of 60-100 Hz and the first 15 overtones may be significant. The blade passage tones for the advanced turbo-prop will be higher, perhaps as high as 400 Hz. In most cases, the excitation can be severely limited below 70 Hz because such frequencies are not realistic for light aircraft.

The power spectrum of the excitation waveform is shown in figure 4.5. It is composed of discrete frequency components from 70 Hz to 1850 Hz in 5 Hz increments. The time history of the signal was calculated on a microcomputer using the equation:

$$x(t) = \sum_{f_1=70Hz,\Delta f=5Hz}^{f_u=1850Hz} \cos(2\pi f t) \qquad (4.1)$$

However, this signal will cause dynamic range problems when used in a practical application. It is clear that the amplitude of this function is much larger at t=0 and at

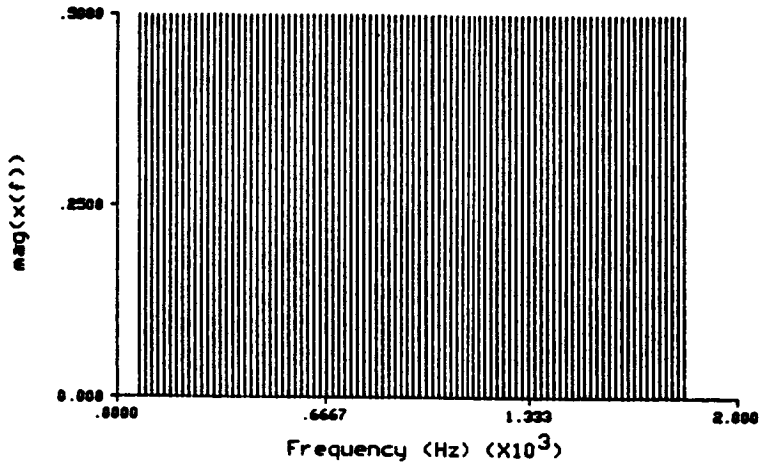

Figure 4.5 Excitation Signal Power Spectrum

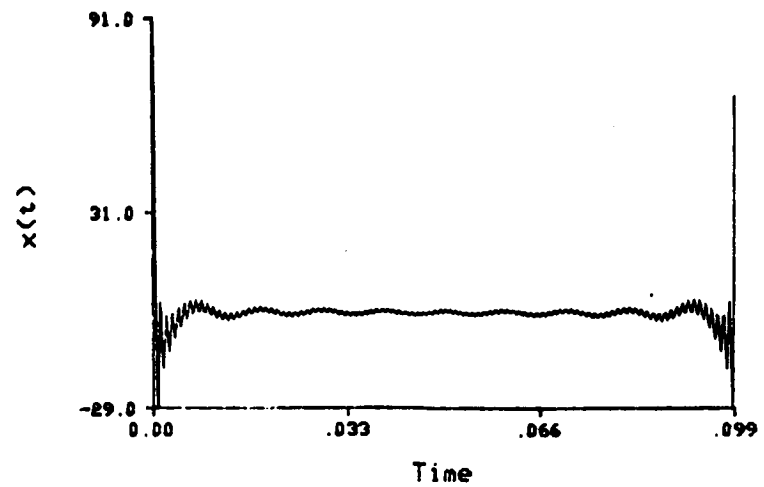

Figure 4.6 Zero-Phased Excitation Signal Time History

integral times of $1/\Delta f$ (with Δf as the frequency increment between components of the signal) than at all other times. This effect is shown in figure 4.6. To reduce the crest factor of the measurements, a technique known as Schroeder-phasing was employed.

4.3.1 Schroeder-Phasing Algorithm

Schroeder applied a scheme to phase components of a harmonic signal in such a way that energy is more evenly distributed through the time period resulting in larger dynamic range in measurement systems [26,6]. Concisely stated, Schroeder prescribed that the portion of the time (in a sampling period) spent at a certain frequency be proportional to the amplitude of that frequency. Since in this study a "flat" spectrum was desired, the algorithm prescribed that the time for all frequency components be equal and hence the phase of the nth component (or harmonic) be:

$$\Phi_n = 2\pi \sum_{i=1}^{n} i \qquad (4.2)$$

The Schroeder-phased time history is calculated with the following expression:

$$x(t) = \sum_{f_l=70Hz,\Delta f=5Hz}^{f_u=1850Hz} \cos(2\pi f\ t + \Phi_n) \quad n=1,2,3.. \qquad (4.3)$$

The result of this phasing is shown in figure 4.7. The power spectrum of the zero-phased signal and the Schroeder-phased signal were compared by inputting the signals to the arbitrary waveform generator and then to the Nicolet FFT. The S/N of the phased signal was 15 dB higher than that of the zero-phased signal. The Schroeder-phased signal was used in power comparison experiments on three different structures as described in section 4.6.1. The intensity mapping experiments of a point-driven plate described in section 4.7 were run before the implementation of the Schroeder-phased signal. The excitation for the plate tests was provided by a GenRad random noise generator and amplifier.

As with the acoustical intensity measurements, the equation for intensity assumed single-frequency measurements and then was generalized to include excitation of some finite bandwidth. Redman-White, who used analog measurements, cautions that the error will depend heavily on the power spectral density of excitation utilized. He recommends using a bandwidth ratio (df/f) of less than 0.3.[24] The recommendation is satisfied in this investigation because the excitation signal is composed of discrete frequencies and not a band of frequencies. Therefore the quantity df is very small and the ratio is less than 0.3.

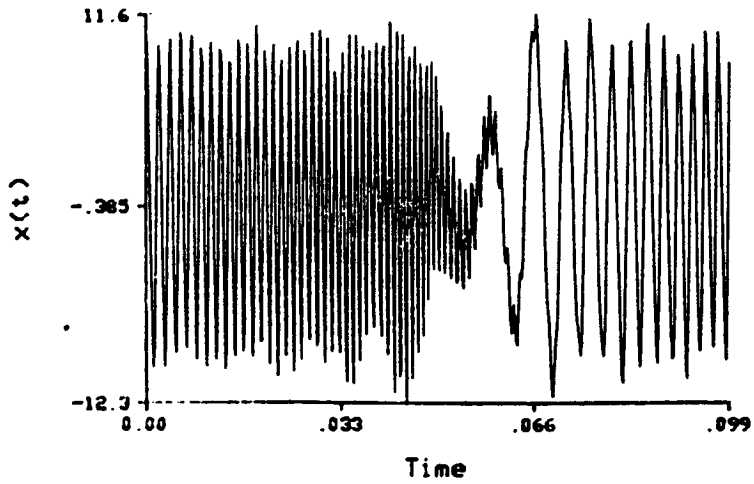

Figure 4.7 Schroeder-Phased Excitation Signal Time History

4.4 Contour Integration

To determine the validity of the structural intensity measurements, the power injected into the test structures was determined by the intensity measurements and by using an impedance transducer. The intensity measurements from a contour surrounding the source (shaker) were integrated to obtain injected power according to :

$$\pi_{in} = \frac{(d) \sum_{i=1}^{n} I_n}{n} \qquad (4.4)$$

where n is the number of intensity locations, I_n is the intensity value at the at the nth location, and d is the length of the contour. For the plate, d = 2 π * radius of the enclosing circle; the radius in all plate experiments was 15.24 cm (6"). For a beam the intensity probe was placed at two different distances (for two different trials) from the source, 30.48 cm (12") and 60.96 cm (24"). The 30.48 cm tests are not included in this report because they are very similar to the 60.96 cm tests. The contour length is d = 2 * width in both cases. The probe was always oriented perpendicular to the integration contour. Intensity measurements were taken at 12 equally spaced locations about the circumference of the circle, thus at every 30° .

4.5 Power Determination From a Force Gauge and Accelerometer

The means of determining the injected power independent to the intensity method is by use of a force gauge and accelerometer. Assuming there are no twisting moments or bending moments applied to the structure, such measurements can be used to compute power into the structure. Special care was used in aligning transducers, the shaker and mounting studs. A flexible piece, described in section 4.2, was used to connect the shaker to the force gauge to reduce the applied moments. The shaker mounting arrangement is depicted in figure 4.8. A labelled sketch of the transducer configuration is shown in figure 4.9 . The power is calculated as follows:

$$\pi_{in} = \frac{1}{2} \text{Re} \ (F \cdot V^{*})$$

$$\pi_{in} = \frac{1}{2} \text{Re} \ (F \cdot \frac{A^{*}}{j\omega})$$

$$\pi_{in} = \frac{-\text{Im}(\ S_{12} \ )}{2\omega} \qquad (4.5)$$

where in this case S_{12} is the cross spectrum between the force and acceleration signals. The verification plots comparing the power obtained both ways is presented in the section 4.6.

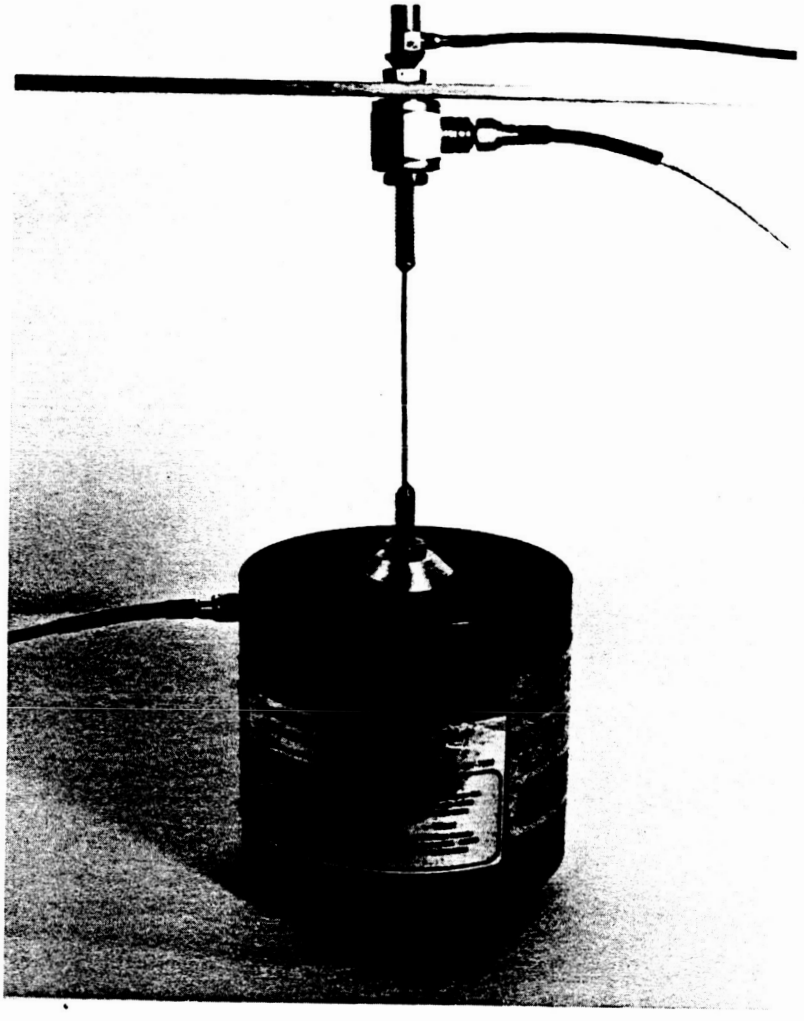

Figure 4.8 Experimental Shaker Mounting and Power Sensing Configuration

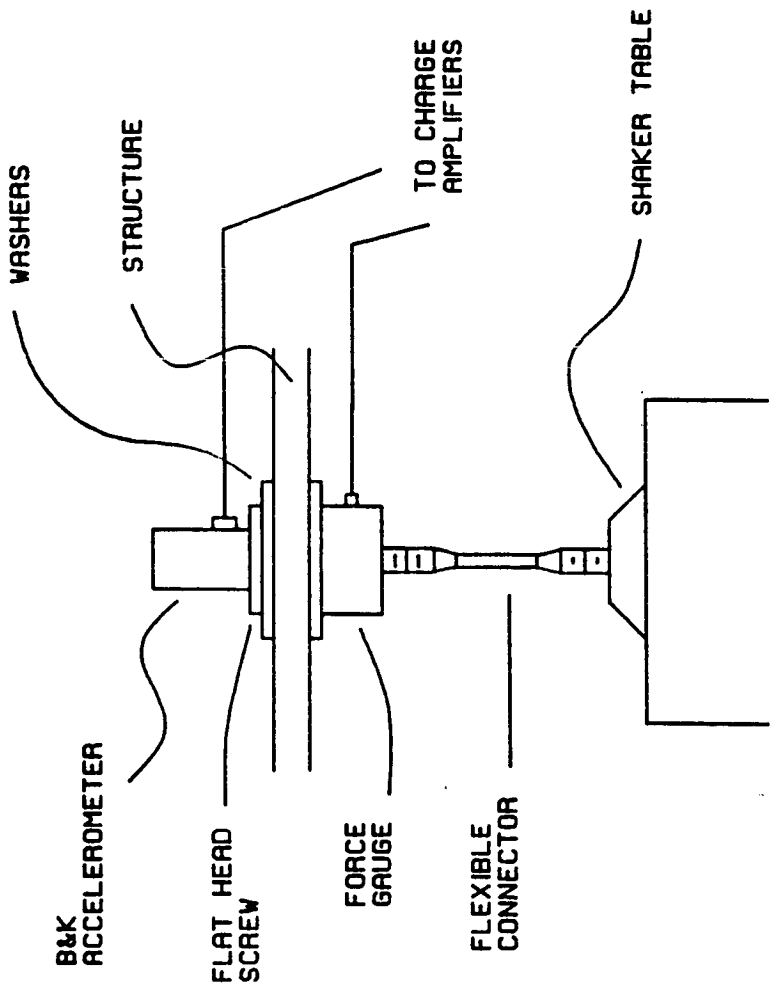

Figure 4.9 Detail Sketch of Shaker Mounting Scheme

4.6 Structures Under Investigation

Two beams and a plate were used to investigate the two accelerometer method of determining the power injected into a structure. The injected power computed using the structural intensity technique described in section 4.4 is compared with the power computed using an impedance-type measurement of section 4.5.

The characteristics of the test structures used to validate the structural intensity method are shown in table 4.2. The beams were arranged as shown in figure 4.10. Figure 4.11 shows the galvanized steel sand containers and a portion of the beam in a typical test configuration. To provide significant power flow, sand completely enclosed 3 feet of the ends of the beam which was excited at the center. In frequency domain measurements of the input point accelerance, the ratio of the acceleration to input force, large power flow was evident by heavily damped resonant peaks and phase angles between 10 and 120°.

The plate was tested as shown in figure 4.12. The plate used in the experiments is illustrated in figure 4.13. Many means to encourage power flow in the plate proved to be unsuccessful. The lack of resonant behavior and the phase angle between input force and acceleration were used as criterion for judging the extent of power flow. A variety of different durometer rubber pads and foams of

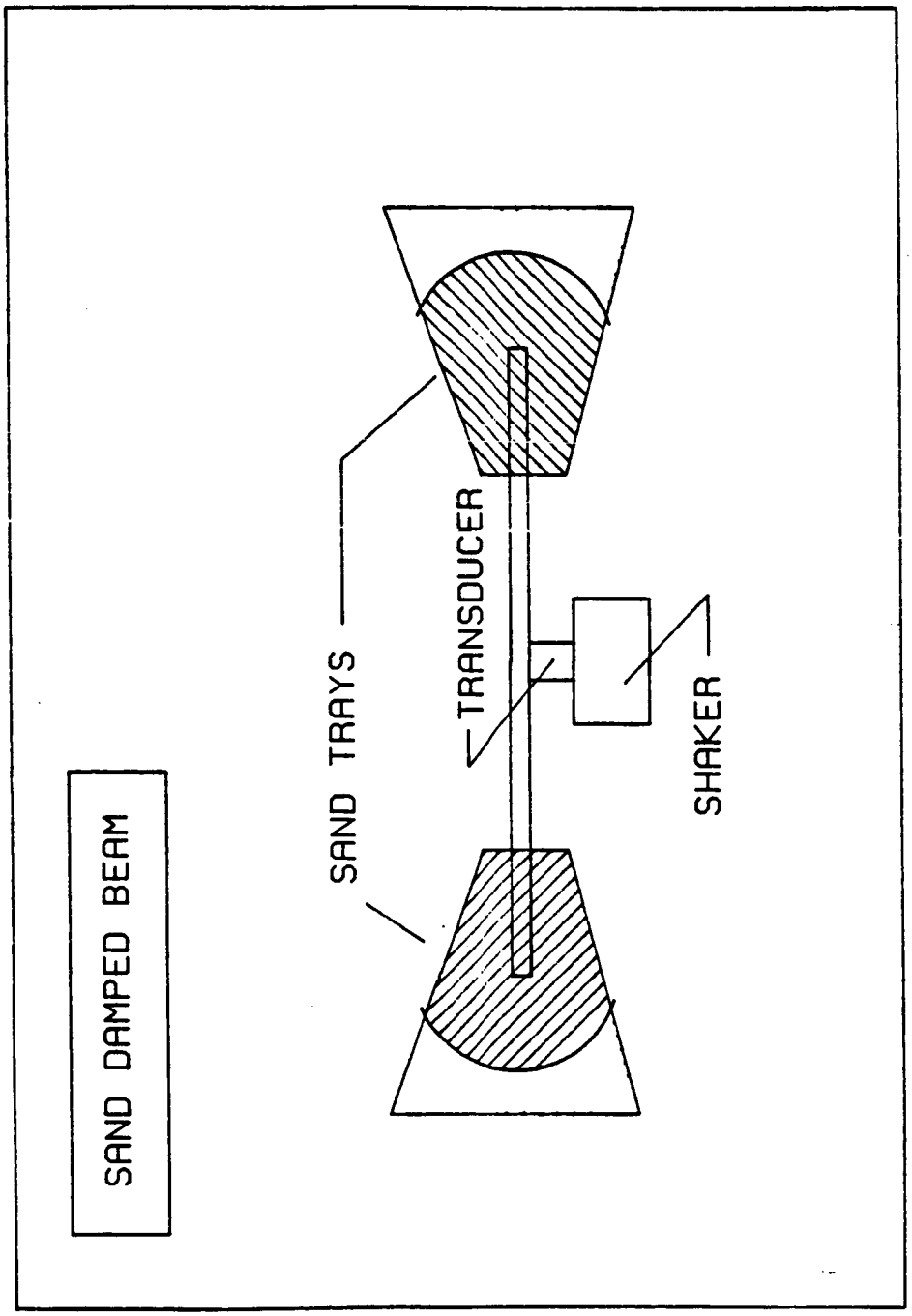

Figure 4.10 Apparatus for Beam Experiments

Figure 4.11 Beam Experimental Apparatus

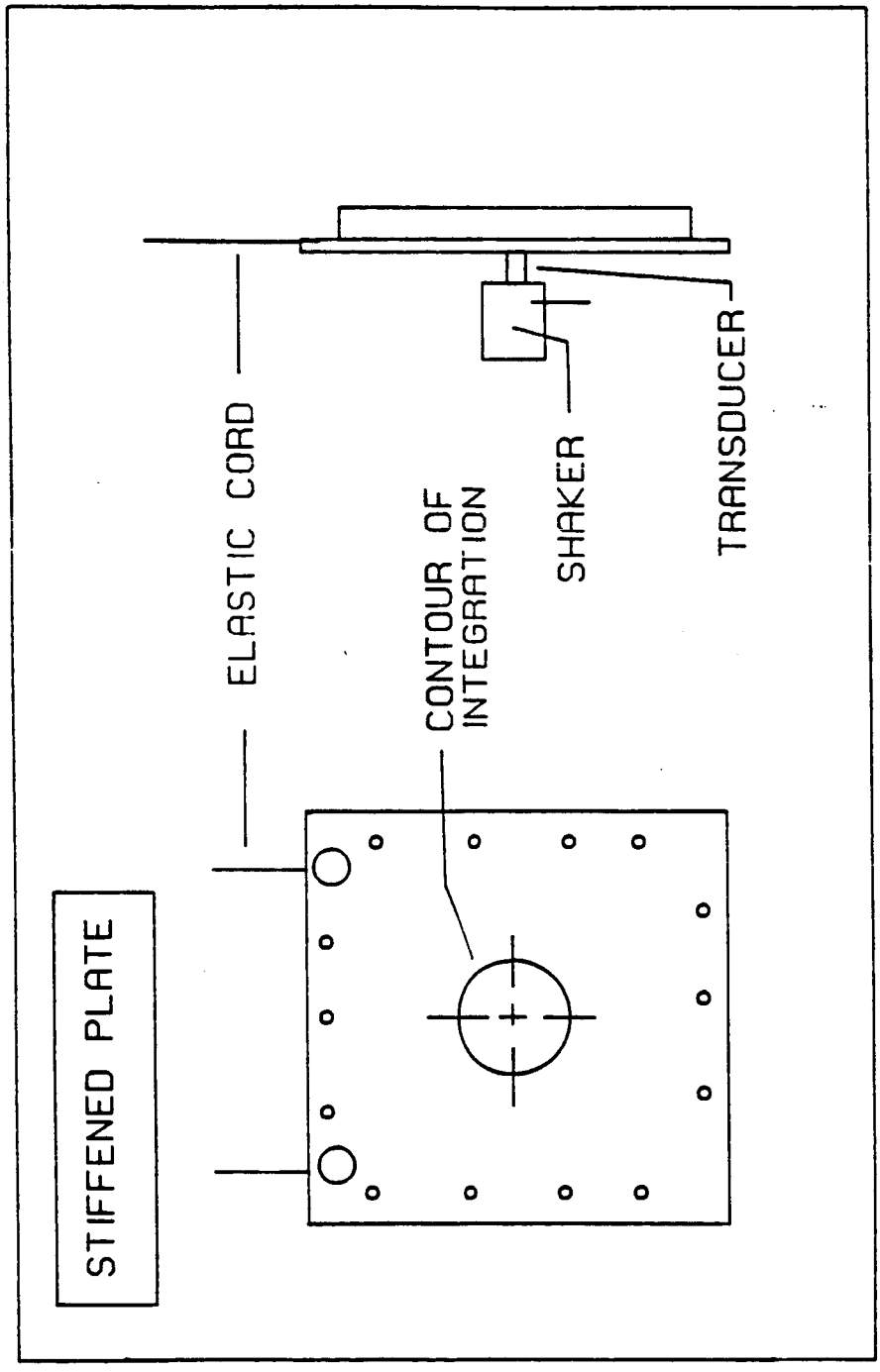

Figure 4.12 Apparatus for Plate Experiments

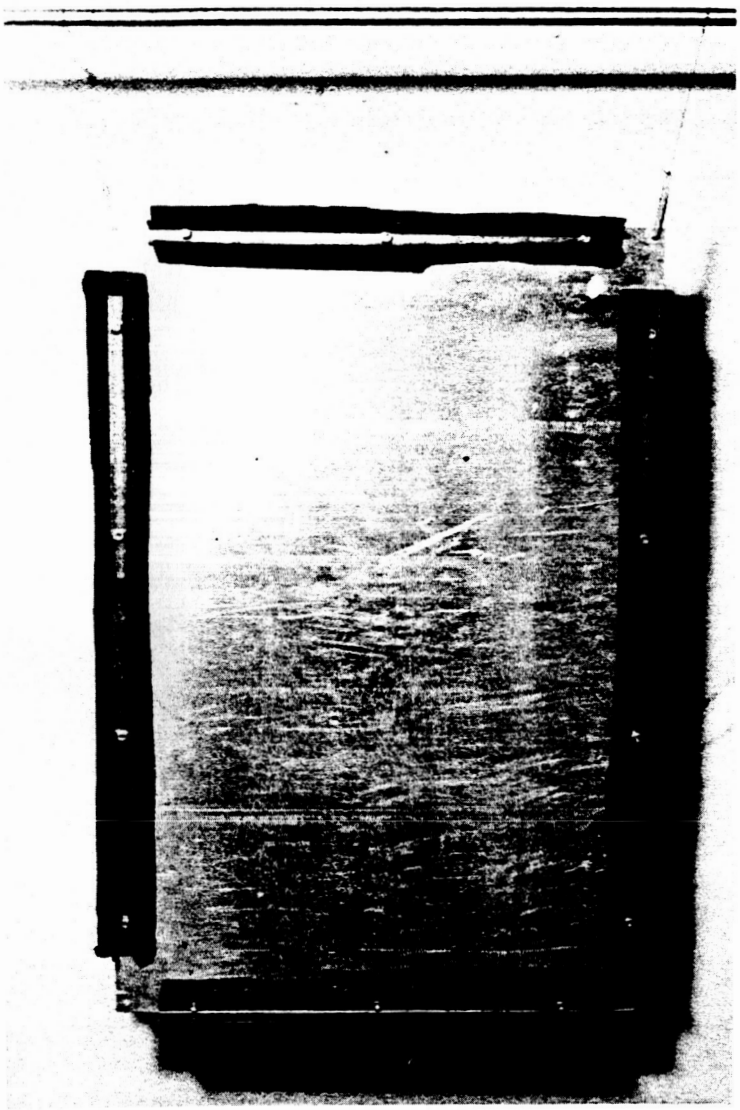

Figure 4.13 Test Plate

various amounts of reticulation were layered to form a stack. Two similar stacks, one on each side of the plate captivated by a single bolt running through one stack, the plate and the other stack were used. Even with several combinations of foam and rubber and varying amount of fastening screw torque, phase differences were no more than 10°. The same was true when a beam secured to the bottom edge of the plate was terminated in a container of water or sand. In addition, capped medical syringes secured to the plate and fixed at the other end were tested to no avail. The lack of a consistently effective damping system introduce errors which result from taking measurements in a highly reactive field as will be described in section 4.8.4.

Table 4.2 Description of Structures

Structure	Dimensions (in.)	Material
Plate	36 x 24 x 1/16	7075 T6 Al
1" Beam	168x 1 x 1/8	6061 T6 Al
3" Beam	96 x 3 x 1/16	7075 T6 Al

4.6.1 Intensity in a Plate

The methods of determining the power injected in the plate are compared in figure 4.14. The general shape of the two curves is encouraging but the rather large discrepancy of 20 dB may be attributed to many factors. These factors will be addressed in the next subsection where much better agreement was obtained. A major factor was found to lie with the influence of the probe in the vibration field.

The phase between the force gauge and accelerometer is shown in figure 4.15. Throughout the experiments, the phase was monitored to give an indication of the mechanical power supplied by the shaker. The greater the phase difference from 0° or 180°, the greater the power injected into the plate.

For the sake of completeness, one should refer to figure 4.16, the ratio of probe spacing to wavelength versus frequency, when evaluating the comparison of power. The ratio indicates what frequency range 0.5" probe spacing is appropriate. The spacing should be at least 1/20 of the wavelength but not more than 1/4 of the wavelength. Above 1/4 wavelength, the finite difference approximation fails and below 1/20, the phase difference at the accelerometers of the travelling wave may not be discerned by the two accelerometers. For the plate used in this test, the acceptable range is 400 Hz to greater than 2000 Hz.

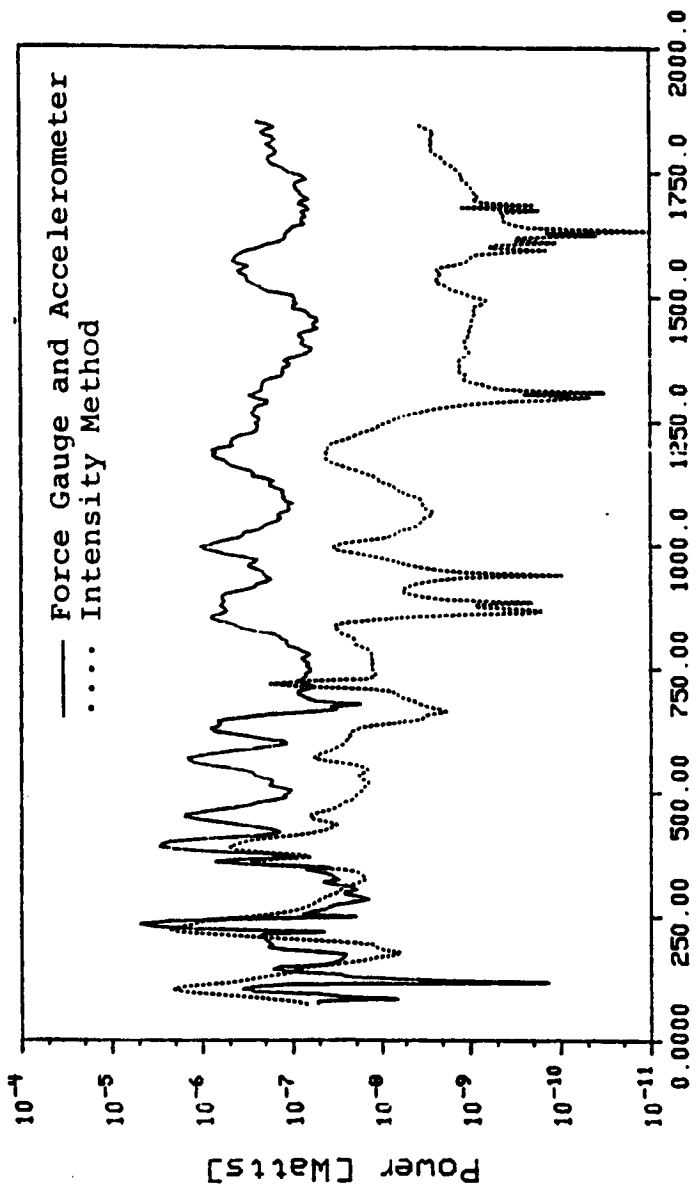

Figure 4.14 Comparison of Injected Power into a Plate for Two Experimental Methods

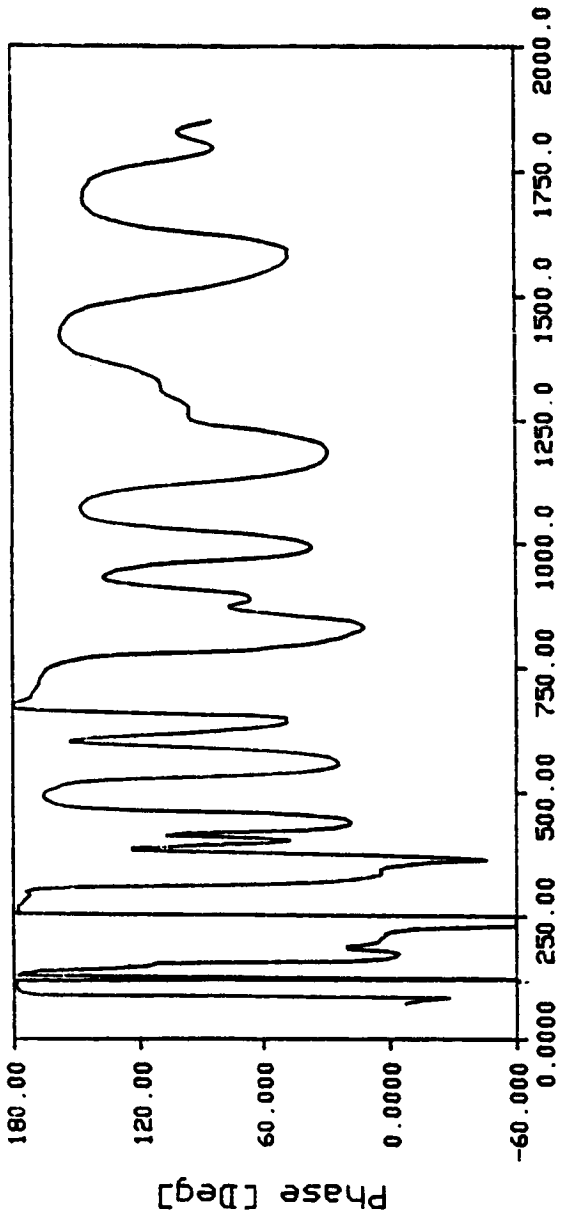

Figure 4.15 Phase Angle Between the Force Gauge and Accelerometer for a Plate

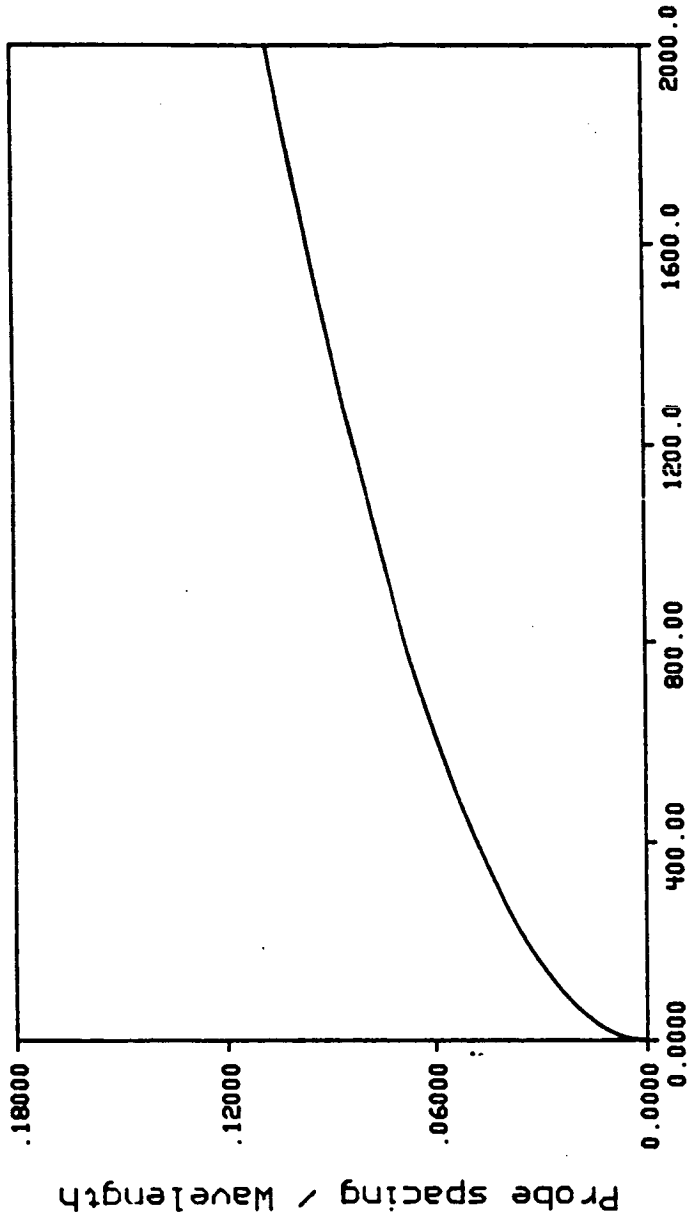

Figure 4.16 The Ratio of Probe Spacing to Wavelength Versus Frequency for a Plate With a Thickness of 1/16"

4.6.2 Intensity in a Beam

4.6.2.1 3 Inch Wide Beam

The two independent methods of calculating the power injected into the 3" beam are compared in figure 4.17. The large disagreement was a consequence of inconsistent mechanical power flow due to the repositioning of the probe with each measurement. Figure 4.18 shows the comparison of the same methods when accounting for the inertial properties of the probe. The more favorable agreement between methods when compared to the analogous plot for the plate (figure 4.14) or the uncompensated beam (figure 4.17) lies in the fact that the probe's effect was considered. The contour integration consisted of 6 intensity measurements, 3 across the width of the beam on the two sides of the source, 12" from the source.

As a measure of power flow, figure 4.19 shows the phase angle difference between the force and acceleration transducers. While the phase difference was as high as 120° at a narrow portion of the frequency spectrum, it generally hovered at about $\ddot{20}^{\circ}$. Much energy was transmitted from exciter to sand at the natural frequencies of the beam up to 1200 Hz. Between natural frequencies, the sand damping system, still absorbed significant power flow.

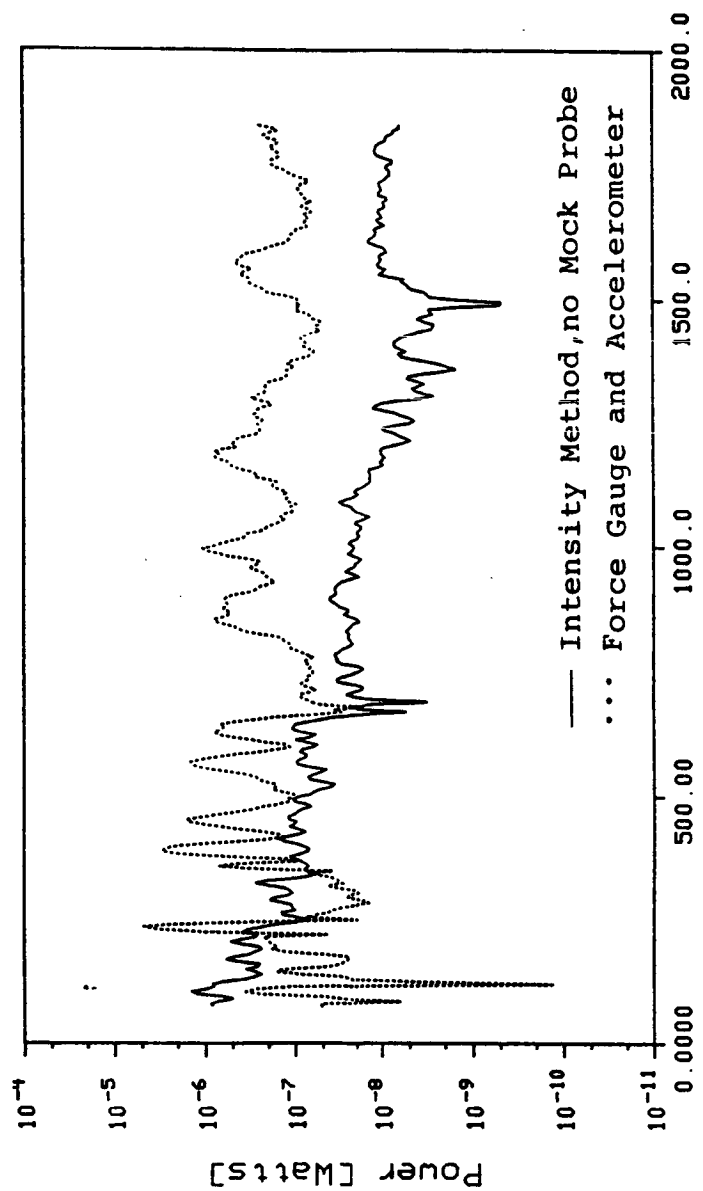

Figure 4.17 Comparison of Injected Power into a 3" Wide Beam for Two Experimental Methods Without Accounting for Probe Inertial Properties

C-2

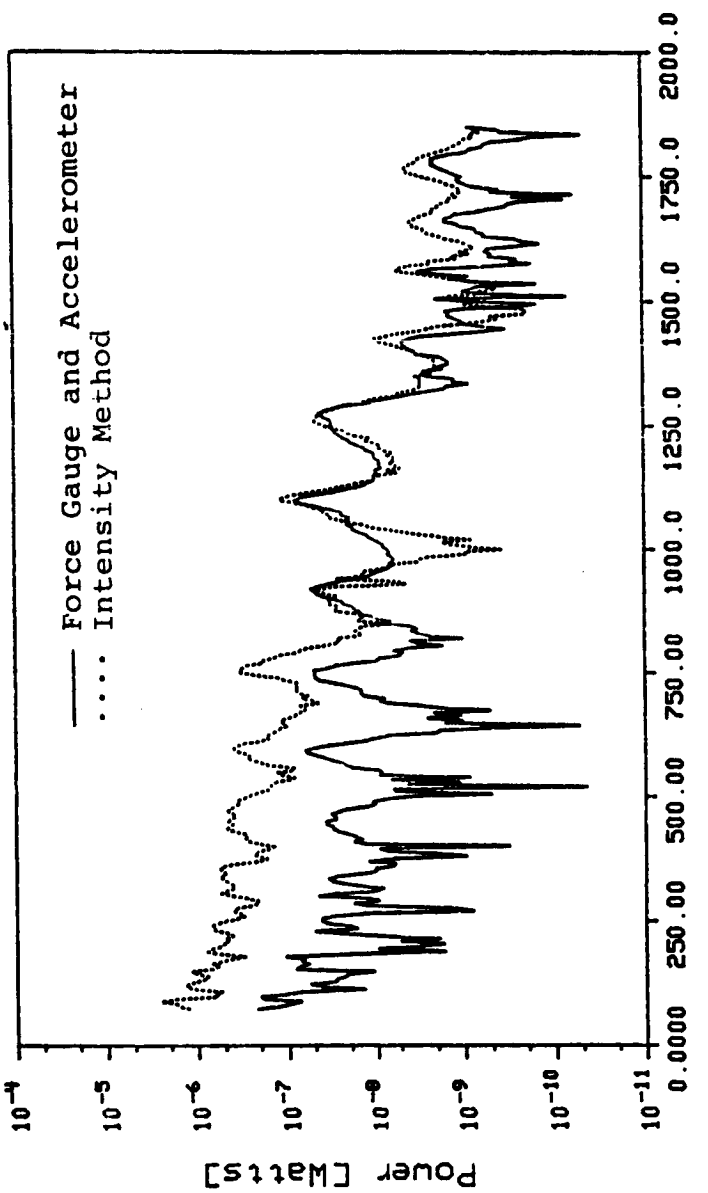

Figure 4.18 Comparison of Injected Power into a 3" Wide Beam for Two Experimental Methods

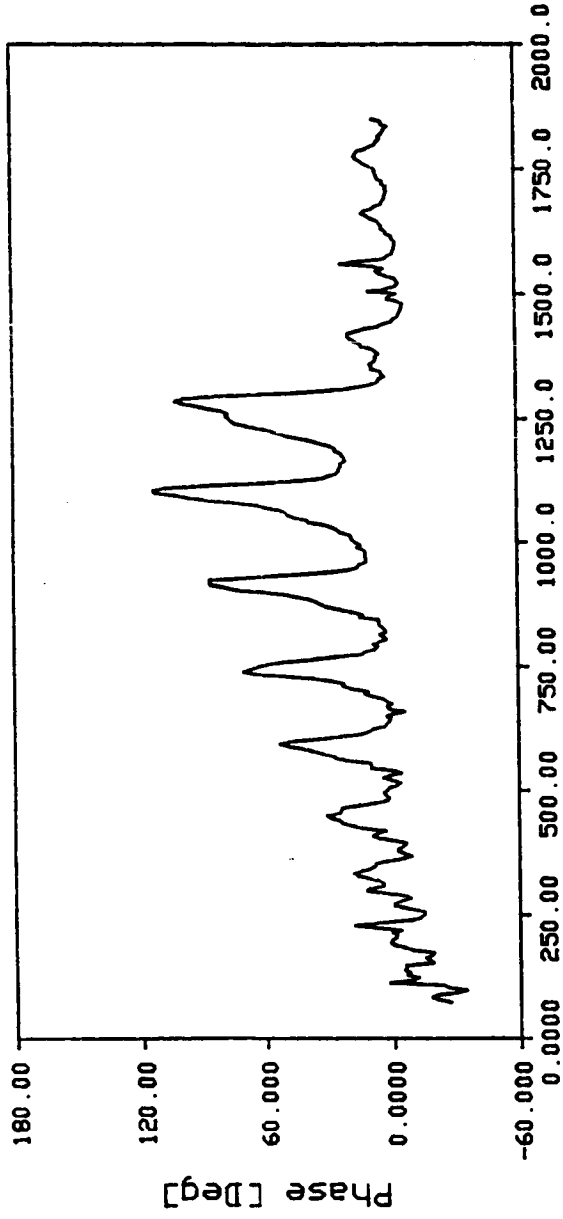

Figure 4.19 Phase Angle Between the Force Gauge and Accelerometer for a 3" Wide Beam

Mock probes were placed at all the locations in the integration contour except where the actual probe was located during a measurement. The mock probes were fabricated of acrylic spacers (identical to that used in the actual probe) and clay of roughly the same weight distribution as two accelerometers. The mock probes and the actual probe are shown in figure 4.20. The acrylic spacer provided consistent bonding characteristics among probes and the clay provided similar inertial properties as the accelerometers. The mechanical power and phase were monitored with each movement of the probe to a new location and are plotted superimposed in figures 4.21 and 4.22. The curves show some variations but are encouraging since they indicate that consistent power flow is maintained. A comparison between the mechanical power when the probe was attached and the mechanical power when the probe was removed is given in section 4.8.3.

Analytically, the modal density for the 3" wide beam is fairly high in the frequency range of interest, containing about 15 natural frequencies. The ratio of probe spacing to wavelength versus frequency for a beam of this size is shown in figure 4.23. The 0.5" probe spacing is 1/20 the wavelength at 120 Hz and is approximately 1/6 the wavelength at 2000 Hz.

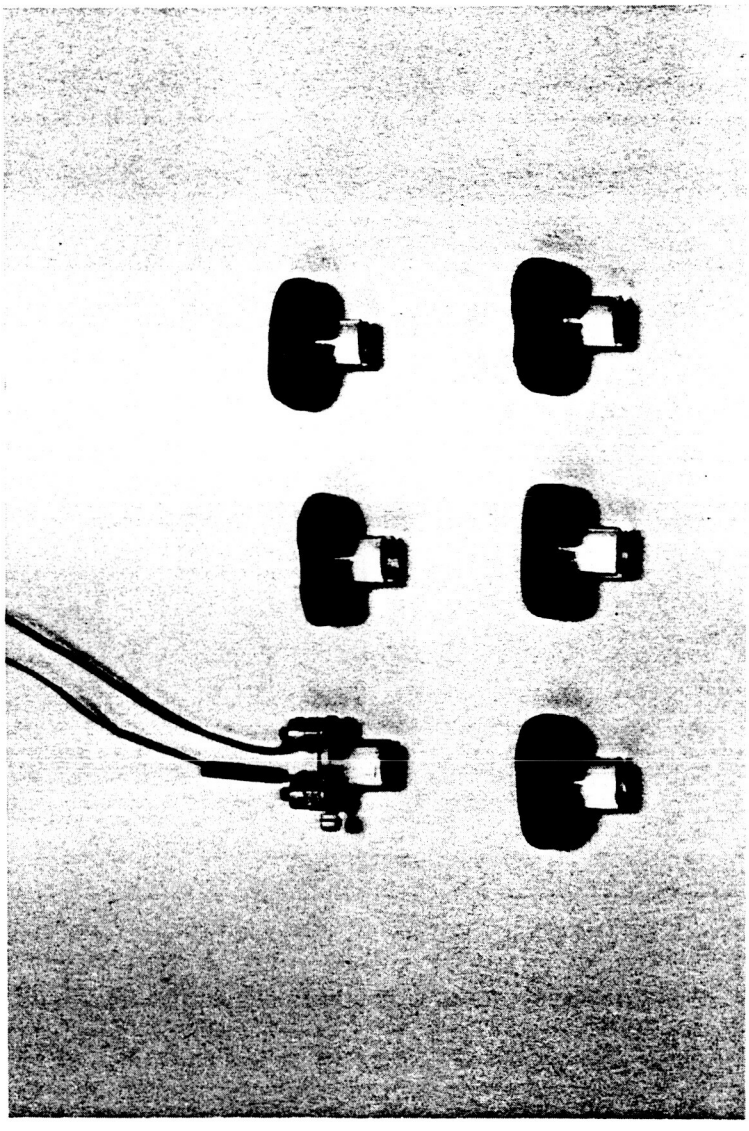

Figure 4.20 Actual Probe with Mock Probes

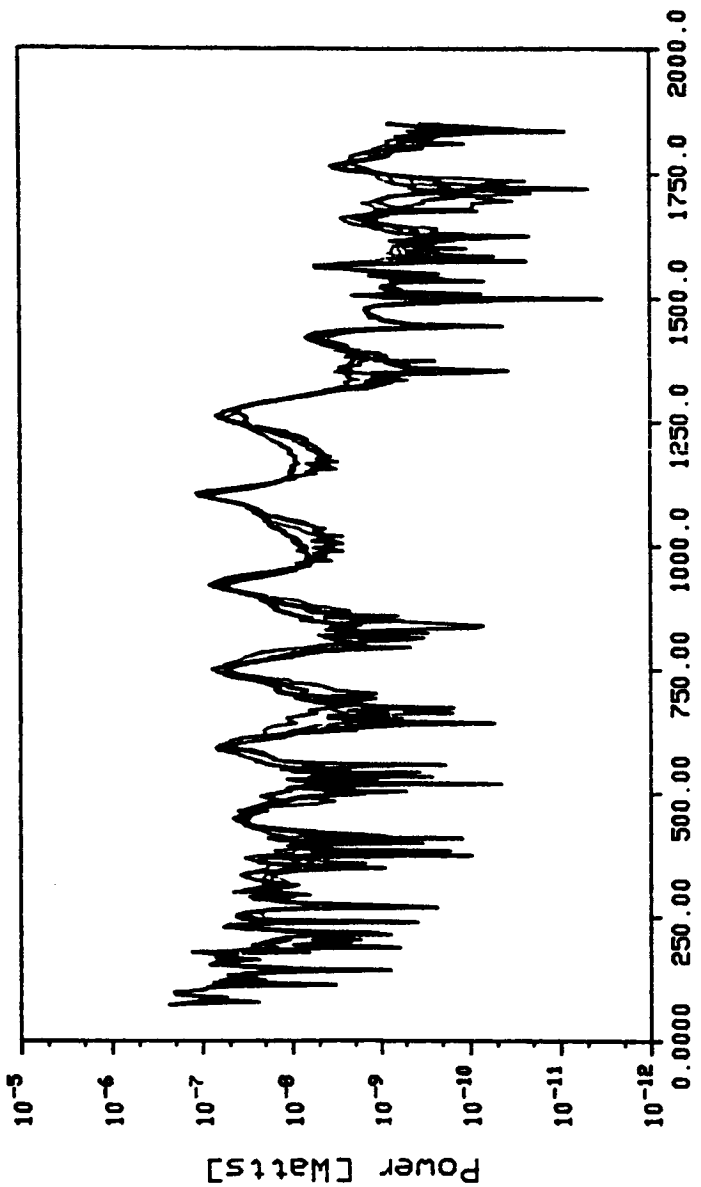

Figure 4.21 F*V Power for Each of Six Probe Locations

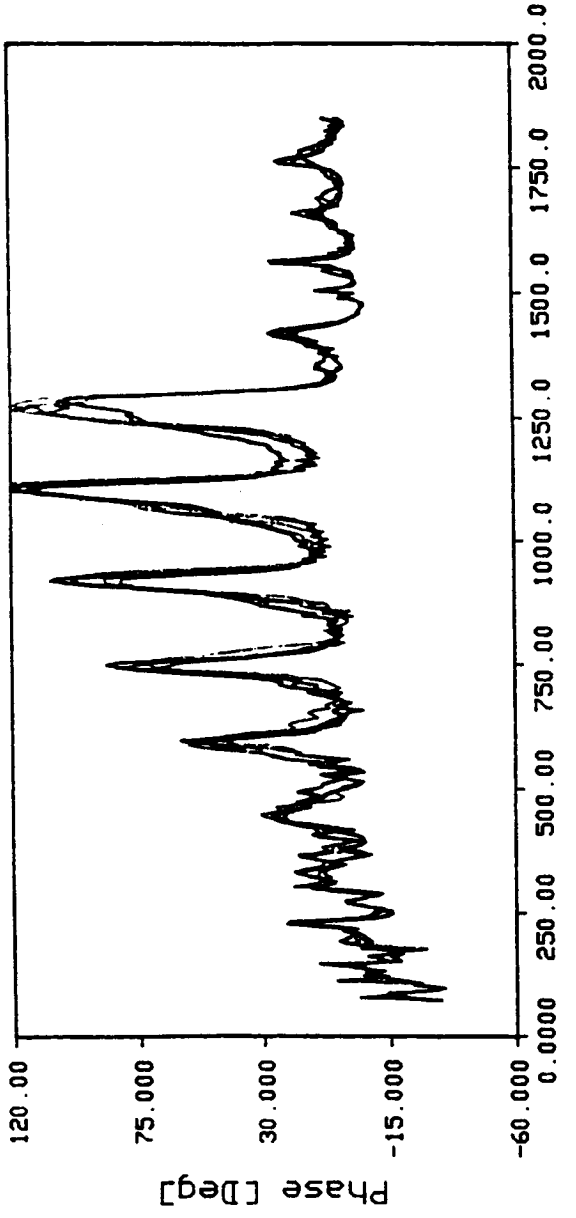

Figure 4.22 F*V Phase for Each of Six Probe Locations

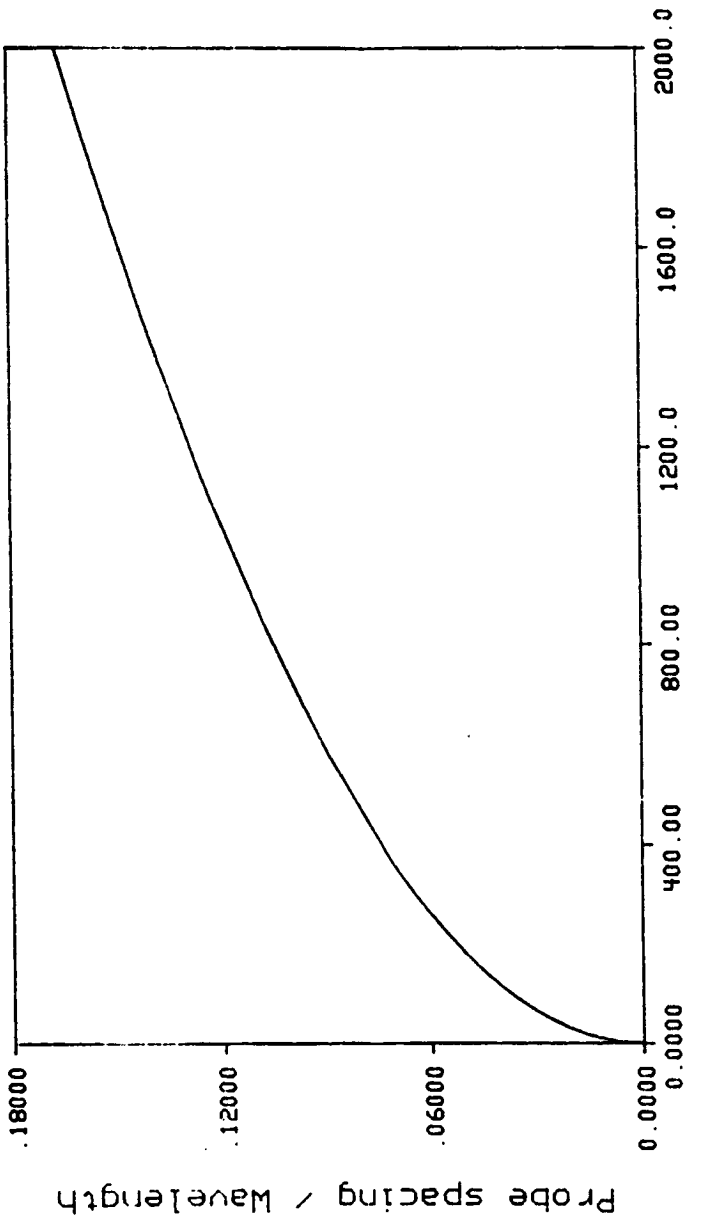

Figure 4.23 The Ratio of Probe Spacing to Wavelength Versus Frequency for a 3" Wide Beam

4.6.2.2 1 Inch Wide Beam

The power comparisons and phase for the 1" wide beam is shown in figures 4.24 and 4.25 respectively. A mock probe was also used for the measurements. Figure 4.25 also shows that the phase difference between the force and acceleration gauges is nearly identical with either the actual or mock probe fixed to the beam. The similar phase differences indicate that consistent power flow was maintained in the structural intensity measurements.

The discrepancies found in the power comparisons are very similar to those found in the 3" beam. The intensity was only measured at 1 point on each side of the source, 12" from the source. One mock probe was used to maintain consistent power flow during the measurements.

One common technique for increasing the dynamic range and eliminate the effects of channel mismatch in the acoustical intensity method and used in this investigation is transducer switching. In the probe switching technique, measurements are taken at each location with the intensity probe switched in orientation. The instrumentation channel connection to the probe is unchanged during the switching. The actual intensity should only change in sign but the instrumentation error between channels remains constant. By subtracting these two measured values of intensity and dividing in half, one is left with the true value of

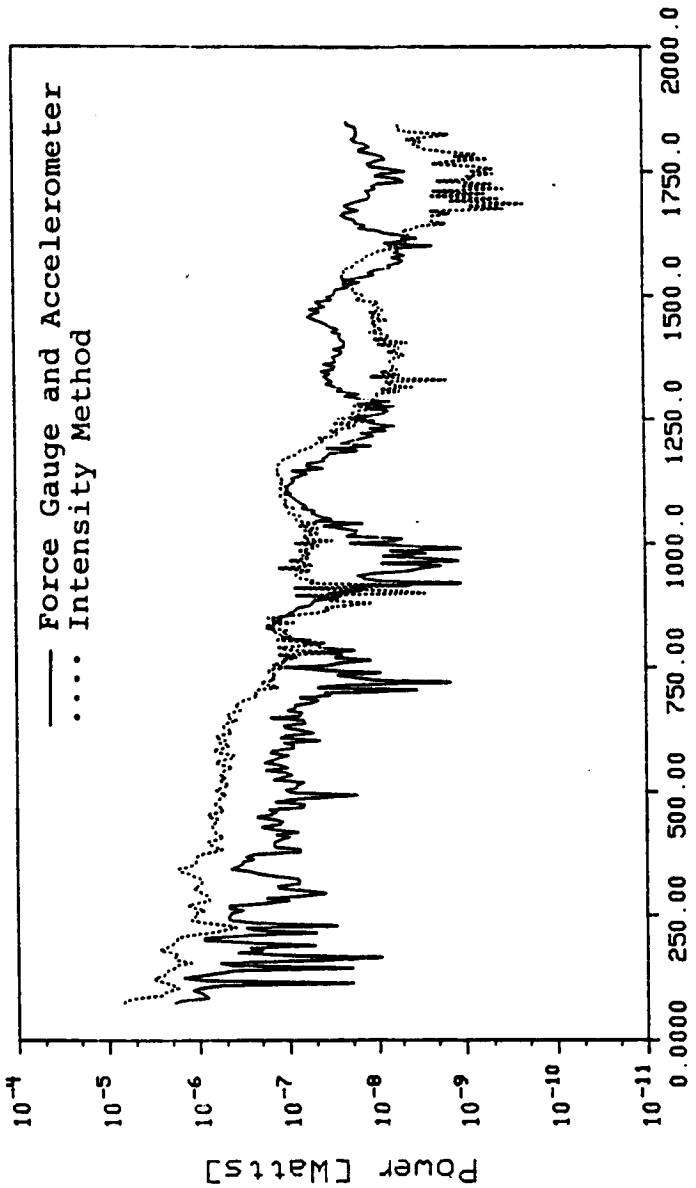

Figure 4.24 Comparison of Injected Power into a 1" Wide Beam for Two Experimental Methods

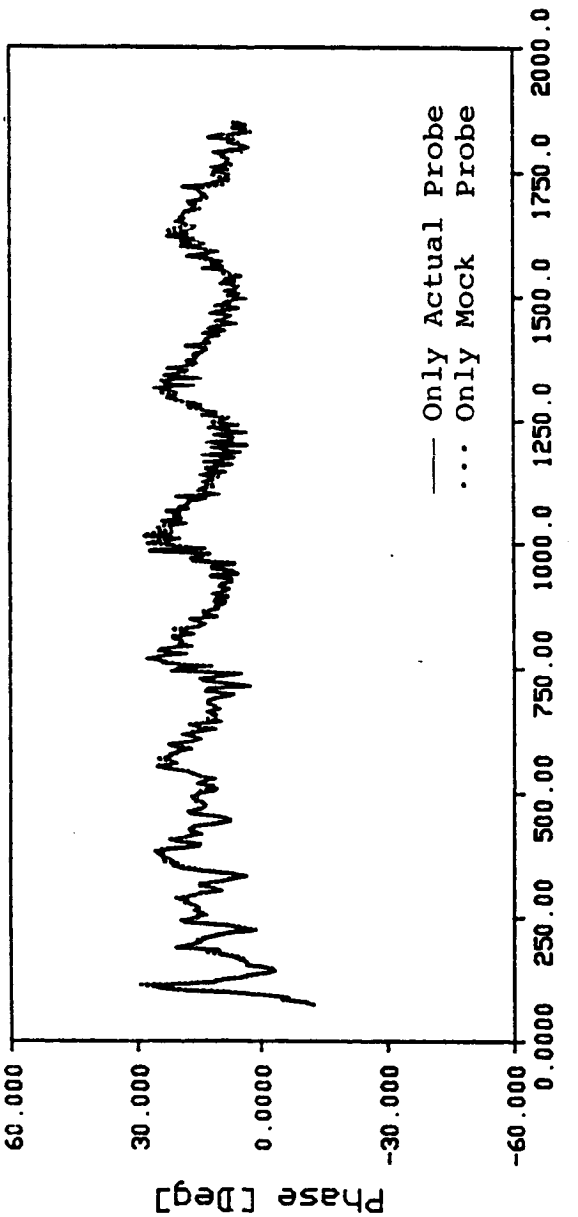

Figure 4.25 Phase Angle with Only Actual Probe Attached and With Only Mock Probe Attached

intensity. The switching technique is explained further by Waser and Crocker [34]. The power comparison and phase difference utilizing probe switching is shown in figure 4.26 and 4.27. The mock probe was used to maintain consistent power flow. Much of the 7 dB error in the high frequency range is absent and a slight improvement in the low frequency range occurs when the probe switching technique is used.

As with the previous beam, the modal density is high in the frequency range of interest with about 11 natural frequencies in the range. To gain insight into probe size considerations, a plot of the probe spacing versus wavelength in the 1" beam is included as figure 4.28. The ratio is 1/20 at about 200 Hz and is 1/10 at 1850 Hz.

Based on power comparisons with an independent means of measurement, the structural intensity method can supply accurate values as long as necessary precautions are taken. The precautions include having some form of compensation for noise and transducer mismatch like probe switching, using the proper excitation and accounting for the probe's inertial properties.

4.7 Intensity Vector Mapping of a Plate

A sketch of the test set-up for the stiffened aluminum plate used for intensity mapping experiments is shown in

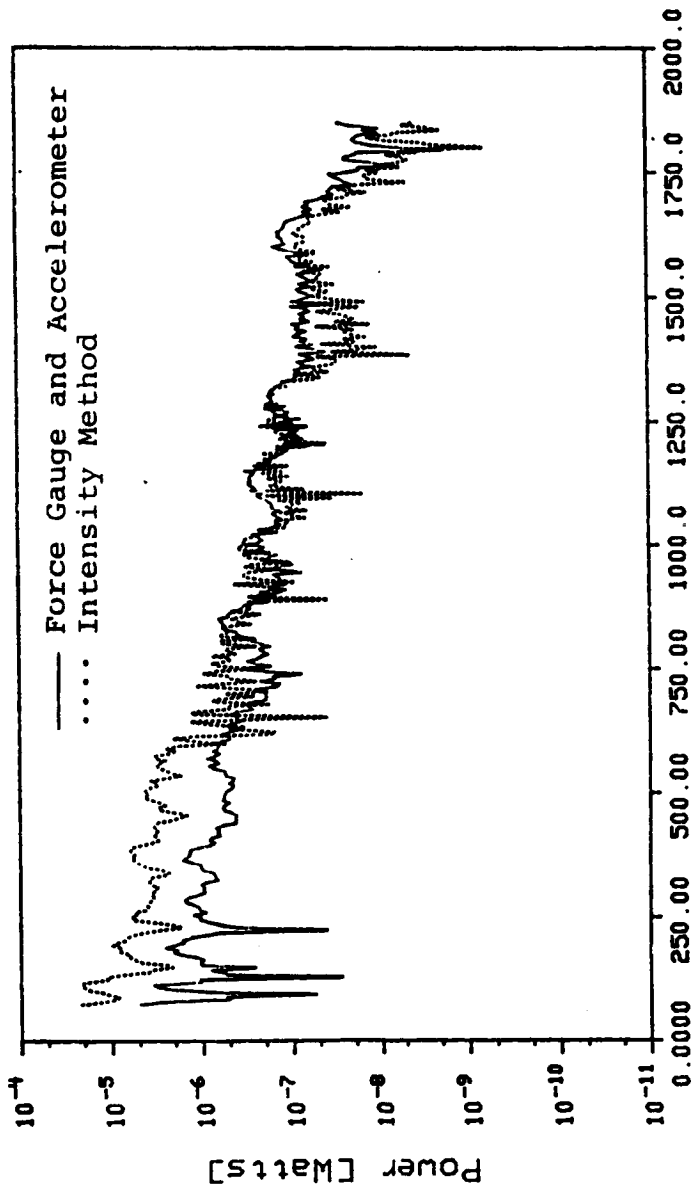

Figure 4.26 Comparison of Injected Power into a 1" Wide Beam for Two Experimental Methods Utilizing Probe Switching

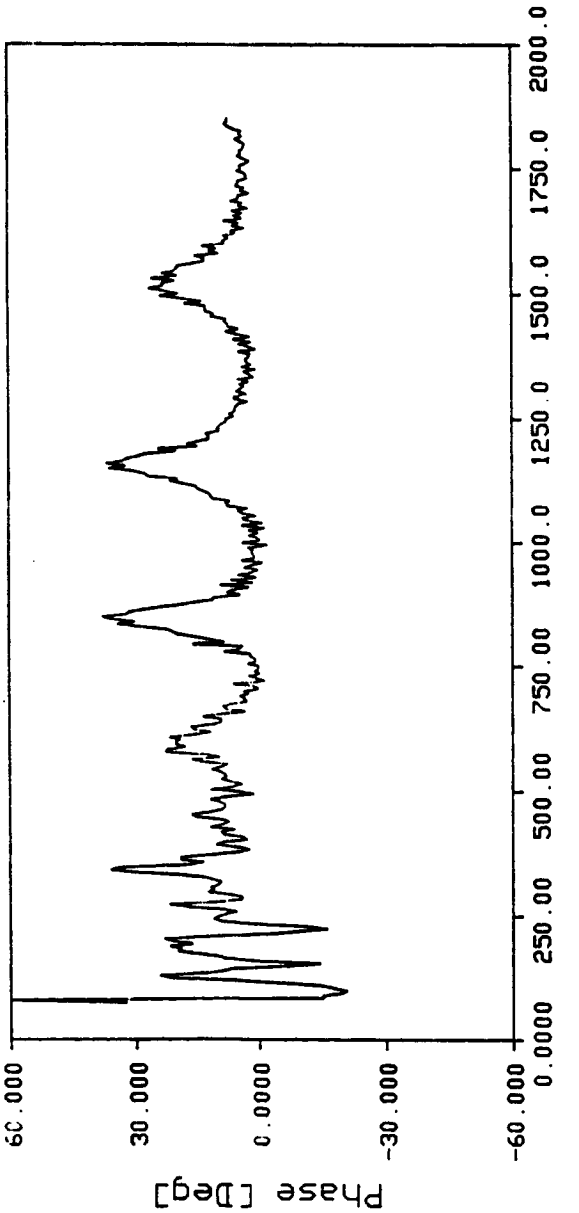

Figure 4.27 Phase Angle Between the Force Gauge and Accelerometer for a 1" Wide Beam Utilizing Probe Switching

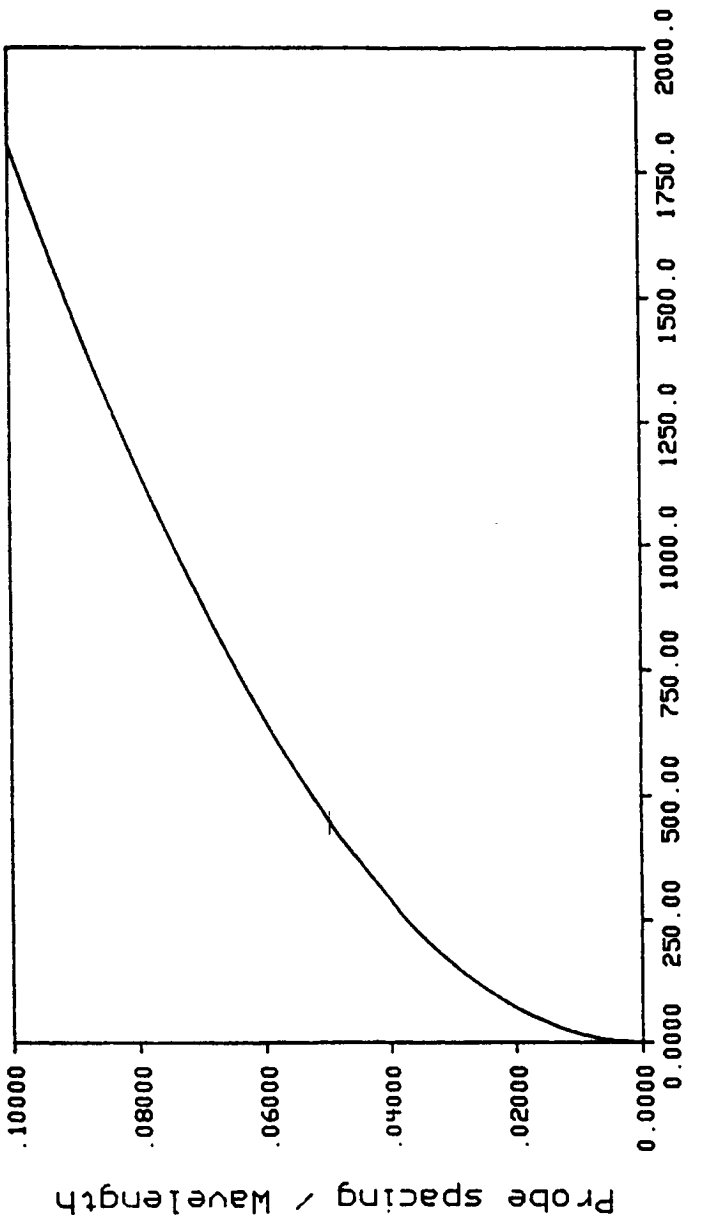

Figure 4.28 The Ratio of Probe Spacing to Wavelength Versus Frequency for a 1" Wide Beam

figure 4.29. The plate was discretized in a 2" by 2" grid of 135 locations over the surface. The excitation was bandlimited white noise supplied by a random noise generator. At each location, the structural intensity probe was fixed with beeswax and an intensity measurement taken, first parallel with the x coordinate direction and then with the y coordinate direction. No dummy transducers were used.

Some typical plots are shown in figures 4.30 to 4.35. The source, a shaker, is denoted by "0" in the figure, and the energy sink, a passive (no excitation) shaker, is represented by "S". The vectors also indicate that energy transport can take a tortuous path depending upon the frequency of analysis. While in most plots it is clear where the source and sink are located, the magnitude of the intensity (the length of the arrow) for some locations appears to be inappropriate. Theoretically, the intensity should diminish with distance from the source due to internal damping and a small amount of energy loss due to radiation to the surrounding air space. In addition, no energy should be transmitted across the plate edges.

As mentioned in section 4.3, one encounters problems in the use of broadband excitation. The questionable results may also be attributed to the inconsistent damping provided at the stiffening angle irons. The passive shaker

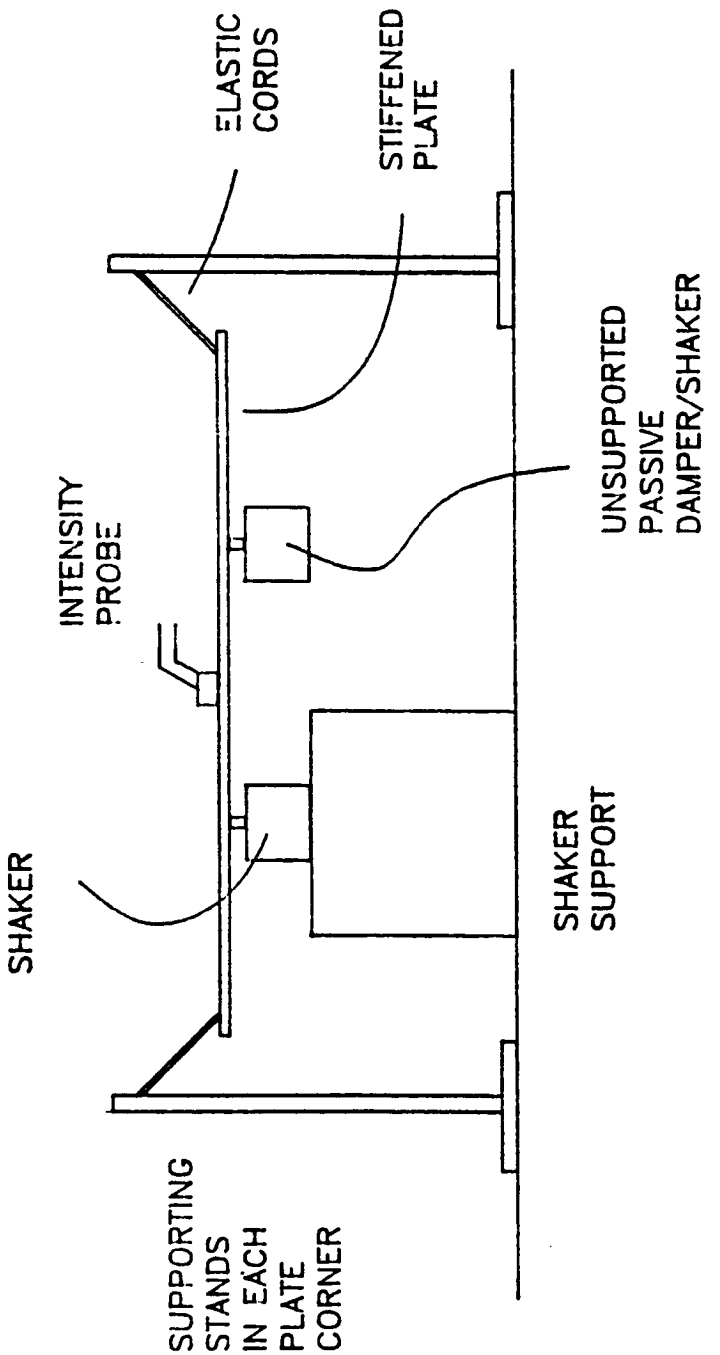

Figure 4.29 Aluminum Plate Used in Intensity Mapping Experiments

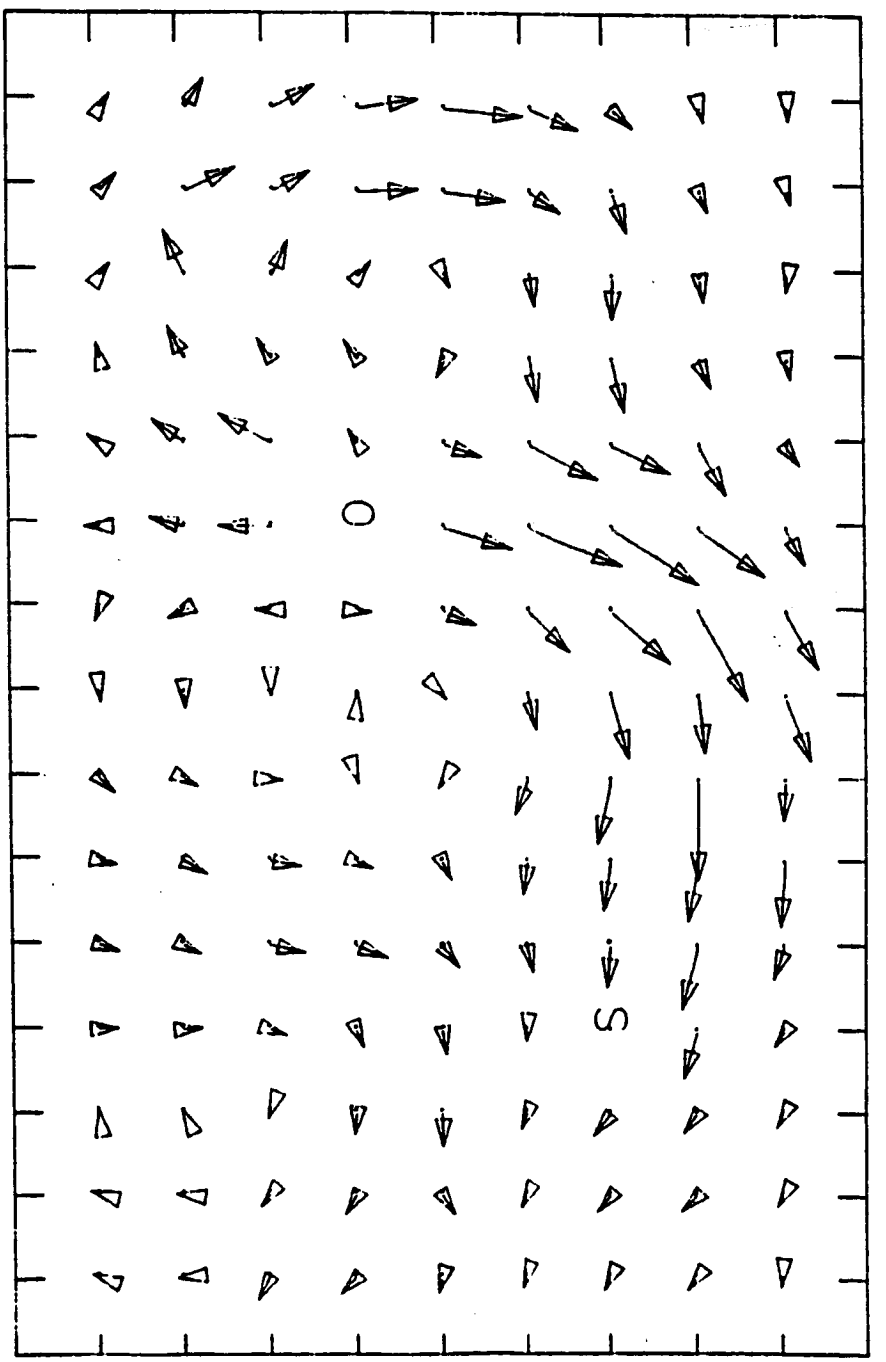

Figure 4.30 Intensity Mapping for the Plate at 100 Hz

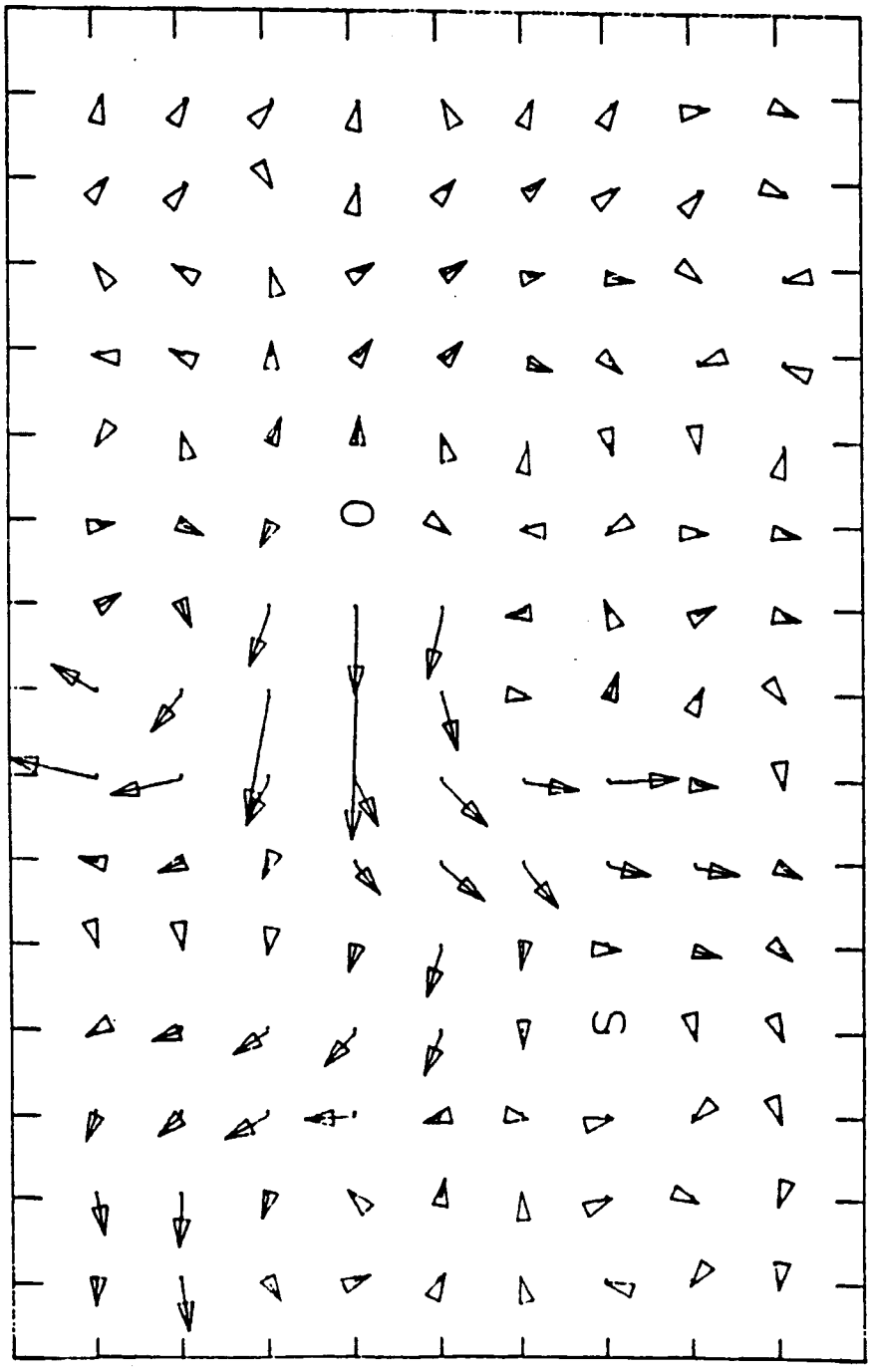

Figure 4.31 Intensity Mapping for the Plate at 175 Hz

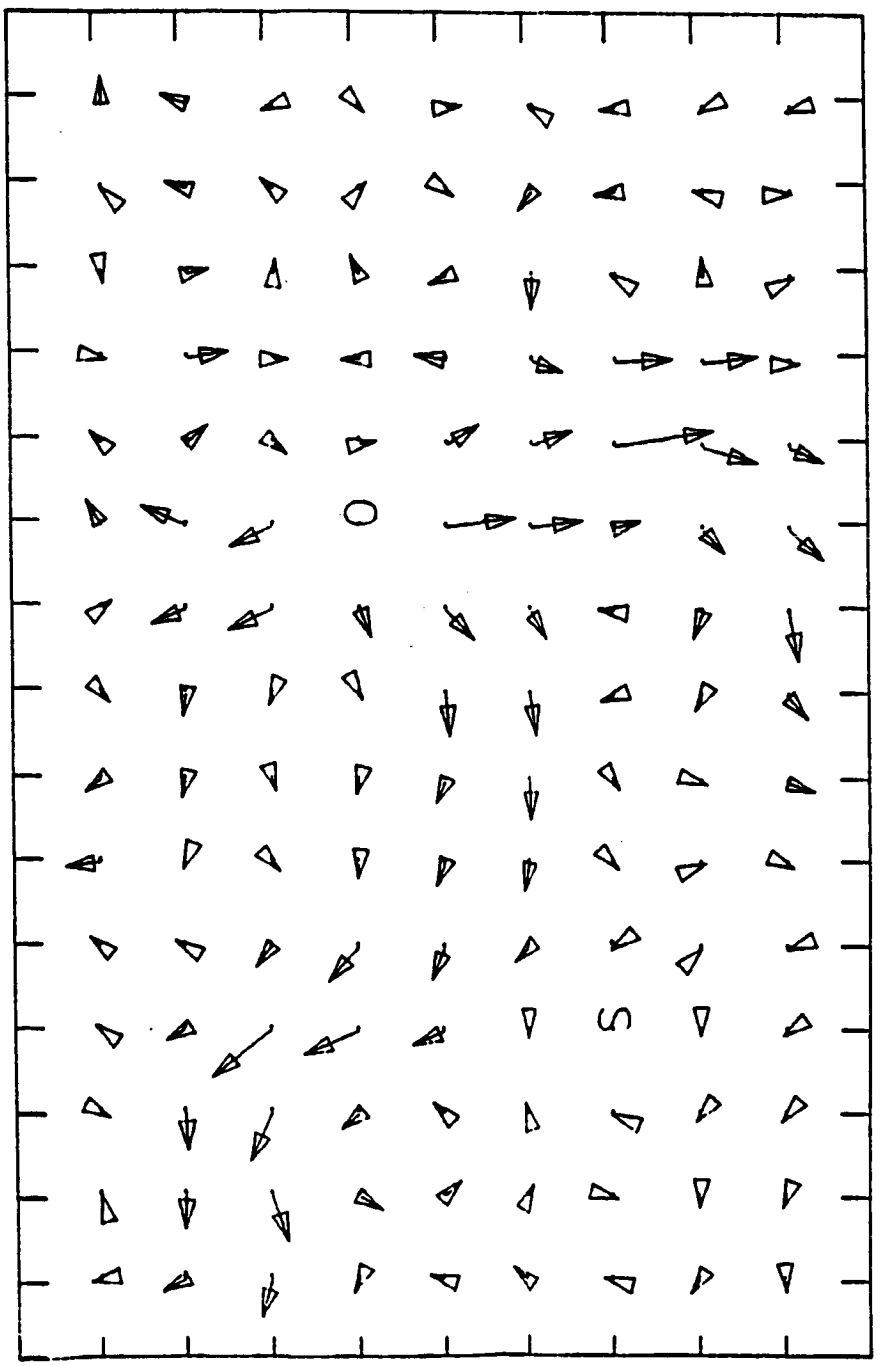

Figure 4.32 Intensity Mapping for the Plate at 250 Hz

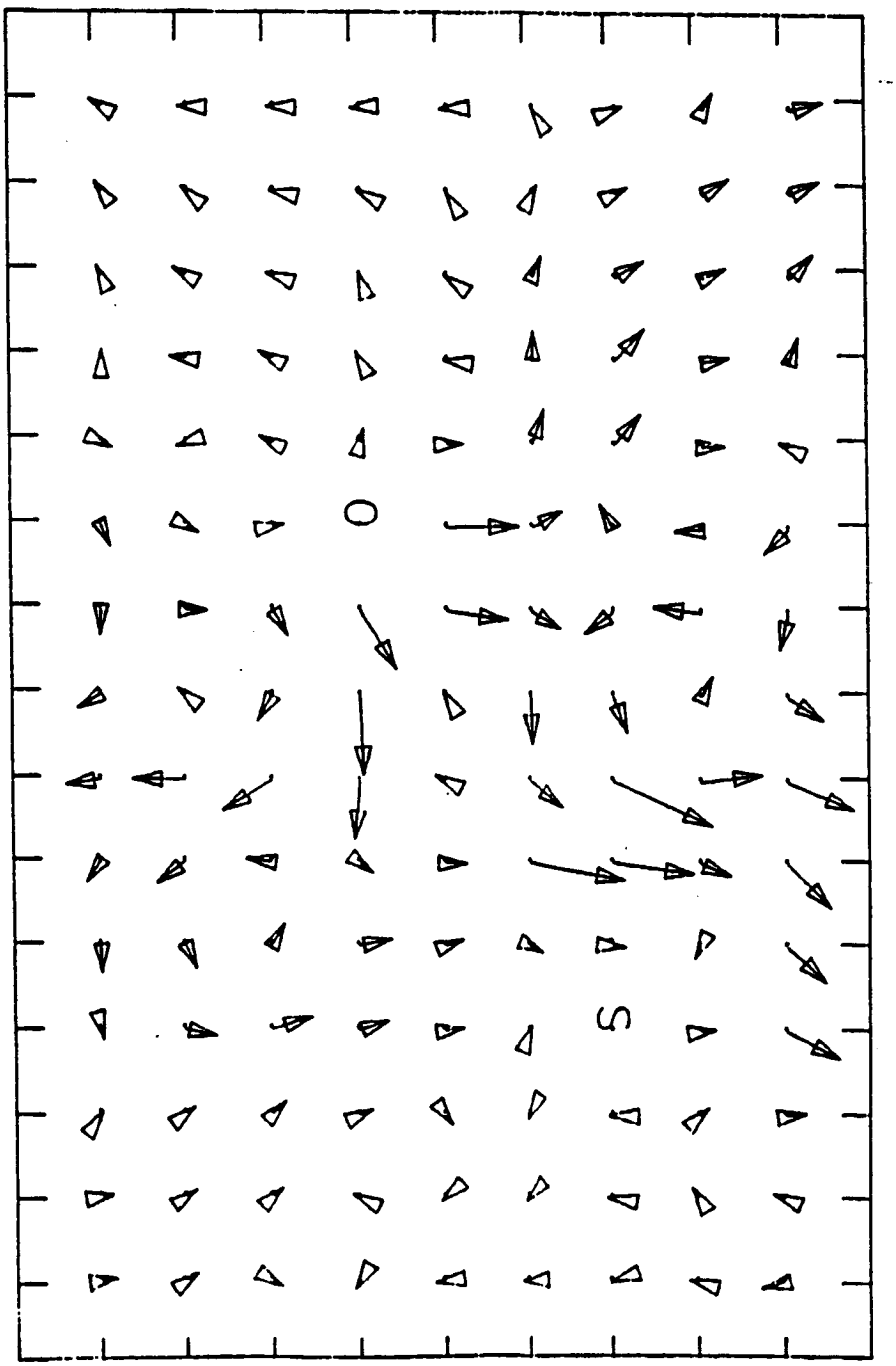

Figure 4.33 Intensity Mapping for the Plate at 275 Hz

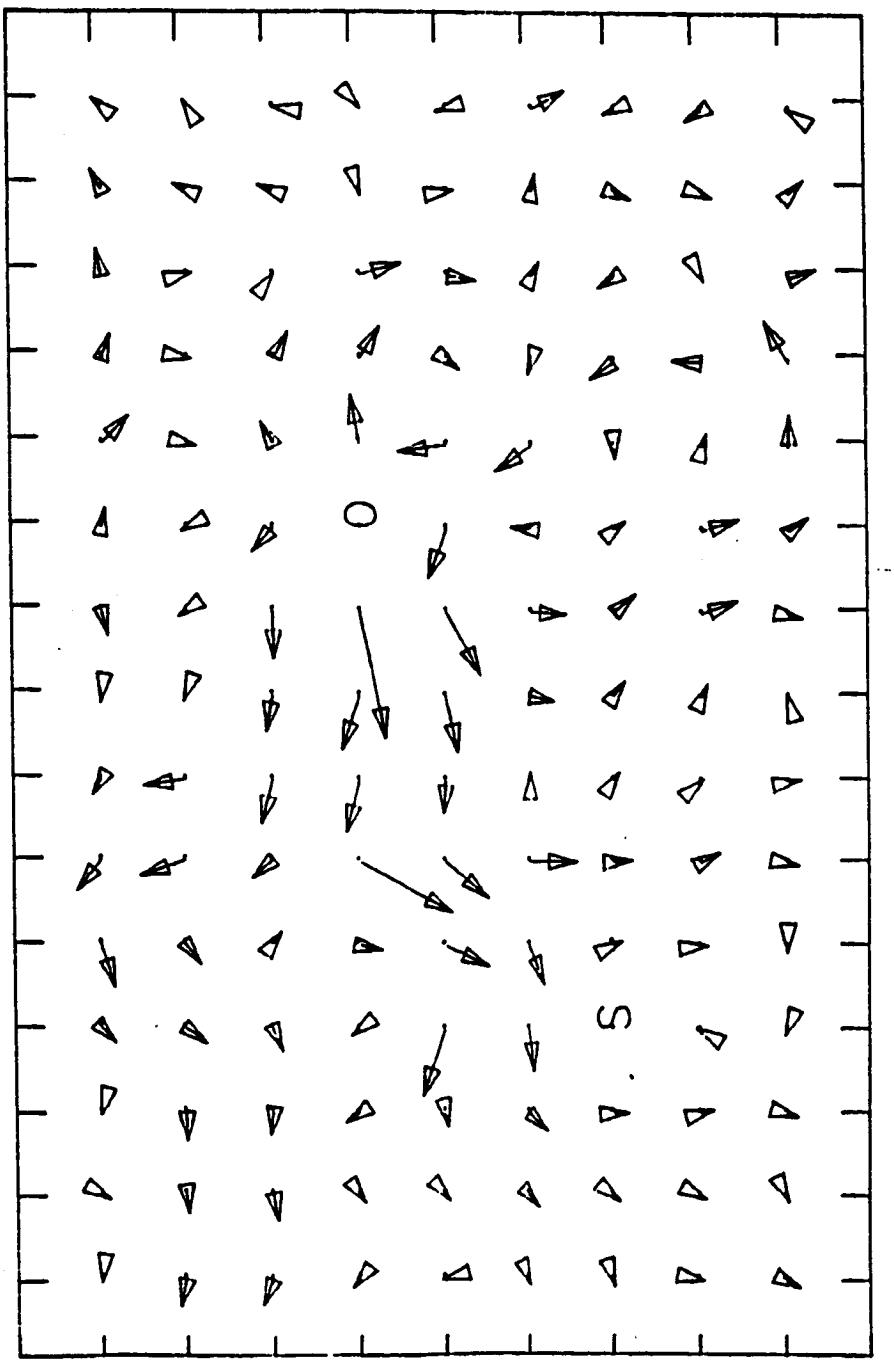

Figure 4.34 Intensity Mapping for the Plate at 300 Hz

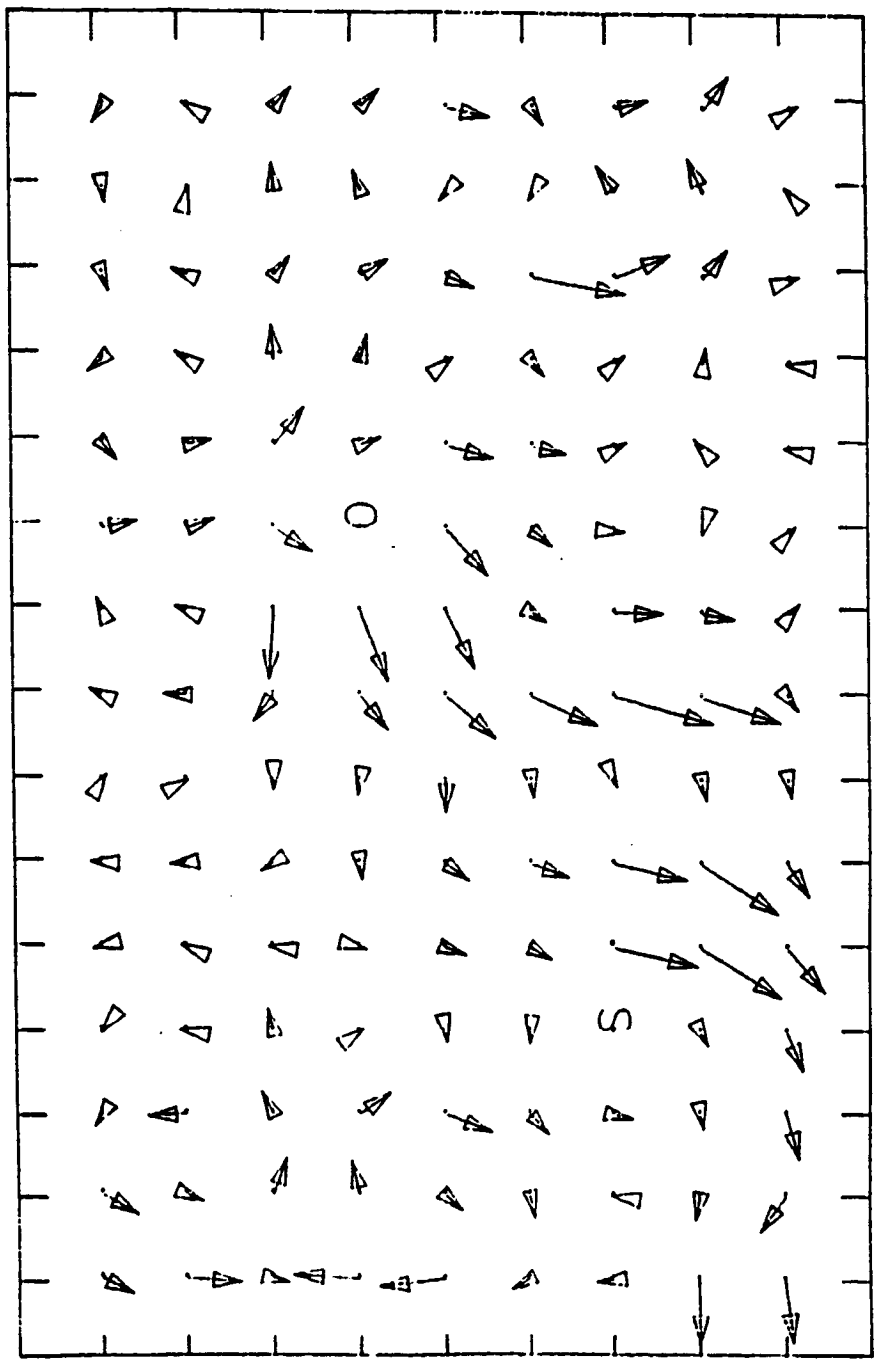

Figure 4.35 Intensity Mapping for the Plate at 325 Hz

was also probably used in its nonlinear range for motion because it was not supported in the tests and therefore the shaker flexures "bottom out" on either the shaker housing or the permanent magnet. The time dependent damping provided by the supports and passive shaker could alter the power flow over the course of an approximately 6 1/2 hour measurement period. In the grid consisting of 135 locations, some locations (for certain frequencies) are located in the near field of the source, sink, and boundary. Therefore, the vector computed at these locations and frequency would be in error. Also the influence of the probe in the vibration field was not considered, as described in section 4.8.3. From earlier investigations, it is expected that the influence of the probe could have shifted intensity vectors significantly to confuse the mappings.

The ratio of probe spacing to wavelength referred to earlier is an important consideration and is included in figure 4.16. At the frequencies where the intensity mappings are shown, the ratio is quite small, indicating that the actual phase difference to be distinguished by the probe is quite small. It may be indiscernible compared with the phase difference between accelerometers in the probe. Thus, some error due to phase mismatch is expected. The relative role played by each of the factors is difficult to determine.

While the figures given show that structural intensity measurements are useful in identifying noise sources and sinks, much could be done to extract more information from a mapping of this nature. Using a 13 accelerometer probe, one could overcome the near field error, reduce data collection time and could obtain intensity in orthogonal orientations simultaneously. Thirteen accelerometers are necessary for the finite difference approximation of a fourth-order equation (including cross terms). It would be more desirable if the two-dimensional intensity measurement could be made using a non-contacting probe.

4.8 Experimental Error Analysis

In the process of taking structural intensity measurements, certain items were found to influence the accuracy of the measurements. The structural intensity technique is very sensitive to phase mismatch between the measuring channels. Also the influence of the intensity probe on the vibrational characteristics of the structure was found to be significant.

4.8.1 Mismatch in the Equipment Channels

The channel mismatch can be a combination of two types: gain or phase. The channel gain mismatch for the transducers appeared insignificant as shown in figure 4.3.

Gain mismatch is readily overcome because the construction of the accelerometer is such that a linear range is ensured and in addition, the calibration factors are found using a single accelerometer calibrator. While the accelerometers themselves present no major problems to gain mismatch, care must be taken with the rest of the components which comprise a measurement channel. The amplifier, cables, and FFT channels can all introduce gain differences.

The phase mismatch between the channels can also result in large errors in intensity. Thompson and Tree [29] have shown that error in intensity, ε_p, due to phase differences can be written as:

$$\varepsilon_p = \frac{\sin\Delta\Phi - \sin(\Delta\Phi \pm \Delta\alpha)}{\sin\Delta\Phi} \qquad (4.6)$$

or for small angles simply as:

$$\varepsilon_p = \frac{\Delta\alpha}{\Delta\Phi} \qquad (4.7)$$

where $\Delta\Phi$ is the actual physical phase difference and $\Delta\alpha$ is the instrument phase error. While the phase difference between microphones in an acoustical intensity probe can be quite large, accelerometers are generally well phase-matched. In comparing figure 4.36, which depicts the phase of an actual structure and figure 4.3, which illustrates the phase difference between accelerometers in the intensity probe, one can see the actual phase. One run was conducted using a probe switching technique where the phase

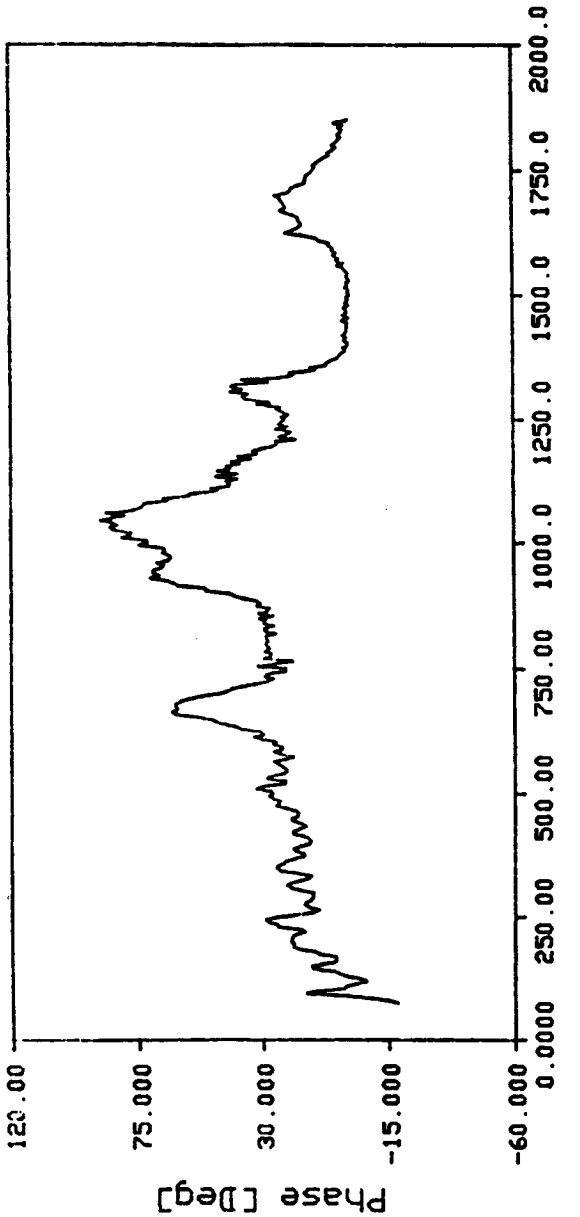

Figure 4.36 Typical Phase Difference Between Accelerometers for a Test Structure

difference is removed. This was discussed in detail in section 4.6. Apparently, despite the fact that the accelerometers appear phase matched, probe switching improved the results.

The phase mismatch between the force gauge and accelerometer used in the power calculation in section 4.5 can also be a source of error similar to the two accelerometers in the intensity probe. The phase difference was measured and found to be slight compared to the phase difference found in injected power measurements of a test structure.

4.8.2 Force Gauge and Accelerometer versus Impedance Head Measurements

Section 4.5 discusses how measurements were made using a force gauge and accelerometer. Initially the power measurement for comparison to the intensity measurement was obtained using an impedance head. However when discussing the discrepancy between the methods with the manufacturer of the impedance head, a decision was made to substitute the force gauge and accelerometer. Figure 4.37 shows the differences in results.

The particular impedance head used in this investigation seemed to be sensitive to mounting configuration. While the injected power found by the impedance head was

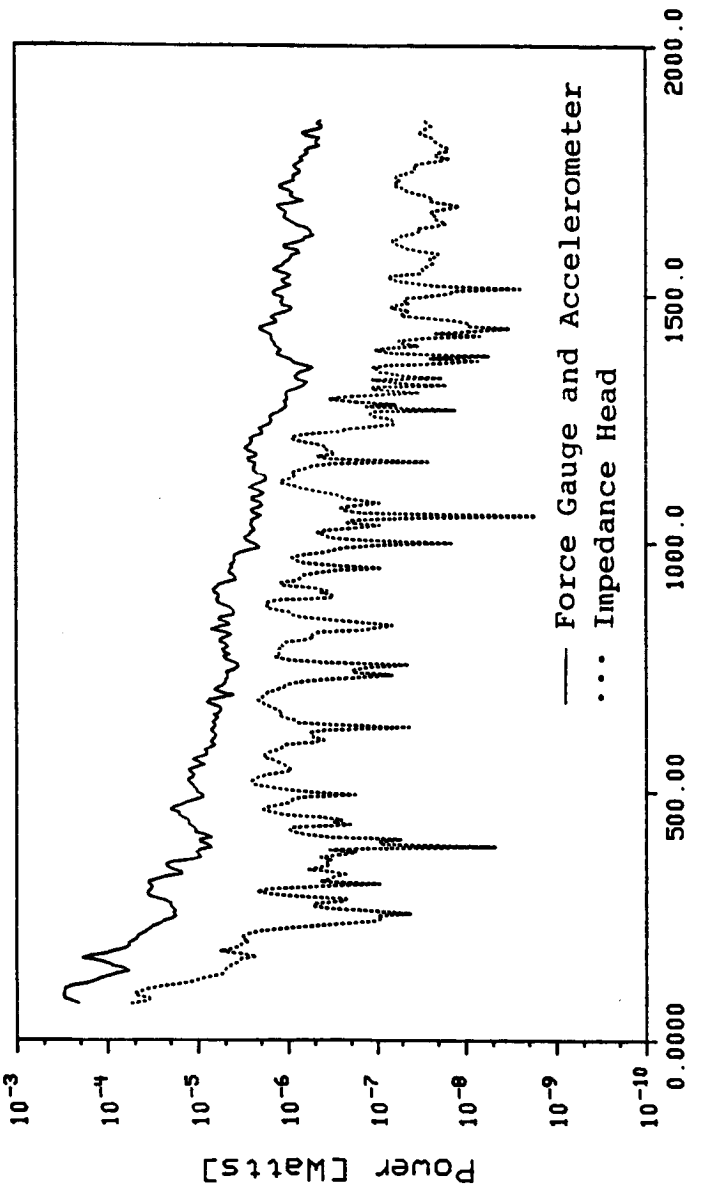

Figure 4.37 Power Measured by an Impedance Head and that Measured by a Force Gauge and Accelerometer

generally not as great, the impedance head also appeared to suffer from a resonant condition. The impedance head also exhibited resonant behavior in the frequency domain transfer function, acceleration over input force, in the excitation of what could be considered a lumped mass. The force gauge and accelerometer did not show this resonant behavior and consequently were believed to be preferable.

4.8.3 Probe Location, Mass and Rotational Inertia

With any measurement where the transducer is placed in the medium to be tested, errors result from the disturbance of the transducer. The measurement will be valid if the perturbation can be considered negligible. Quinlan [22] alluded to Beranek [1] who determined the effect of the point mass loading of a probe on the plate in the vibration field. Knowledge of the point mass loading of a transducer probe on the structure determines the nearfield effect of that transducer. For the .062" aluminum beam and plate, a 7.35 g probe will produce a 3 dB error at about 1800 Hz. For the 0.125" aluminum beam, the same error occurs at about 7500 Hz. The high frequency limit for this investigation was 1850 Hz so the error does not play a great role in the measurements. The nearfield effect of the probe (found insignificant) discussed here differs from the effect of section 3.2.2. Section 3.2.2 refers to the loading of the probe on the source.

There was, however, a very noticeable difference between the power spectrum of the injected power obtained from the accelerometer and force gauge with the probe in place and with it removed. The difference can be seen in comparing the results of figure 4.38. The beam used was .062" thick, 96" long, and 3" wide. The probe was placed at a distance of 12" from the source.

To study the effect of the probe analytically (much like section 3.5 "Sensitivity of Power Measurements to Probe Parameters"), the model of figure 3.1 was loaded with probes of different mass and rotational inertias. The actual experimental intensity probe had a mass of 7.35 g and a calculated rotational inertia of $1(10)^{-5}$ kg m^2. Figure 4.39 gives the power injected into a point-driven, point-damped aluminum beam with a rotational inertia the same as the actual probe. The mass was varied at 0, 2, 4, 7.35, 12, and 20 g. Increasing the mass of the probe tends to shift the power spectrum to the left or toward lower frequency. The shift results from the fact that for harmonic excitation, the mass is multiplied by the square of frequency in the force balance at the probe location. The effect of the term increases with increasing mass. The amplitude is affected more at higher frequency, however it may increase or decrease as shown by the seventh and eighth peaks of the spectrum. Each progressive mass increment effects the spectrum less.

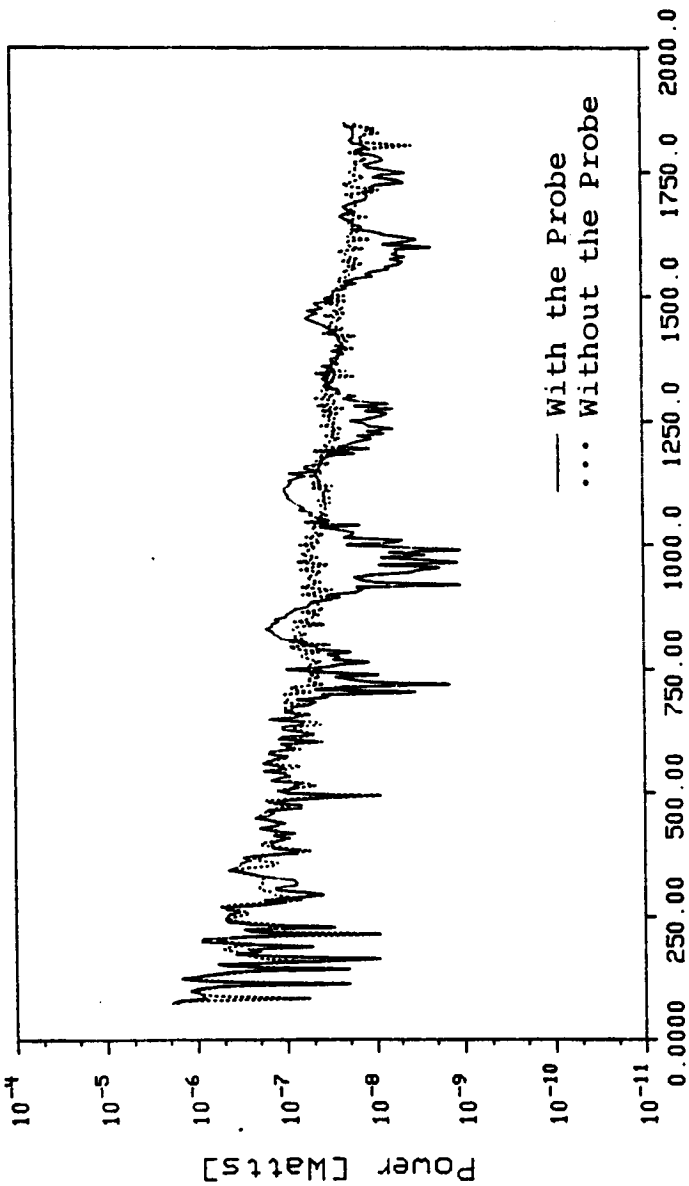

Figure 4.38 Power Injected into a Beam with the Probe in Place and Absent

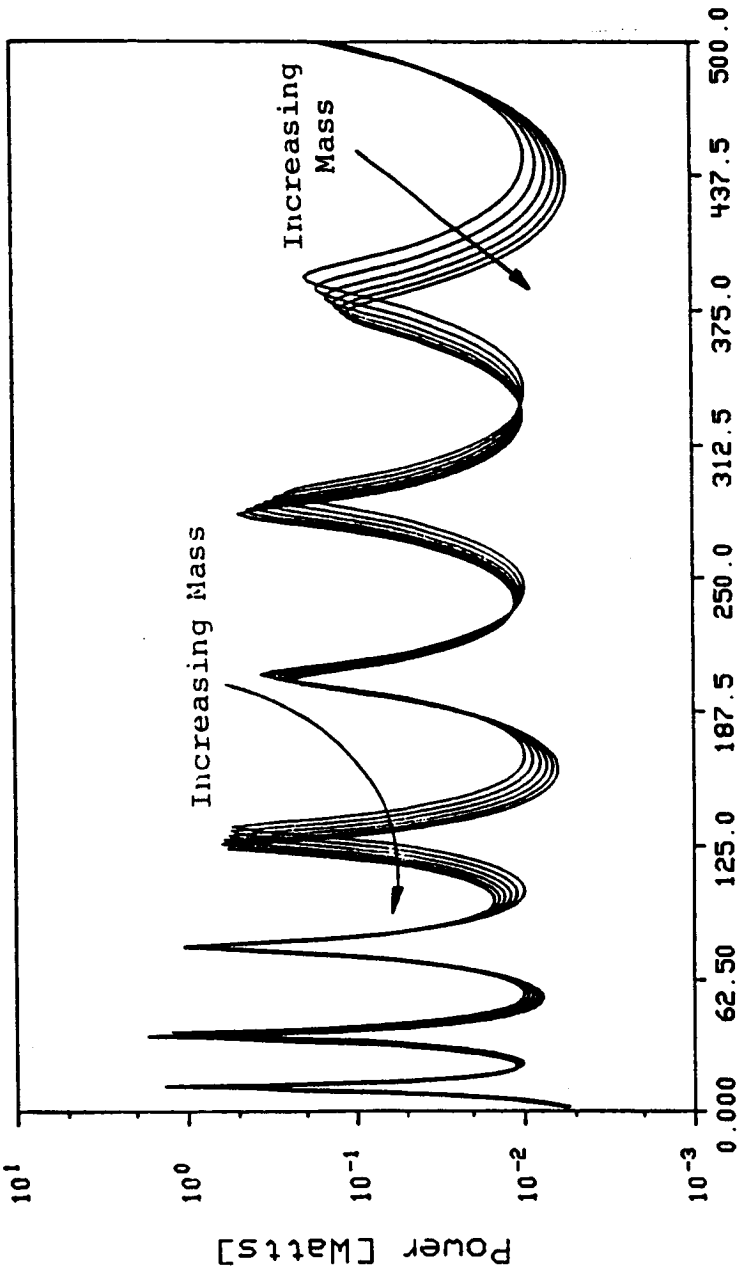

Figure 4.39 The Effect of the Mass of the Probe on Power Flow

Further, the effect of varying the rotational inertia of the probe was studied. For the beam above, with the mass of the analytical probe equal to that of the actual probe, spectra of the injected power were calculated for probe rotational inertias of 0, $1(10)^{-5}$, $4(10)^{-5}$, $8(10)^{-5}$, and $1.2(10)^{-4}$ kg m^2. The effect of rotational inertia is illustrated in figure 4.40. Again, increasing the rotational inertia had a larger effect at higher frequency. The increase seemed to remain constant as progressive increments of rotational inertia were added.

The effect of changing the location of the mass greatly changes the power injected as shown in figure 4.41. The same analytical beam was used, with mass and rotational inertia of the analytical probe equal to that of the actual probe. Due to the dispersive nature of wave propagation in the structures, any one position will be a node, antinode, and between a node and antinode for multifrequency analysis. Modes are not affected, however, if the probe location is also a nodal location.

4.8.4 Measurement in a Reactive Field

Just as in the case of acoustic intensity, the structural intensity technique is sensitive to measurement in a reactive field. Whereas a free-field (totally anechoic) is relatively easy to arrange experimentally in air-borne

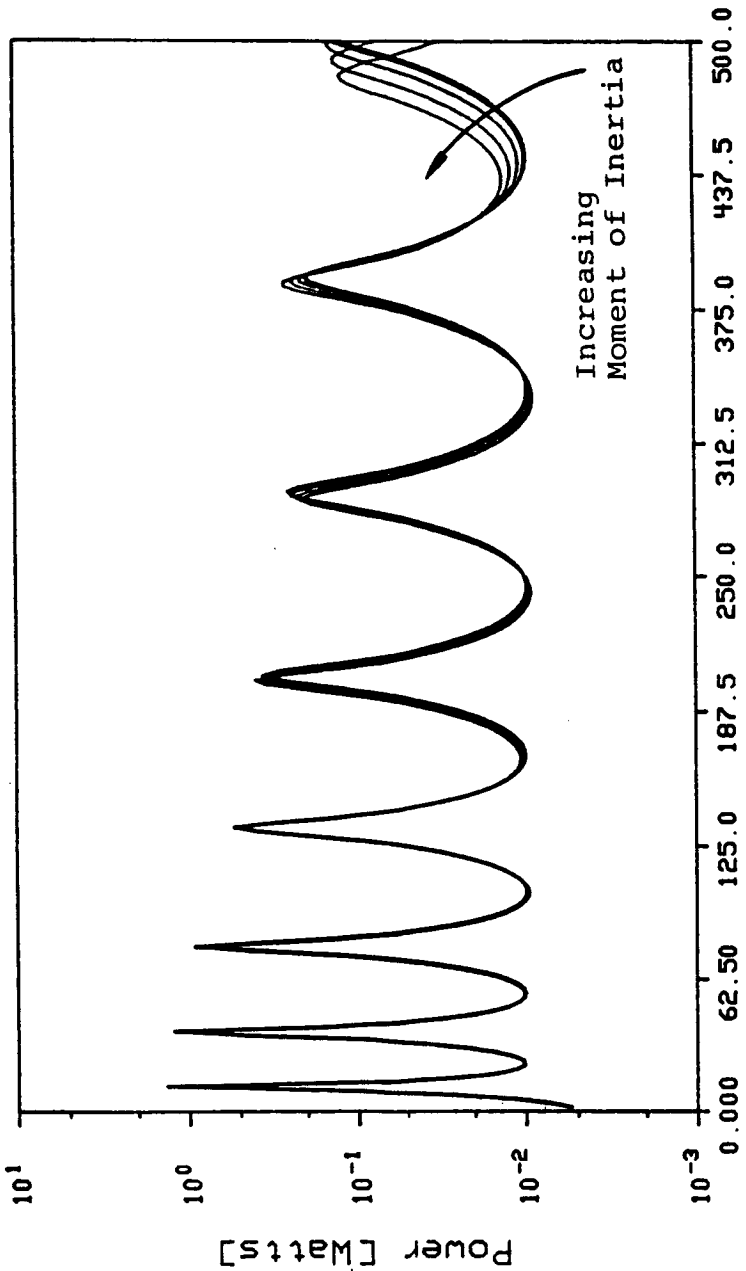

Figure 4.40 The Effect of the Rotational Inertia of the Probe on Power Flow

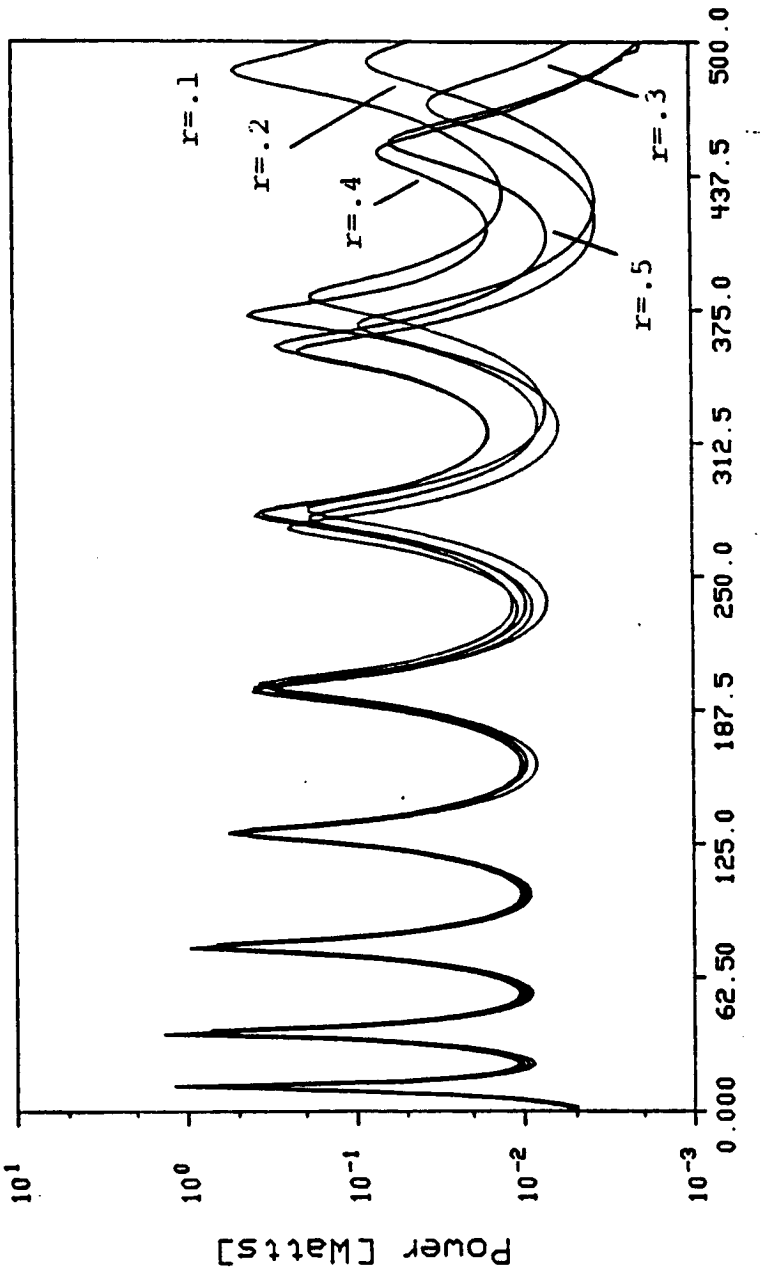

Figure 4.41 The Effect of the Location of the Probe on Power Flow

sound, it is difficult to achieve in common structures. Therefore, determining the effects of making measurements in a reactive field is essential.

Quinlan also gives an equation for the normalized bias error which is defined as the difference between the estimated value of intensity and the actual intensity divided by the actual intensity. For no gain mismatch between measurement channels and small phase errors, the equation is

$$\varepsilon_B \simeq \frac{\sin(\delta(\omega))\mathrm{Re}[S_{12}(\omega)]}{\mathrm{Im}[S_{12}(\omega)]} \qquad (4.8)$$

where $S_{12}(\omega)$ is the cross spectrum between the signals of accelerometer 1 and 2 and $\delta(\omega)$ is the actual physical phase difference in the structural intensity measurement. The reactive intensity is proportional to $\mathrm{Im}[S_{12}(\omega)]$ and the active intensity is proportional to $\mathrm{Re}[S_{12}(\omega)]$. It can clearly be seen that the bias error increases when the ratio of reactive to active intensity is increased, assuming that the phase angle is significant. However, the near field effects of fourth order behavior are also ignored and means that the probe must be positioned away from the source and boundaries.

CHAPTER 5 - CONCLUSIONS AND RECOMMENDATIONS

5.1 Conclusions

Structural intensity measurement is potentially a very powerful technique for the identification of structure-borne noise sources, sinks and paths. However, as previous investigators have pointed out, the two accelerometer implementation of structural intensity is quite limited in its application. In particular, it has been demonstrated that the method may only be used for measurement of flexural wave energy in the farfield of the plate in vibration fields where a significant part of the motion is due to active energy transport rather than standing waves. The method is also subject to high and low frequency limits due to the sensitivity of the probe and the finite difference approximation. The technique also suffers in accuracy when significant phase and gain mismatch exist between the two measurement channels.

This investigation has been concerned primarily with the applicability of the two accelerometer structural intensity implementation in thin plate structures typical

of aircraft. A previously unreported limitation of the intensity measurement is discussed in this investigation. It was discovered in measurement that the inertia of the probe significantly affects the power input to a thin plate. When the inertia of the probe is compensated for the intensity apparently is accurately measured. The accuracy of intensity measurement is verified by integrating intensity over a surface and comparing the power to measured input power. Under well controlled conditions the integrated power and input power are very well matched.

The sensitivity of the intensity measurement to probe inertia was also demonstrated theoretically using a beam solution. It was found that for a typical beam with typical probe inertias, the injected power to a beam is very sensitive to probe location and inertia. It was also shown that such sensitivity also changes with damping (i.e. the active component of energy flow).

To complement the measurement of intensity for structural modeling and for complex structures, the structural intensity calculation was formulated for the finite element. A popular finite element code, ANSYS, was used for this study. The implementation required some postprocessing. However, the finite element formulation was successfully verified for both one-dimensional and two-dimensional geometries. The method can be used to identify

power flow in built-up structures. In addition, the resulting intensity computations can be directly compared with measurements to verify models and identify system behavior.

5.2 Recommendations

Several areas were identified which require more extensive research. Experimentally it would be advantageous to be able to include the near field of discontinuities as viable regions for measurement since for built-up structures under low frequency excitation any location on the structure may be considered near field. With a technique accurate in the near field, the effect of discontinuities such as rivets, edges, bends, etc. could be identified.

In considering the effect of the probe parameters on the sound field, the advantages of implementing a non-contacting means of measuring the structural motion, such as proximeter probes, microphones, or laser velocimeters, are clear. However, it would also be advantageous to use a 4 transducer probe so that the intensity in the two orthogonal directions could be obtained simultaneously and a precise probe construction which would ensure nearly exact orthogonal measurements.

The Schroeder-phased excitation signal offered advantages over single frequency excitation since the injected

power comparisons can be made over a wide frequency range. Both the magnitude and the character or shape of the injected power can be compared with a multifrequency signal.

The finite element procedure of this report illustrates the path identification possible with the finite element method. The finite element procedure developed here should, however, be used with complete structural acoustic finite element models which include resistive components. The analytical models of damping require more development and structural intensity measurement can prove very beneficial in the development. Higher order elements with better continuity constraints are needed. ANSYS and NASTRAN are limited due to the relatively low order elements.

Lastly it is recommended, where possible, to use a force gauge and accelerometer to monitor the change in phase difference during each measurement at a new location. The monitoring indicates when the effect of the probe is significant enough to corrupt the measurement.

LIST OF REFERENCES

LIST OF REFERENCES

[1] Beranek, L.L., Noise and Vibration Control, New York, McGraw-Hill Inc., 1971, pp. 62-64.

[2] Beyer, T.B., Powell, C.A., Daniels, E.F. and Pope, L.D., "Effects of Acoustic Treatment on the Interior Noise Levels of a Twin-Engine Propeller Aircraft - Experimental Flight Results and Theoretical Predictions", AIAA Paper 84-2331, 9th Aeroacoustics Conference, Oct., 1984.

[3] DeSalvo, J.G. and Swanson, J.A., "ANSYS Engineering Analysis System User's Manual", Swanson Analysis System Inc., Houston, PA, Feb, 1982.

[4] Eversman, W., Ramakrishnan, J.V. and Koval, L.R., "A Comparison of the Structureborne And Airborne Paths for Propfan Interior Noise", AIAA Paper 86-1863, 10th Aeroacoustics Conference, July, 1986.

[5] Ewins, D.J., Modal Testing: Theory and Practice, New York, John Wiley and Sons, 1984, pp. 87-137.

[6] Flower, J.O., Knott, G.F. and Forge S.C., "Application of Schroeder-Phased Harmonic Signals to Practical Identification", Measurement and Control, Vol II, Feb., 1978, pp. 69-73.

[7] Hillarby, S.N. and Oldham, D.J., "Nearfield Directivity Measurements Using the Two Microphone Intensity Measuring Technique", Acoustic Letters, 6(3), 1982, pp. 36-39.

[8] Heckl, M., "Reduction of Structure Borne Noise", Proceedings of Inter-Noise 85, Sept, 1985, pp. 69-80.

[9] Heckl, M., Cremer, L. and Ungar, E.E., Structure-Borne Sound, New York, Springer Verlag, 1973, pp. 95-121,217-37,240-303.

[10] Holmer, C.I., "Alternative Approach to Aircraft Interior Noise Control I - Damped Trim Panels", AIAA Paper 84-2371 presented at the 9th Aeroacoustics Conference, Oct., 1984.

[11] Holmer, C.I., "Alternative Approach to Aircraft Interior Noise Control II - Self-Supporting Damped Interior Shell", AIAA Paper 84-2371 presented at the 9th Aeroacoustics Conference, Oct., 1984.

[12] Jungar, M.C. and Feit, D., Sound, Structures, and Their Interaction, Cambridge, MIT Press, 1972, pp. 11-29,133-152.

[13] Kinsler, L.E., Frey, A.R., Coppens, A.B. and Sanders, J.V., Fundamentals of Acoustics, Third Edition, New York, John Wiley and Sons, 1982, pp. 64-75,104-5.

[14] Mace, B.R., "Wave Reflection and Transmission in Beams", J. Sound and Vibration, Jan, 1984. pp. 237-246.

[15] McCallion, H., Vibration of Linear Mechanical Systems, London, Longman, 1973, pp. 97-110.

[16] McGary, M.C., "A New Measurement Method for Separating Airborne and Structureborne Noise Radiated by Aircraft Type Panels", NASA Technical Paper 2079, Jan, 1982.

[17] Metcalf, V.L. and Mayes, W.H., "Structureborne Contribution to Interior Noise of Propeller Aircraft", SAE Paper 830735, 1983.

[18] Mixson, J.S., Farassat, F. and Leatherwood, J.D., "Interior Noise Consideration for Advanced High Speed Turboprop Aircraft", AIAA Paper 82-1121 presented at the 18th Joint Propulsion Conference Paper. June, 1982.

[19] Noiseux, D.U., "Measurement of Power Flow in Uniform Beams and Plates." JASA, 47(1), Jan, 1970, pp. 238-247.

[20] Oppenheim, A.V. and Schafer, R.W., Digital Signal Processing, Englewood Cliffs, NJ, Prentice-Hall, Inc., 1975, pp. 87-114.

[21] Pavic, G., "Measurement of Structure Borne Wave Intensity, Part 1 Formulation of the Method.", Journal of Sound and Vibration, 49(2), July, 1976, pp. 221-230.

[22] Quinlan, D., "Measurement of Complex Intensity and Potential Energy Density in Thin Structures", Master's Thesis, Pennsylvania State University, May, 1985.

[23] Rasmussen, P., "Measurement of Vibration Intensity", Bruel & Kjaer Report/ Department 13 Report, 1983.

[24] Redman-White, W., "The Experimental Measurement of Flexural Wave Power Flow in Structures", Proc. of Int'l Conf. on Recent Advances in Struct. Dynamics, University of Southampton, 1983, pp. 467-474.

[25] Revell, J.D., Balena, F.J. and Prydz, R.A., "Cabin Noise Weight Penalty Requirements for a High Speed Propfan-Powered Aircraft - A Progress Report", SAE Paper 821360, 1983

[26] Schroeder M.R., "Synthesis of Low-Peak-Factor Signals and Binary Sequences with Low Autocorrelation", IEEE Transactions on Info Theory, Vol. 16, Jan, 1970, pp. 85-89.

[27] SenGupta, G., Landmann, A.E., Mera, A. and Yantis, T.F., "Prediction of Structure-Borne Noise, Based on the Finite Element Method", AIAA Paper 86-1861, 1986.

[28] Snowdon, J.C., Vibration and Shock In Mechanical Systems, New York, John Wiley and Sons, 1968, pp. 270-291.

[29] Thompson, J. and Tree, D.R., "Evaluation of the Conventional and Acoustic Intensity Methods of Noise Source Identification for Small Internal Combustion Engines", Herrick Lab Report HL 79-38, Purdue University, 1979.

[30] Timoshenko, S. and Wionowsky, S., Theory of Plates and Shells, New York, McGraw-Hill Inc., 1959, pp. 79-85.

[31] Ugural, A.C., Stresses in Plates and Shells, New York, McGraw-Hill, 1981, pp. 1-25.

[32] Unruh, J.F., "Procedure for the Evaluation of Engine Isolators for Reduced Structure Borne Noise

Transmission", AIAA Paper 81-1970 presented at the 7th Aeroacoustics Conference, Oct., 1981.

[33] Verheij, J.W. and Pavic, G., "Cross Spectral Density Methods for Measuring Structure Borne Power Flow on Beams And Pipes", J. Sound and Vibration, 70(1), 1980, pp. 133-139.

[34] Waser M.P. and Crocker M.J., "Introduction to the Two-Microphone Cross-Spectral Method of Determining Sound Intensity", Noise Control Engineering Journal, 22(3), May-June, 1984, pp. 76-85.

[35] Williams, E.G., Dardy, H.D., and Fink, R.G., "A Technique for Measurement of Structure-Borne Intensity in Plates". JASA, 78(6), Dec, 1985, pp. 2061-2068.

[36] Zienkiewicz, O.C., The Finite Element Method In Engineering Science, Second Edition, London, McGraw-Hill, 1971, pp. 103-128,171-211.

APPENDICES

Appendix A : ANSYS Results

The appendix provides three-dimensional representations of the finite element results. The first page of the appendix is devoted to the uninterpolated ANSYS results. The interpolated displacement results are shown on the next page. The third and fourth pages show the uninterpolated results for moments and shear force. The displacement is the transverse harmonic amplitude of the displacement. X and y rotation refers to $\frac{\partial u_z}{\partial x}$ and $\frac{\partial u_z}{\partial x}$ respectively. The definitions of the moments and the shear force can be found in figure 2.1.

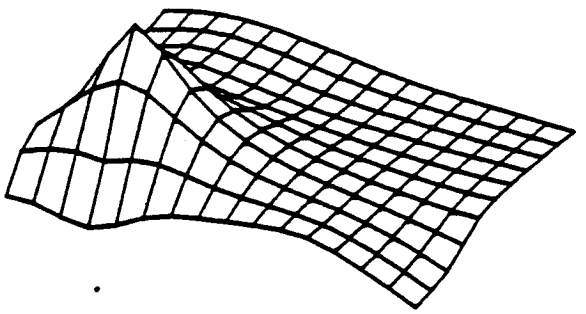

Figure A.1 Imaginary Displacement

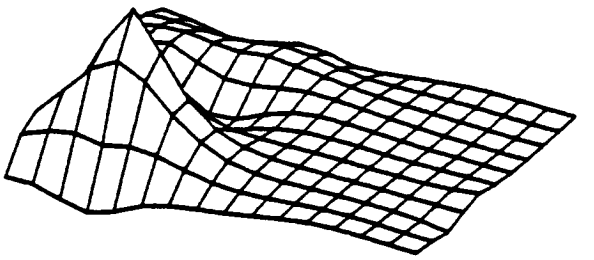

Figure A.2 Real Displacement

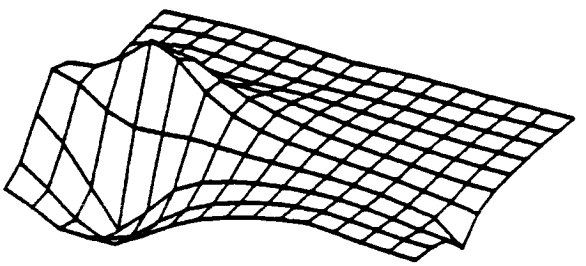

Figure A.3 Imaginary X Rotation

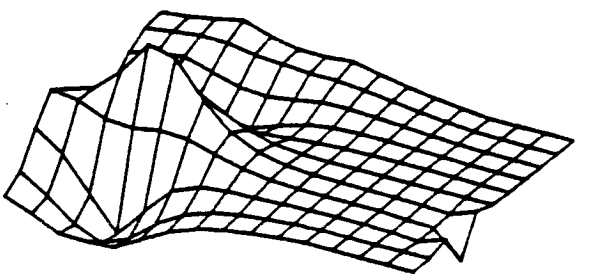

Figure A.4 Real X Rotation

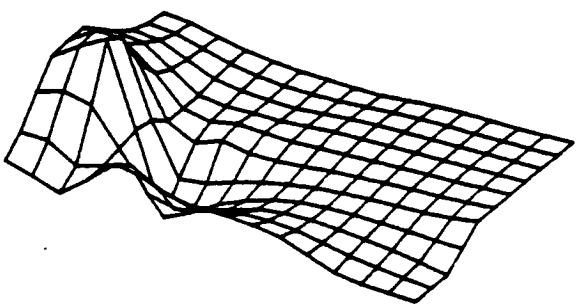

Figure A.5 Imaginary Y Rotation

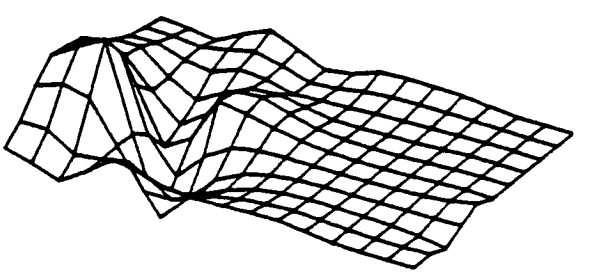

Figure A.6 Real Y Rotation

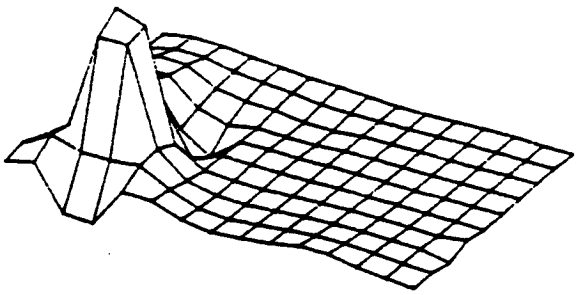

Figure A.7 Imaginary X Bending Moment

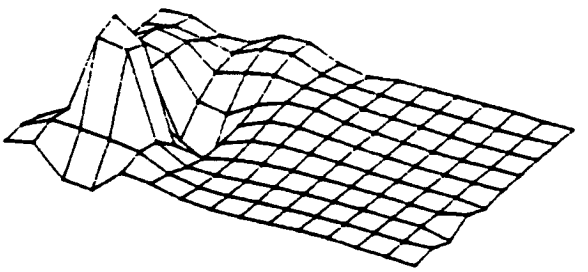

Figure A.8 Real X Bending Moment

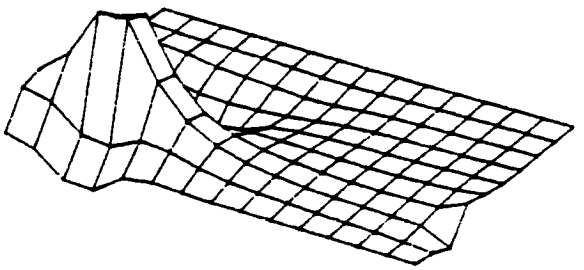

Figure A.9 Imaginary Y Bending Moment

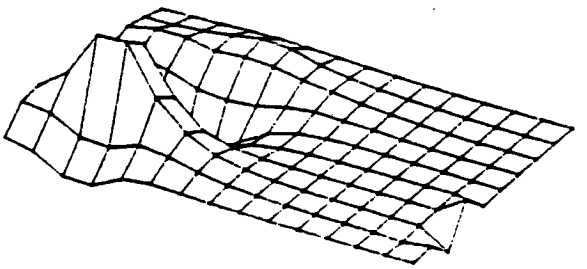

Figure A.10 Real Y Bending Moment

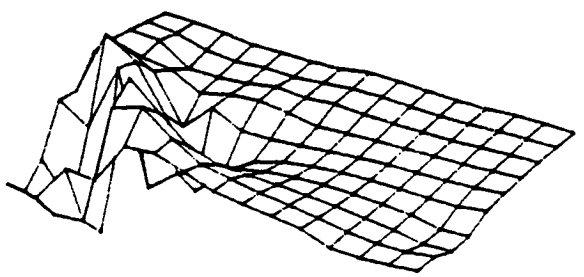

Figure A.11 Imaginary Twisting Moment

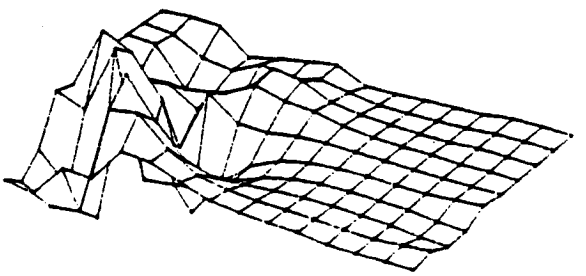

Figure A.12 Real Twisting Moment

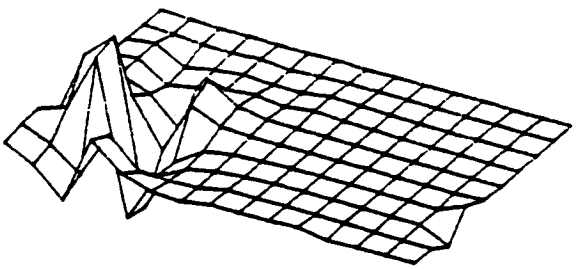

Figure A.13 Imaginary X Shear Force

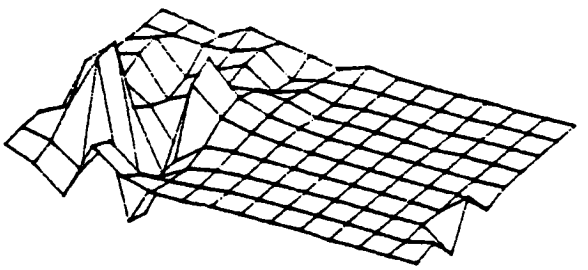

Figure A.14 Real X Shear Force

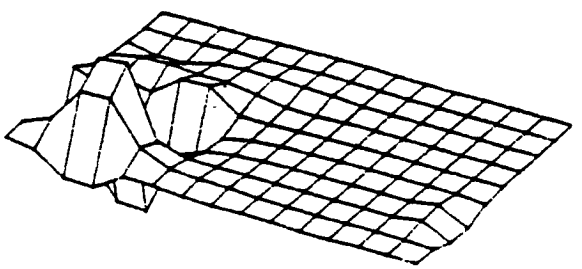

Figure A.15 Imaginary Y Shear Force

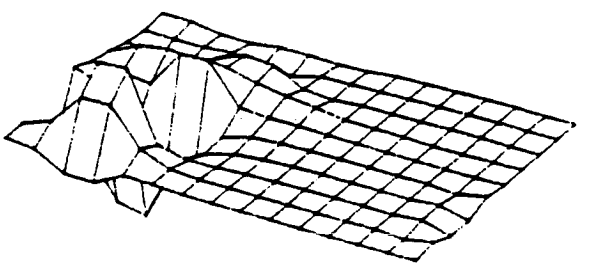

Figure A.16 Real Y Shear Force

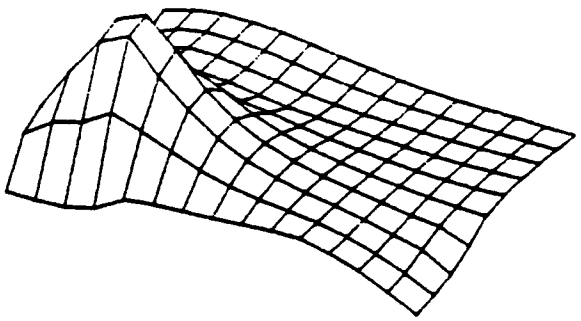

Figure A.17 Interpolated Imaginary Displacement

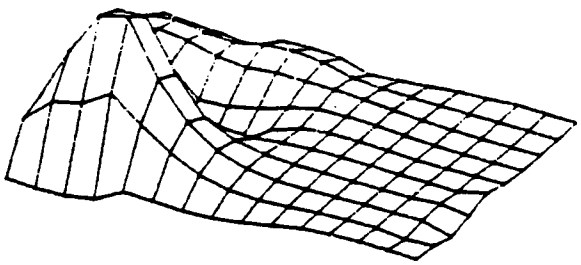

Figure A.18 Interpolated Real Displacement

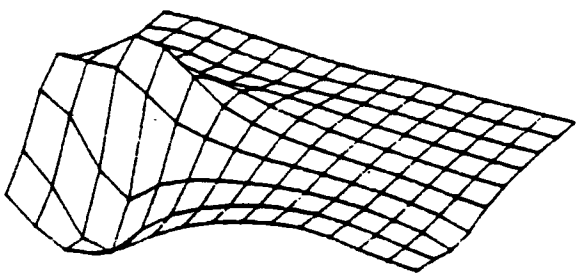

Figure A.19 Interpolated Imaginary X Rotation

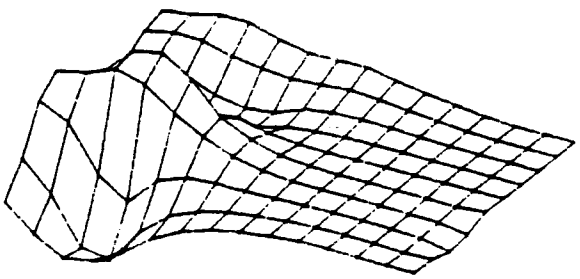

Figure A.20 Interpolated Real X Rotation

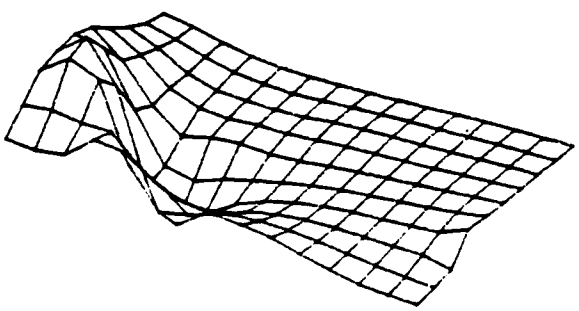

Figure A.21 Interpolated Imaginary Y Rotation

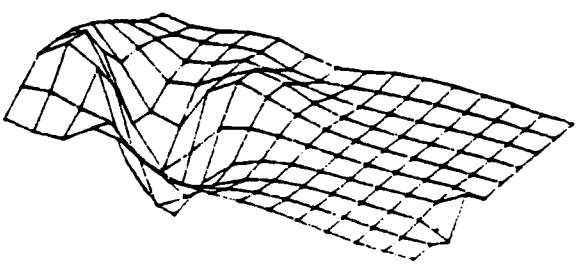

Figure A.22 Interpolated Real Y Rotation

Appendix B : Source Code of INTNS.F

This program calculates the intensity in a plate in three different manners. First, the displacement results from ANSYS are used in the transducer formulation for intensity. Secondly, the nodal displacements are interpolated to give centroidal displacements and the intensity is calculated using the moments formulation. Lastly, the intensity is determined from the interpolated displacements using the transducer formulation.

```
c  Program Intns.f reduces the output from ANSYS (real and
c  imaginary) to structural intensity.  This is done three ways:
c
c       1. The displacements (and rotations) are combined according
c          to the "two accelerometer" technique or transducer
c          formulation.
c
c       2. The moments and shear force are multiplied by
c          interpolated displacements as in the primary
c          equation from which the "two accelerometer"
c          formulation is developed.
c
c       3. The interpolated displacements are combined
c          according to the transducer formulation.
c
c  Initialize Arrays reserved for finite element results
c
c   Mxi       : array for the imaginary X bending moment
c   Myi       :                imaginary Y
c   Mxr       :                real      X
c   Myr       :                real      Y
c
c   Q*        : arrays for the real and imaginary, X and Y shear
c               forces
c
c   uz*       : arrays for the real and imaginary transverse plate
c               displacement
c
c   rot*      : arrays for the real and imaginary, X and Y plate
c               rotations.
c
c   rot*n     : arrays for the interpolated, real and imaginary,
c               X and Y plate rotations.
c
c   c         : 2 dimensional array containing the interpolation
c               coefficients
c

      real Mxi(400), Myi(400), Mxyi(400), Qxi(400), Qyi(400)
      real Mxr(400), Myr(400), Mxyr(400), Qxr(400), Qyr(400)
      real dum,six,siy,six2,siy2,ix,iy

      dimension uzi(400), rotxi(400), rotyi(400)
      dimension uzr(400), rotxr(400), rotyr(400)

      dimension uzin(400), rotxin(400), rotyin(400)
      dimension uzrn(400), rotxrn(400), rotyrn(400)

      dimension c(12,12)

c
c  The real and imaginary parts of the moments,force and motion
```

```
c  DOF's are combined in a single complex number.
c
      complex j,Mx,My,Mxy,Qx,Qy,rotx,roty,uz,rox,roy,z
      integer k,l,mm,km,mnl,ll,i,m,nnod,nelem
      character*12 rdisp,matrout,mint,idisp,dint,dint2

c
c  Set up the input and output files
c
      write(*,11)
11    format('Enter the filename of real ANSYS input')
      read(*,*) rdisp

      write(*,12)
12    format('Enter the filename of imag ANSYS input')
      read(*,*) idisp

      write(*,13)
13    format('Enter the filename for moment intensity output')
      read(*,*) mint

      write(*,14)
14    format('Enter the filename for displac intensity output')
      read(*,*) dint

      write(*,44)
44    format('Enter the filename for interpolated displacement
     &intns output')
      read(*,*) dint2

      write(*,15)
15    format('Enter the filename of Lagrange interpol. coefs')
      read(*,*) matrout

c
c  Input the Number of Elements and Nodes
c
      print*, 'Enter the no. of Nodes  in the finite element grid'
      read(*,*) nnod
      print*, 'Enter the no. of Elems. in the finite element grid'
      read(*,*) nelem

      open(1,file=rdisp)
      open(2,file=idisp)
      open(3,file=mint)
      open(4,file=matrout)
      open(30,file=dint)
      open(31,file=dint2)

      open(7,file='zr')
```

```
      open(8,file='zi')
      open(9,file='rotxr')
      open(10,file='rotxi')
      open(11,file='rotyr')
      open(12,file='rotyi')
      open(13,file='Mxr')
      open(14,file='Mxi')
      open(15,file='Myr')
      open(16,file='Myi')
      open(17,file='Mxyr')
      open(18,file='Mxyi')
      open(19,file='Qxr')
      open(20,file='Qxi')
      open(21,file='Qyr')
      open(22,file='Qyi')
      open(33,file='zrn')
      open(34,file='zin')
      open(25,file='rotxrn')
      open(26,file='rotxin')
      open(27,file='rotyrn')
      open(28,file='rotyin')

      j = cmplx(0.0,1.0)

c
c  Read in values for displacement and rotations.
c
      do 2, k=1,nnod

c
c  Data consists of node no.,x displacement(=0),y displacement(=0)
c                    z displacement,x rotation,y rotation
c                    on one line
c
       read(1,*) nod,dum,dum,uzr(k),rotxr(k),rotyr(k)
       read(2,*) nod,dum,dum,uzi(k),rotxi(k),rotyi(k)

       z   =   uzr(k) + j*uzi(k)
       roy= rotyr(k) + j*rotyi(k)
       rox= rotxr(k) + j*rotxi(k)

c
c  Calculate the intensity at each node
c
c  The displacement formulation intensity is proportional
c  to the imag part of z*conjg(rotation)
c

       ix = aimag(z*conjg(roy))
       iy = aimag(z*conjg(rox))

       write(31,*) ix,iy
```

```
      write(7,*) uzr(k)
      write(8,*) uzi(k)
      write(9,*) rotxr(k)
      write(10,*) rotxi(k)
      write(11,*) rotyr(k)
2     write(12,*) rotyi(k)

c
c  Read in values for moments and shear force.
c

      do 7, l=1,nelem

       read(2,*)  dum,dum,dum,Qxi(l),Qyi(l),Mxi(l),Myi(l),Mxyi(l)
       read(1,*)  dum,dum,dum,Qxr(l),Qyr(l),Mxr(l),Myr(l),Mxyr(l)

        write(13,*) Mxr(l)
        write(14,*) Mxi(l)
        write(15,*) Myr(l)
        write(16,*) Myi(l)
        write(17,*) Mxyr(l)
        write(18,*) Mxyi(l)
        write(19,*) Qxr(l)
        write(20,*) Qxi(l)
        write(21,*) Qyr(l)
7       write(22,*) Qyi(l)

c
c  Read in the interpolation matrix coefficients.

      do 22, k2= 1,3
22    read(4,*) (c(k2,k1), k1 = 1,12)


c  mm is the node index, incremented for each node
      mm=1

c  km is the node column index, incremented every time
c  a new nodal column in the grid is reached
      km=1

c  mnl is the nodal column size (=number of nodes on the
c   y side of the finite element rectangular mesh)
      mnl=11


      do 300, ll=1,nelem

       if(mm.eq.mnl*km) then
           mm=mm+1
           km=km+1
       endif
```

```
                print*, ' mm=',mm,mm+mn1,mm+mn1+1,mm+1

c
c  Perform the interpolation paying attention to global locations.
c
      do 301, i =1,3

      a1i = c(i,1)*uzi(mm)        + c(i,4)*uzi(mm+mn1)
     &    + c(i,7)*uzi(mm+mn1+1) + c(i,10)*uzi(mm+1)

      a1r = c(i,1)*uzr(mm)        + c(i,4)*uzr(mm+mn1)
     &    + c(i,7)*uzr(mm+mn1+1) + c(i,10)*uzr(mm+1)

      a2i = c(i,2)*rotxi(mm)        + c(i,5)*rotxi(mm+mn1)
     &     +c(i,8)*rotxi(mm+mn1+1) + c(i,11)*rotxi(mm+1)

      a2r = c(i,2)*rotxr(mm)        + c(i,5)*rotxr(mm+mn1)
     &     +c(i,8)*rotxr(mm+mn1+1) + c(i,11)*rotxr(mm+1)

      a3i = c(i,3)*rotyi(mm)        + c(i,6)*rotyi(mm+mn1)
     &     +c(i,9)*rotyi(mm+mn1+1) + c(i,12)*rotyi(mm+1)

      a3r = c(i,3)*rotyr(mm)        + c(i,6)*rotyr(mm+mn1)
     &     +c(i,9)*rotyr(mm+mn1+1) + c(i,12)*rotyr(mm+1)

      if (i.eq.1) then
       uzin(11) = a1i + a2i + a3i
       uzrn(11) = a1r + a2r + a3r
       write(34,*)uzin(11)
       write(33,*)uzrn(11)
      else
          if(i.eq.2) then
           rotxin(11) = a1i + a2i + a3i
           rotxrn(11) = a1r + a2r + a3r
           write(26,*) rotxin(11)
           write(25,*) rotxrn(11)
          else
           rotyin(11) = a1i + a2i + a3i
           rotyrn(11) = a1r + a2r + a3r
           write(28,*) rotyin(11)
           write(27,*) rotyrn(11)
          endif
       endif
 301   continue

300     mm=mm+1

c
c  Calculate structural intensity; first by initial formulation
c  and then by two accelerometer formulation.
c
```

```
      do 200, m=1,nelem

       Mx    = Mxr(m)     + j*Mxi(m)
       My    = Myr(m)     + j*Myi(m)
       Mxy   = Mxyr(m)    + j*Mxyi(m)
       Qx    = Qxr(m)     + j*Qxi(m)
       Qy    = Qyr(m)     + j*Qyi(m)
       rotx  = rotxrn(m)  + j*rotxin(m)
       roty  = rotyrn(m)  + j*rotyin(m)
       uz    = uzrn(m)    + j*uzin(m)

c
c  The interpolated moments formulation intensity
c  x and y components are calculated
c
c  The velocity is j(omega)(displac); the j changes
c  the real part to the imag part, the omega is just
c  a proportional constant - a relative magnitude
c  is necessary
c

      six=aimag(Qx*conjg(uz) + Mx*conjg(roty)
                             + Mxy*conjg(rotx))

      siy=aimag(Qy*conjg(uz) + My*conjg(rotx)
                             + Mxy*conjg(roty))

c
c  The interpolated,displacement two-accelerometer technique
c  intensity x and y components are calculated
c

       six2=  aimag(uz*conjg(roty))
       siy2=  aimag(uz*conjg(rotx))

       write(3,*) six,siy
200    write(30,*) six2,siy2


       close(1)
       close(2)
       close(3)
       close(4)
       do 19,i=7,22
19     close(i)
       close(30)
       close(33)
       close(34)

       stop
       end
```